

Spring 5-19-2018

Characterization of Ground Deformation Associated with Shallow Groundwater Processes Using Satellite Radar Interferometry

Xie Hu

Southern Methodist University, xieh@smu.edu

Follow this and additional works at: https://scholar.smu.edu/hum_sci_earthsciences_etds



Part of the [Geophysics and Seismology Commons](#), and the [Other Earth Sciences Commons](#)

Recommended Citation

Hu, Xie, "Characterization of Ground Deformation Associated with Shallow Groundwater Processes Using Satellite Radar Interferometry" (2018). *Earth Sciences Theses and Dissertations*. 4.
https://scholar.smu.edu/hum_sci_earthsciences_etds/4

This Dissertation is brought to you for free and open access by the Earth Sciences at SMU Scholar. It has been accepted for inclusion in Earth Sciences Theses and Dissertations by an authorized administrator of SMU Scholar. For more information, please visit <http://digitalrepository.smu.edu>.

CHARACTERIZATION OF GROUND DEFORMATION ASSOCIATED WITH SHALLOW
GROUNDWATER PROCESSES USING SATELLITE RADAR INTERFEROMETRY

Approved by:

Prof. Zhong Lu
Professor of Geophysics

Prof. Heather DeShon
Associate Professor of Geophysics

Dr. David George (USGS)
Research Mathematician

Prof. Robert T. Gregory
Professor of Geochemistry

Prof. Brian Stump
Professor of Seismology

CHARACTERIZATION OF GROUND DEFORMATION ASSOCIATED WITH SHALLOW
GROUNDWATER PROCESSES USING SATELLITE RADAR INTERFEROMETRY

A Dissertation Presented to the Graduate Faculty of

Dedman College

Southern Methodist University

in

Partial Fulfillment of the Requirements

for the degree of

Doctor of Philosophy

with a

Major in Geophysics

by

Xie Hu

M.A., Photogrammetry and Remote Sensing, Wuhan University, Wuhan, China

B.A., Geographic Information System, China University of Geosciences, Wuhan, China

May 19, 2018

Copyright (2018)

Xie Hu

All Rights Reserved

ACKNOWLEDGMENTS

First and foremost, I want to thank my advisor, Prof. Zhong Lu. He broadens my horizons in InSAR expertise. He has given me invaluable guidance throughout my pursuit of this PhD, encouraging me to think critically and independently. Beyond the research, he truly cares about his students' lives and treats us like family members. I am grateful beyond words for his constructive advice and most of all, encouragement, in completing this dissertation.

I would also like to thank Prof. Brian Stump, Prof. Matthew Hornbach, and Prof. Heather DeShon of SMU, for their feedback and encouragement about my research, as well as Prof. Robert Gregory for his warm support. I also appreciate the wisdom and guidance from the broader communities. In particular, I am grateful to Dr. David George, my outside committee member from USGS, for the useful discussions and comments; Dr. Thomas Pierson from USGS for his patient and scrupulous edits, as well as insightful and critical comments to my landslide manuscripts; Prof. Thomas Oommen from Michigan Technological University for his guidance in geotechnical modeling of consolidation settlement; Prof. Sylvain Barbot from Nanyang Technological University, Singapore for his guidance in analytic modeling of groundwater reservoirs; Prof. Roland Bürgmann from UC, Berkeley for his hospitality to have our family working and napping (Yusa) next to his office in August 2016, as well as his constructive comments on my research, particularly the landslide study; and Dr. Brent Delbridge from UC, Berkeley for walking me through his paper and showing me his derivation of formulas. In addition,

I thank Prof. Sigurjón Jónsson for providing me with a job as his research assistant at King Abdullah University of Science and Technology in Saudi Arabia, before I headed to the United States.

My life in the Department of Earth Science at SMU, and my five-month visit to the Earth Observatory of Singapore (EOS) at Nanyang Technological University, could not have been so enjoyable without the companionship and encouragement of my friends. In particular, I am grateful to Feifei Qu, her kind parents, and her smiley baby boy Hanghang for bringing me to their home for wonderful homemade food every week during my second pregnancy away from my family; Kevin Kwong and his lovely big family for entertaining my family in Los Angeles; SeongJu Jeong, YuRi Choi, and their cute baby girl Green, for helping me and sharing their life with me; Jin-Woo Kim for his always immediate help in work and life, even the emergency trip to the pediatrician; Yue Yin, Yanjun Hao, and their happy family for entertaining my family in Houston; and Ziling Huang for entertaining my family in Boulder and San Francisco. I also must thank Hui Wang for reminding me of our youth in high school and helping my family get used to the life in Singapore.

I would also like to thank all the staffs and friends at SMU: Stephanie Schwob, Lacey DeMara, Maria Richards, Ian Richards, Roy Beavers, and Cathy Chickering, especially for her help with the language editing of my manuscript. I also thank my colleagues and friends in our Radar Lab at SMU: Yusuf Eshqi Molan, Kimber DeGrandpre, Weiyu Zheng, Yuankun Xu, Yufen Niu, Yun Shi, Jinqi Zhao, and those I may have forgotten to include. I thank Lu Zhu for her caring and encouragement. In addition, I thank many friends at EOS for making our life in Singapore truly enjoyable. To all of you: your support in this process has been indispensable.

I thank my husband Teng for his love and support in my life, encouragement and assistance in my research.

Born on a rainy day to parents who are both working on SAR, our first baby was given the name 雨颯 (Yusa), which means standing strong in rain and wind. The second one, arriving this spring, was given the name 一舸 (Yige), which means a single boat. We hope you brothers always stand together in your life journey (风雨同舟). Thank you for being a part of my life and having me as your mom.

Finally, and most importantly, I am forever grateful to my parents and parents-in-law for traveling to the countries they are totally unfamiliar with, and for taking care of us and our babies, and to my sister for taking care of the family in China when I am not around. My academic work could not have been accomplished without their selfless support.

Hu, Xie

M.A., Wuhan University, 2013
B.A., China University of Geosciences, 2011

Characterization of Ground Deformation Associated with Shallow
Groundwater Processes Using Satellite Radar Interferometry

Advisor: Professor Zhong Lu

Doctor of Philosophy conferred May 19, 2018

Dissertation completed March 23, 2018

Shallow groundwater processes may lead to ground deformation and even geohazards. With the features of day-and-night accessibility and large-scale coverage, time-series interferometric synthetic aperture radar (InSAR) has proven a useful tool for mapping the deformation over various landscapes at cm to mm level with weekly to monthly updates. However, it has limitations such as, decorrelation, atmospheric artifacts, topographic errors, and unwrapping errors, in particular for the hilly, vegetated, and complicated deformation patterns. In this dissertation, I focus on characterizing the ground deformation over landslides, aquifer systems, and mine tailings impoundment, using the designed advanced time-series InSAR strategy, as well as the interdisciplinary knowledge of geodesy, hydrology, geophysics, and geology.

Northwestern USA has been exposed to extreme landslide hazards due to steep terrain, high precipitation, and loose root support after wildfire. I characterize the rainfall-triggered movements of Crescent Lake landslide, Washington State. The seasonal deformation at the lobe, with larger magnitudes than the downslope riverbank, suggests an amplified hydrological loading effect due to a thicker unconsolidated zone. High-temporal-resolution InSAR and GPS data reveal dynamic landslide motions. Threshold rainfall intensities and durations wet seasons have been associated with observed movement upon shearing: antecedent rainfall triggered precursory slope-normal subsidence, and the consequent increase in pore pressure at the basal surface reduces friction and

instigates downslope slip over the course of less than one month. In addition, a quasi-three-dimensional deformation field is created using multiple spaceborne InSAR observations constrained by the topographical slope, and is further used to invert for the complex geometry of landslide basal surface based on mass conservation.

Aquifer skeletons deform in response to hydraulic head changes with various time scales of delay and sensitivity. I investigate the spatio-temporal correlation among deformation, hydrological records and earthquake records over Salt Lake Valley, Utah State. A clear long-term and seasonal correlation exists between surface uplift/subsidence and groundwater recharge/discharge, allowing me to quantify hydrogeological properties. Long-term uplift reflects the net pore pressure increase associated with prolonged water recharge, probably decades ago. The distributions of previously and newly mapped faults suggest that the faults disrupt the groundwater flow and partition hydrological units.

Mine tailings gradual settle as the pore pressure dissipates and the terrain subsides, and tailings embankment failures can be extremely hazardous. I investigate the dynamics of consolidation settlement over the tailings impoundment in the vicinity of Great Salt Lake, Utah State, as well as its associated impacts to the surrounding infrastructures. Largest subsidence has been observed around the low-permeable decant pond clay at the northeast corner. The geotechnical consolidation model reveals and predicts the long-term exponentially decaying settlement process.

My studies have demonstrated that InSAR methods can advance our understanding about the potential anthropogenic impacts and natural hydrological modulations on various geodynamic settings in geodetic time scale.

TABLE OF CONTENTS

LIST OF FIGURES.....	xiv
LIST OF TABLES.....	xvii
CHAPTER 1 INTRODUCTION.....	1
1.1 InSAR methods.....	1
1.2 Chapter summaries.....	6
References.....	10
CHAPTER 2 MAPPING SLOWLY MOVING LANDSLIDES: A CASE STUDY OF THE CRESCENT LAKE LANDSLIDE, WA.....	11
2.1 Introduction.....	11
2.2 Challenges in landslide monitoring.....	13
2.2.1 Incompleteness of landslide inventory.....	13
2.2.2 Limitations of SAR measurements in landslide study.....	13
2.2.3 Complexity of landslide basal geometry.....	14
2.2.4 Complexity of rainfall triggers.....	16
2.3 Study area.....	17

2.4 Methodology.....	21
2.4.1 Time-series InSAR analysis.....	21
2.4.1.1 Coherent target (CT) selection.....	24
2.4.1.2 Topographic error (topo-error) removal.....	24
2.4.1.3 Atmospheric phase screen (APS) removal.....	28
2.4.2 Mapping slope-parallel displacement using LOS measurements.....	28
2.4.3 Mapping a quasi-3D creeping landslide using spaceborne InSAR observations...	29
2.4.4 Landslide thickness inversion.....	33
2.4.5 Analysis of landslide stability and mobility.....	35
2.5 Characterization of incipient motion of Greenleaf Basin rock avalanche.....	38
2.6 Spatio-temporal landslide motion.....	39
2.6.1 Spatial pattern of landslide motion.....	39
2.6.2 Slope-parallel movement of Cascade landslide complex.....	43
2.6.3 Seasonal deformation in response to precipitation.....	46
2.6.4 Validation of InSAR results using GPS data.....	51
2.6.5 Quasi-3D displacement fields.....	54
2.7 Active landslide thickness.....	57
2.8 Landslide stability and mobility.....	59

2.9 Discussion and conclusions.....	61
2.9.1 Biases in 3D displacements and thickness inversion.....	62
2.9.2 Plausible mechanism for precursory subsidence.....	64
Acknowledgments.....	67
References.....	68
CHAPTER 3 CHARACTERIZATION OF HYDRODYNAMICS OF SALT LAKE VALLEY, UTAH.....	74
3.1 Introduction.....	74
3.2 Study area.....	75
3.2.1 Tectonic settings.....	76
3.2.2 Hydrogeologic settings.....	77
3.3 Methodology.....	79
3.3.1 Multi-temporal InSAR analysis.....	79
3.3.2 Separation of long-term and seasonal deformation signatures.....	83
3.3.3 Estimation of aquifer properties from surface deformation and groundwater levels.....	84
3.3.3.1 Decay coefficient.....	84
3.3.3.2 Storage properties and bulk aquifer compressibility.....	85
3.4 Results.....	87
3.4.1 Spatial features of the deformation field.....	87

3.4.2 Time-series vertical deformation versus water discharge and precipitation.....	90
3.4.3 Long-term decay coefficient.....	94
3.4.4 Storage coefficient and bulk compressibility.....	97
3.4.5 Analytic modeling of the groundwater reservoir.....	101
3.5 Discussion and conclusions.....	105
3.5.1 Localized anthropogenic deformation and basin-wide hydrogeologic effects....	105
3.5.2 Long-term deformation due to a delayed response to the prolonged head changes.....	108
3.5.3 Salt Lake Valley, UT and Santa Clara Valley, CA: similarity and distinction....	111
3.5.4 Correlation among seismic hazards, seasonal deformation and hydrological process at monthly scale.....	112
Acknowledgments.....	117
References.....	119
CHAPTER 4 CONSOLIDATION SETTLEMENT OF SALE LAKE COUNTY TAILINGS IMPOUNDMENT.....	
4.1 Introduction.....	125
4.2 Study area and related hazards.....	129
4.3 Multi-temporal InSAR analysis.....	131
4.4 Data analysis and interpretation.....	135
4.4.1 Drastic settlement of the south pond.....	136

4.4.2 Stability of the embankments and surrounding area.....	142
4.5 Consolidation settlement modeling.....	145
4.6 Discussion and conclusions.....	152
Acknowledgments.....	153
References.....	154
CHAPTER 5 CONCLUDING REMARKS.....	158
5.1 Highlights.....	158
5.2 Future work.....	160

LIST OF FIGURES

Figure 1.1 Sketch of InSAR geometry.....	3
Figure 2.1 Geographic maps of the Cascade landslide complex.....	20
Figure 2.2 Image graph of interferometric pairs.....	22
Figure 2.3 Workflow of time-series InSAR processing.....	23
Figure 2.4 Sources of topographic error.....	26
Figure 2.5 Implications of radar look angles.....	29
Figure 2.6 Topography information over the area of interest	30
Figure 2.7 Primed coordinate system that fits on the slope-parallel/perpendicular plane	31
Figure 2.8 Landslide mobility index graphs for diverse landslides.....	37
Figure 2.9 Detection of the Greenleaf Basin rock avalanche.....	39
Figure 2.10 Time-series deformation along radar line-of-sight.	42
Figure 2.11 Derived slope-parallel landslide motion.....	45
Figure 2.12 Time-series InSAR-derived slope-parallel ground motion correlating with 30-day accumulated precipitation total	47
Figure 2.13 GPS-derived slope-parallel ground motion correlating with 30-day accumulated precipitation total	48
Figure 2.14 GPS displacements at the semipermanent GPS station.....	51
Figure 2.15 GPS displacements at the semipermanent GPS station, projected onto the LOS direction in comparison with the Sentinel-1A measurements	53
Figure 2.16 Line-of-sight deformation velocity	54
Figure 2.17 Quasi-3D displacement velocity maps	56

Figure 2.18 Thickness variation of the Crescent Lake landslide.....	58
Figure 2.19 Wetness analysis at Crescent Lake landslide.....	60
Figure 2.20 Biases in thickness inversion considering the uncertainty of slope and aspect angles	64
Figure 3.1 Locations and hydrogeologic architectures of Salt Lake Valley, Utah.....	78
Figure 3.2 Image graph of the interferometric pairs	79
Figure 3.3 Mean coherence map.....	81
Figure 3.4 Topographic error analysis	82
Figure 3.5 Azimuth interferometry over Sentinel-1A overlapping bursts	83
Figure 3.6 Vertical deformation and its feature of seasonality over Salt Lake Valley	89
Figure 3.7 Comparison between time-series ground deformation and water discharge monitoring gauges.....	91
Figure 3.8 Comparison between time-series ground deformation and meteorological monitoring gauges.....	92
Figure 3.9 Time-series ground deformation, water discharge, and precipitation.....	94
Figure 3.10 Exponentially decaying deformation.....	96
Figure 3.11 Comparison between time-series ground deformation and water level monitoring gauges.....	98
Figure 3.12 The derived hydrogeological properties	100
Figure 3.13 Groundwater reservoir modeling of the annual uplifting area.....	103
Figure 3.14 Quadtree representation of ENVISAT LOS deformation velocity	105
Figure 3.15 Localized subsidence in North Salt Lake and Lehi.....	107
Figure 3.16 Map of ground water level changes from 1975 to 2005 superimposed on the long-term vertical deformation velocity derived from 2004-2010 ENVISAT data.....	109
Figure 3.17 Water level of USGS gauge #404506111523301 in the ground uplifting area.....	111

Figure 3.18 Monthly binned histograms showing the number, magnitude and depth of tectonic earthquakes, non-linear deformation component of the area of interest, cumulative precipitation, and water discharge.....	115
Figure 4.1 Geographic maps of the tailings impoundment	128
Figure 4.2 Image graph of the interferometric pairs	132
Figure 4.3 CT points selection.....	134
Figure 4.4 2D annual displacement field of the south pond.....	136
Figure 4.5 Vertical deformation velocity in the south pond.....	138
Figure 4.6 DEM of the pond area	140
Figure 4.7 Quasi-linear cumulative deformation of four reclamation areas within the south pond	142
Figure 4.8 Vertical deformation velocity surrounding the tailings impoundment	143
Figure 4.9 Cumulative vertical deformation surrounding the impoundment and water level measurements.....	145
Figure 4.10 Decadal settlement modeling from 2000 to 2020	151
Figure 5.1 Preliminary results of InSAR-mapped the slowly moving landslides over the national forests in northern California.....	161

LIST OF TABLES

Table 2.1 Summary of 3D displacements, landslide thickness and volume due to the uncertainty of slope and aspect.	63
Table 2.2 Time points of the start of rainfall season and incipient landslide motion, and the cumulative precipitation in between	65
Table 3.1 Hydrogeological properties at water level gauges	101
Table 3.2 Best fit results for the analytic modeling.....	103
Table 4.1 Soil material properties of tailings structure.....	147

*Dedicated to my beloved parents and sister,
my husband Teng,
and my children Yusa and Yige.*

CHAPTER 1

INTRODUCTION

Ground deformation and its associated geohazards, taking place in various geodynamic settings, are usually in essence a process of changes in pore (fluid) pressure and effective stress beneath the land surface. How the hydrology-driven ground deformation evolves is a question of fundamental importance in understanding the occurrence of the geohazards or landform alternations, and more importantly, mitigating the potential risks to lives. In this dissertation, I focus on using interferometric synthetic aperture radar (InSAR) data to characterize the ground deformation caused by both natural and anthropogenic activities, in the geodynamic settings of slow-moving landslide terrain, urbanized aquifer systems and mine tailings impoundment, and to decipher the triggering mechanisms based on geophysical models.

1.1 InSAR methods

Monitoring the spatio-temporal behavior of Earth's surface deformation can advance our knowledge about underlying geodynamic processes. Interferometric synthetic aperture radar (InSAR) can measure centimeter to millimeter-level displacement with weekly to monthly updates. Different from optical sensors, the active SAR sensors transmit and receive electromagnetic microwaves regardless of weather conditions. SAR satellites have been one of the most well-recognized tools to routinely monitor geohazards through InSAR analysis [e.g., Lu and Dzurisin, 2014; Simons and Rosen, 2015]. SAR data, stored in the format of complex numbers, record the phase and amplitude information of backscattering and incoming radar echoes. The

phase represents the radar signal's round-trip traveling distance between the sensor and ground target, as well as the interaction of the radar signal with ground targets, modulated by 2π . Therefore, a subsequent unwrapping procedure has to be applied to retrieve the continuous phase changes. The amplitude represents the intensity of the backscattered electromagnetic energy, which is primarily determined by the surface dielectric constant, surface roughness, and surface slope. When two SAR images from the identical vantage of repeating passes are available, the interferometric phase ϕ , generated by the phase differential at each coregistered pixel, represents the difference in the round-trip traveling distance along the line-of-sight (LOS) direction during the time interval of those two acquisitions, assuming that the scattering phases remain the same (Figure 1.1).

$$\phi = -\frac{4\pi}{\lambda}(r_1 - r_2) \quad (1.1)$$

where λ is radar wavelength, and $r_1 - r_2$ is the range difference.

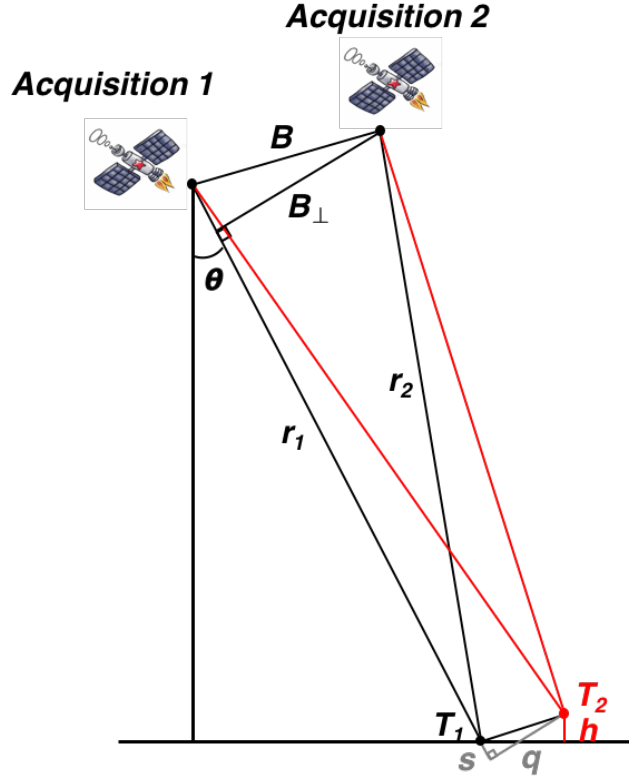


Figure 1.1 Sketch of InSAR geometry (modified from Lu and Dzurisin, 2014)

The phase difference $\Delta\phi$ between the two neighboring pixels is composed of the slant range difference s and the height difference h (Figure 1.1).

$$\Delta\phi = -\frac{4\pi}{\lambda} \frac{B_{\perp}s}{R \tan \theta} - \frac{4\pi}{\lambda} \frac{B_{\perp}h}{R \sin \theta} \quad (1.2)$$

where B_{\perp} is the perpendicular baseline between the radar sensors, R is the range distance, and θ is the look angle. The first term can be removed according to SAR system parameters, and the remaining term is the flatten interferometric phase $\Delta\phi_{flat}$. It can be used to extracted topographic elevation, assuming no surface deformation between those two acquisitions.

$$\Delta\phi_{flat} = -\frac{4\pi}{\lambda} \frac{B_{\perp}h}{R \sin \theta} \quad (1.3)$$

On the other hand, if the phase derived from topography can be subtracted from the digital elevation model (DEM), the deformation of the ground target (if exists) during the time of acquisitions can be obtained from the differential interferometric phase.

InSAR coherence is an affiliated product of interferometry, and it depicts the similarities in backscattering characteristics. The coherence map is generated by the cross-correlation of the coregistered SAR image pair in a moving window.

$$\gamma = \frac{\left| \sum C_1 C_2^* e^{-j\phi_{det}} \right|}{\sqrt{\sum |C_1|^2 \sum |C_2|^2}} \quad (1.4)$$

where C_1 and C_2 are the backscattering coefficient, the superscript * denotes the performance of the complex conjugate, j is the imaginary unit and is equivalent to $\sqrt{-1}$, ϕ_{det} is the deterministic phase due to the phase contributions by baseline, topography, atmosphere, and deformation. The loss of coherence is referred to as decorrelation.

Conventional InSAR method as described above can provide meter-level topographic elevation and centimeter-level deformation when the coherence is good. However, it is limited by decorrelation, atmospheric artifacts, topographic errors, and unwrapping errors.

Permanent scatterer InSAR (PS-InSAR) and small baseline subset (SBAS) InSAR are two representative time-series InSAR methods [Ferretti et al., 2000; Ferretti et al., 2001; Berardino et al., 2002; Hooper, 2006]. Instead of extracting information from each pixel of an interferogram, PS-InSAR and SBAS methods identify stable targets, i.e., PS points, from long time-series InSAR images. Additionally, the main concept of SBAS is the analysis of interferograms with small baselines to reduce the geometrical decorrelation and topographic error induced artifacts, for a more accurate monitoring of the temporal evolution of deformations. The solution of time-series phase values associated with the deformation for each selected PS point is given by

$$\boldsymbol{\phi}_N = (\mathbf{A}^T \mathbf{A})^{-1} \mathbf{A}^T \Delta \boldsymbol{\phi}_M \quad (1.5)$$

where $\boldsymbol{\phi}_N$ is the vector of the N unknown phase values associated with the cumulative deformation of N acquisitions in time series, $\Delta \boldsymbol{\phi}_M$ is the vector of the M known phase values from M interferograms, and \mathbf{A} is an M by N sparse matrix [Berardino et al., 2002]. The solution can be simply given by the least-squares estimation (LSE) when the unwrapped interferograms are all connected and \mathbf{A} is full rank. Otherwise, the singular value decomposition (SVD) can provide a simple solution for this inverse problem when the interferograms are not connected and \mathbf{A} is rank deficient [Berardino et al., 2002].

Time-series InSAR methods aim to separate the interferometric phase components according to their characteristics in spatial and time domains. The interferometric phase $\Delta \phi_{ifg}$ generally consists of the following components.

$$\Delta \phi_{ifg} = \Delta \phi_{def} + \Delta \phi_{topo}^\varepsilon + \Delta \phi_{atm} + \Delta \phi_{orb}^\varepsilon + \Delta \phi_{noise} \quad (1.6)$$

where

$\Delta \phi_{def}$ is the phase change due to the deformation of the ground target in LOS direction.

$\Delta \phi_{topo}^\varepsilon$ is the residual phase component due to DEM errors, and it is given by

$$\Delta \phi_{topo}^\varepsilon = -\frac{4\pi}{\lambda} \frac{B_\perp h^\varepsilon}{R \sin \theta} \quad (1.7)$$

where h^ε is DEM error. This equation states that the phase residuals due to DEM errors are proportional to the perpendicular baselines of different interferograms.

$\Delta\phi_{atm}$ is the phase component due to the difference in atmospheric delay between SAR acquisitions, and it is generally extracted by spatial-temporal filtering [Ferretti et al., 2000; Ferretti et al., 2001].

$\Delta\phi_{orb}^{\varepsilon}$ is the phase component due to orbital error, and it is characterized by low-wavelength artifacts removed by fitting deconvolving low-order polynomials.

$\Delta\phi_{noise}$ is the noise term due to thermal noise and/or coregistration errors. Normally the noise is negligible and hence disregarded.

The technical implementation of phase decomposition is discussed in more details in section 2.3.1.

1.2 Chapter summaries

Chapters 2, 3 and 4 of this work are written for peer-reviewed publication. Chapter 2 includes my research published in two journals: *Remote Sensing of Environment* [Hu et al., 2016] and *Geophysical Research Letter* [Hu et al., 2018]. Part of Chapter 3 has been written as a manuscript and accepted by *Journal of Geophysical Research: Earth Surface*. Chapter 4 has been published in *Remote Sensing of Environment* [Hu et al., 2017]. For each associated publication there are multiple authors, and the author of this dissertation is the first author and primary researcher in all cases.

Chapter 1: This chapter introduces the motivation of the dissertation research, briefly reviews the conventional InSAR method and the mainstream time-series InSAR methods, and describes the organization of the chapters.

Chapter 2: Detection of slow or limited landslide movement within broad areas of forested terrain has long been problematic, particularly for Cascade landslide complex (Washington)

located along the Columbia River Gorge. Although parts of the landslide complex have been found reactivated in recent years, the timing and magnitude of motion has not been systematically monitored or interpreted. Here I apply time-series strategies to study the spatial distribution and temporal behavior of the $\sim 4 \text{ km}^2$ reactivated translational Crescent Lake landslide movement during 2007-2011 and 2014-2016. The temporal oscillation of the seasonal motion can be correlated with precipitation, implying that seasonal movement here is very likely hydrology-driven. The seasonal motion also has a similar frequency of off-slide GPS-derived regional ground oscillations due to mass loading by stored rainfall and subsequent rebound but with much smaller magnitude, suggesting different hydrological loading effects. From the time-series SAR amplitude information on terrain upslope of the headscarp, I also re-evaluate the incipient motion related to the 2008 Greenleaf Basin rock avalanche. In addition, the combined application of on-slide GPS data with InSAR data can reveal much more about the complexity of large landslide movement. Results reveal the complex three-dimensional shape of the landslide mass, how onset of sliding relates to cumulative rainfall, how surface velocity during sliding varies with location on the topographically complex landslide surface, and how the ground surface subsides slightly in weeks prior to downslope sliding.

Chapter 3: Characterizing subsurface aquifer systems is important not only to manage their long-term viability as a stable water source, but also to protect the residences and infrastructures at the surface. In particular, understanding how aquifer skeletons deform in response to hydraulic head changes requires hydrogeological parameters such as decay coefficient, storage coefficient and bulk compressibility. Quantifying these key aquifer properties often requires the analysis of limited water gauge and drilling data. Here I investigate the spatio-temporal correlation between the vertical ground deformation derived by ENVISAT ASAR and Sentinel-1A datasets and

available hydrological records in order to improve the aquifer characterization under Salt Lake Valley, Utah. InSAR results show a clear long-term and seasonal correlation between surface uplift/subsidence and groundwater recharge/discharge, with evidence for the net uplift of 15 mm/yr for an area southwest of Salt Lake City for six years. The long-term uplift, bounded by faults and contained within the water discharge area, reflects a net increase in pore pressure associated with prolonged water recharge, probably decades ago. The distribution of both previously mapped faults and newly mapped faults within the fields of deformation and the decay coefficient suggest that the faults disrupt the groundwater flow and partition the hydrological units. I also characterize anthropogenically and hydrologically induced deformation by the features of seasonality and the deviation from the exponentially decaying model. By improving our ability to characterize aquifer structures, InSAR analysis of surface deformation in combination with traditional hydrological monitoring data presents an opportunity to recognize and mitigate potential hazards.

Chapter 4: Failures of tailings impoundment may lead to catastrophically fatal, environmental and financial consequences. Monitoring the stability of tailings facilities is therefore indispensable for sustainable mining development. Particularly, tailings experience gradual consolidation settlement as the pore pressure dissipates and the terrain subsides. However, field investigations and geotechnical analysis at tailings impoundment are limited by sparse field instrumentation due to high cost. InSAR can provide a full spatial view of settlement rate at millimeter-scale precision with bi-weekly or monthly updates. Here I integrate a large set of remotely sensed data including multi-temporal and multi-spaceborne SAR images of ENVISAT, ALOS PALSAR-1, and Sentinel-1A, and SRTM DEM and LiDAR DEM, as well as water level data, to investigate the dynamics of consolidation settlement over the tailings impoundment area in the vicinity of Great Salt Lake, Utah. Results show that the reclaimed south pond is experiencing large quasi-linear settlements

with the highest rate of 200+ mm/yr around the low-permeable decant pond clay at the northeast corner during 2004-2011, and the rate decreases to 100+ mm/yr during 2015-2016. The nearly decadal InSAR measurements can be well-explained by a geotechnical consolidation model, which matches the long-term exponentially decaying settlement and predicts the settlement process in the near future. InSAR-derived displacement maps also highlight active motions of surrounding infrastructures, such as some highway segments. There is no clear evidence that the fluctuating deformation at those locations and seasonal varied water level are correlated. The results demonstrate that high-resolution surface displacement measurements from InSAR can significantly improve our understanding of tailings settlement process and facilitate the monitoring of dams/infrastructures stability.

Chapter 5: This chapter provides a list of the highlights drawn in the studies in this dissertation, along with some future work.

REFERENCES

- Berardino, P., G. Fornaro, R. Lanari, and E. Sansosti (2002), A new algorithm for surface deformation monitoring based on small baseline differential SAR interferograms, *IEEE Transactions on Geoscience and Remote Sensing*, 40, 2375–2383.
- Ferretti, A., C. Prati, and F. Rocca (2000), Nonlinear subsidence rate estimation using permanent scatterers in differential SAR interferometry, *IEEE Transactions on Geoscience and Remote Sensing*, 38, 2202–2212.
- Ferretti, A., C. Prati, and F. Rocca (2001), Permanent scatterers in SAR interferometry, *IEEE Transactions on Geoscience and Remote Sensing*, 39, 8–20.
- Hooper A. (2006), Persistent Scatterer Radar Interferometry for Crustal Deformation Studies and Modeling of Volcanic Deformation, PhD dissertation, Stanford University.
- Hu, X., Z. Lu, T. C. Pierson, R. Kramer, and D. L. George (2018), Combining InSAR and GPS to determine transient movement and thickness of a seasonally active low-gradient translational landslide, *Geophys. Res. Lett.*, 45.
- Hu, X., T. Oommen, Z. Lu, T. Wang, and J. W. Kim (2017), Consolidation settlement of Salt Lake County tailings impoundment revealed by time-series InSAR observations from multiple radar satellites, *Remote Sens. Environ.*, 202, 199–209.
- Hu, X., T. Wang, T. C. Pierson, Z. Lu, J. W. Kim, and T. H. Cecere (2016), Detecting seasonal landslide movement within the Cascade landslide complex (Washington) using time-series SAR imagery, *Remote Sens. Environ.*, 187, 49–61.
- Lu, Z., and D. Dzurisin, (2014), *InSAR Imaging of Aleutian Volcanoes: Monitoring a Volcanic Arc from Space*, Springer Praxis Books, Geophysical Sciences, ISBN 978-3-642-00347-9, Springer, 390.
- Simons, M., and P. Rosen (2015), *A Interferometric Synthetic Aperture Radar Geodesy*, In: Gerald Schubert (editor-in-chief) *Treatise on Geophysics*, 2nd edition, Vol 3. Oxford: Elsevier, 339–385.

CHAPTER 2

MAPPING SLOWLY MOVING LANDSLIDES:

A CASE STUDY OF THE CRESCENT LAKE LANDSLIDE, WA

Hu, X., Z. Lu, T. C. Pierson, R. Kramer, and D. L. George (2018), Combining InSAR and GPS to determine transient movement and thickness of a seasonally active low-gradient translational landslide, *Geophys. Res. Lett.*, 45, 1453–1462.

Hu, X., T. Wang, T. C. Pierson, Z. Lu, J. W. Kim, and T. H. Cecere (2016), Detecting seasonal landslide movement within the Cascade landslide complex (Washington) using time-series SAR imagery, *Remote Sens. Environ.*, 187, 49–61.

2.1 Introduction

Landslides are important geomorphic processes that sculpture landscapes by transporting large volume of sediment downslope through the fluvial system. Slope failures occur in response to the increased ratio of destabilizing shear stress to resisting shear strength. They are generally recognized as the physical responses to external triggers: heavy rainfall or rapid snowmelt (increased pore-pressure) [e.g., Iverson, 2000], ground shaking (earthquakes and volcanic eruptions) [e.g., Malamud et al., 2004], ecologic events (wildfires) [e.g., Cannon et al., 2001], atmospheric tides [e.g., Schulz et al., 2009], and anthropogenic activities (overdevelopment, mining, and deforestation) [e.g., Highland and Bobrowsky, 2008]. There are two general categories of landslide processes: one is characterized by a long period of dormancy followed by abrupt mass movement along with collapse of slopes and/or a large block of slumps, often causing

causalities [e.g., Petley, 2012; Kim et al., 2015]; the other exhibits relatively slow (<4 m/yr) motions along a large (>500 m long, >5 m thick) hillslope, behaving in a plastic or viscoplastic manner [e.g., Hilley et al., 2004; Mackey and Roering, 2011; Zhao et al., 2012; Handwerger et al., 2013]. In the United States, landslides caused 25-50 causalities and over \$3.5 billion (in 2005 dollars) in damage each year with landslide sites primarily distributed in coastal and mountainous areas [Petley, 2010]. Recent extreme landslides in Oso, WA in 2014 [Iverson et al., 2015; Kim et al., 2015] and following the 2015 Gorkha earthquake in Nepal [Kargel et al., 2016] and 2016 Kumamoto earthquake in Japan [Petley, 2016], have escalated the need to identify potential catastrophic sliding hazards in mountainous regions in order to further assess the associated risks.

Detection of slow or limited landslide movement within broad areas of forested terrain has long been problematic, because slide motion may not disturb the forest enough to make the slides easily visible. Classic methods of landslide monitoring include both ground-based motion- and distance-detection sensors and the analysis of remote sensing imagery [Gili et al., 2000]. In-situ landslide monitoring subject to ground-based sensors, e.g., global positioning system (GPS), borehole inclinometers, strain gauges, and rock noise instruments, are spatially limited, logistically expensive and technically challenging. Aerial remote sensed images are also useful for landslide monitoring, but pre- or post-slide images are not always practically available on a large scale, and the image quality is heavily dependent on the condition of atmospheric water vapor, the extent of vegetative coverage, and the existence of identifiable features.

Under inclement weather conditions, synthetic aperture radar (SAR) imagery may be the only effective method for detecting unmapped landslides and monitoring active sliding motion in rural regions. Since the early 1990s, Interferometric SAR (InSAR) techniques have measured cm- to mm-level deformation in various geodynamic settings [e.g., Simons and Rosen, 2015]. With the

capability of surveying large areas, during both day and night, SAR data have proven very useful for detecting and mapping large landslides in the northwestern USA [Zhao et al., 2012]. InSAR methods can provide critical information on landslide location, boundaries, and movement [e.g., Hilley et al., 2004; Calabro et al., 2010; Zhao et al., 2012; Kim et al., 2015].

2.2 Challenges in landslide monitoring

2.2.1 Incompleteness of landslide inventory

Landslide hazards can trigger downstream flooding and reactivate faults to further threaten human lives and properties. Particularly, the northwestern USA has been exposed to extreme landslide events due to natural and anthropogenic triggering mechanisms such as high precipitation during winter as well as deforestation. Although there exist some maps for historically active landslides in the northwestern USA, not all slides have been completely mapped due to either the lack of geological evidence or cartographic limitations (e.g., <http://www.oregongeology.org/sub/slido/>). In addition, it is unknown which landslides are actively deforming and the spatial extent of active landslides. Furthermore, due to the complicated triggering factors and the lack of pre-, co-, and post-slide observations, the mechanisms of landslides are still poorly understood.

2.2.2 Limitations of SAR measurements in landslide study

Previous InSAR studies have attempted to identify active landslides over the northwestern USA [Zhao et al., 2012]. However, the interpretation was based on a couple of interferogram(s) using ALOS-1 PALSAR-1 data expressed with localized fringes over the mountainous areas, and only large slides covering larger than 0.2 km² were detected [Zhao et al., 2012]. The temporal behavior and the deformation velocity of the detected landslide has not been investigated, excepted for one site of the Boulder Creek landslide. Monitoring landslide-induced deformation using

InSAR has been limited by the following conditions. First, InSAR-based monitoring typically involves the inconsistency of scattering centers -- the three-dimensional (3D) position of the dominant scatterer that occupies the strongest electromagnetic echo within the pixel -- between radar echoes and various DEM data sources, such as Shuttle Radar Topography Mission (SRTM) and Light Detection And Ranging (LiDAR), as a result of different wavelengths of the electromagnetic waves. Second, InSAR measurements can be contaminated by atmospheric artifacts. And third, landslide movement may be non-linear in time. To overcome these limitations, specific strategies for time-series InSAR analysis need to be designed and implemented.

2.2.3 Complexity of landslide basal geometry

The 3D geometry and movement of landslides, particularly large landslides, can be complex and difficult to characterize. Conventional stability analyses [e.g., Rogers and Chung, 2016] require estimates of depth to the basal slip surface and material properties, which are usually obtained from field investigations at a few specific locations. Acquisition of such data typically involves expensive drilling or excavation at a limited number of locations, and properties between holes can only be interpolated. Furthermore, some landslide sites may be hazardous to work on and/or inaccessible.

Existing non-contact methods for determining failure surface geometry and landslide volume, such as the balanced cross-section method [e.g., Bishop, 1999; Aryal et al., 2015], the dislocation model [e.g., Nikolaeva et al., 2014; Aryal et al., 2015], and the mass conservation approach [Booth et al., 2013; Delbridge et al., 2016; Huang et al., 2017], require only an analysis of 3D displacement maps. However, these methods vary in their accuracy based on the underlying model assumptions: the balanced cross-section method considers multiple cross sections independently without taking adjacent bodies into account, and the dislocation model largely simplifies the landslide

geometrically and physically, employing a linear elastic model and a single rectangle planar basal surface [Nikolaeva et al., 2014]. Alternatively, the mass conservation approach used to map glacier ice thickness [Farinotti et al., 2009; Morlighem et al., 2011] has been extended to landslide thickness inversions [Booth et al., 2013; Delbridge et al., 2016; Huang et al., 2017]. The accuracy of these non-contact methods is limited to the accuracy of the utilized 3D displacement fields.

Spatially continuous 3D displacement fields can be constructed by geodetic methods such as differential digital elevation models (DEMs), pixel offset tracking using optical or SAR images and InSAR when three or more measurements of independent imaging geometries are available. Application of these methods still presents challenges.

The differential DEM method requires repeat high resolution DEMs, such as bare-earth LiDAR DEMs, which are not commonly available for landslide areas. In addition, most long-active landslide areas move slowly at rates of millimeters to meters per year, but the precision of DEMs is usually at the level of several to tens of meters. Therefore, high-resolution DEM difference maps must span long time intervals in order to enhance the signal-to-noise ratio.

The pixel offset tracking methods estimate deformation using pixel shifts, detected by searching for the cross-correlation peak between the matching patches of two images, one acquired before and the other after the occurrence of deformation [e.g., Scambos et al., 1992; Michel et al., 1999]. The precision of pixel offset tracking is up to 1/20 of one single-look pixel when cross correlation is high [e.g., Hu et al., 2014; Wang and Jónsson, 2015]. Optical images can be used for pixel offset tracking, but landslides are generally located in vegetated hilly terrain, so that ground features are more difficult to distinguish with optical methods than with SAR. SAR electromagnetic waves can penetrate vegetation to a certain degree (depending on the wavelength and characteristics of canopies such as thickness and moisture), making SAR data better for pixel

tracking than optical data. However, spaceborne SAR data have large pixel spacings (several to dozens of meters). Pixel offset tracking is only applicable when the displacement exceeds $\sim 1/10$ of the pixel spacing between two temporal acquisitions [Hu et al., 2014], such as for the Slumgullion landslide in Colorado, where movement is as high as ~ 2 cm/day [Delbridge et al., 2016]. Thus, the deformation magnitude of slow-moving landslides, mostly less than tens of centimeters per year [e.g., Mackey and Roering, 2011], is generally too small for detection by pixel tracking and not appropriate for this study.

InSAR methods determine deformation from the differential phase shift of reflected radar waves returning to the sensor in temporally spaced data acquisitions. But general limitations of the methods include the geometric distortion due to topographic relief and poor coherence due to vegetation [e.g., Hu et al., 2016]. Spaceborne InSAR is additionally limited by significant insensitivity to north-south motion due to LOS slant looking geometries of near-polar orbiting SAR satellites. Airborne InSAR methods (such as radar sensors mounted in unmanned aerial vehicles—UAVSAR systems) have the advantages of high-resolution detection (sub-meter to meter level) and they are not restricted to the fixed looking geometries (allowing the detection of north-south motion) [Delbridge et al., 2016]. However, airborne SAR data seldom cover large areas, and data availability is generally restricted due to agreements between service providers and clients.

2.2.4 Complexity of rainfall triggers

A decrease in effective shear strength along basal shear surfaces due to increased pore pressure from infiltrated rainwater (or snowmelt) is a major trigger of landslides [Iverson et al., 1997; Iverson et al., 2000]. The correlation of landslide movement with seasonal rainfall in the study area of the Crescent Lake landslide [Hu et al., 2016; Tong and Schmidt, 2016] indicates that it is

the operative trigger mechanism. But rainfall-triggered landslide movement, particularly the time of failure and extent of displacement and runout, is typically difficult to predict, because (a) the fluid pressure evolution is complex, owing to the combined effect of groundwater inflow and infiltration and to variations in subsurface flow paths due to the heterogeneous soil matrix at and above the basal slip surface [Iverson et al., 1997; Iverson, 2000]; (b) landslide movement is highly sensitive to the initial soil porosity and can result in contrasting dynamics upon shearing [Iverson et al., 1997; Iverson et al., 2000]; and (c) the time required for infiltration and pressure transmission to elevate the pressure head at the basal shear zone is uncertain [Iverson, 2000; Priest et al., 2011].

2.3 Study area

The Washington side of the Columbia River Gorge is especially prone to landslides due to weak underlying volcanoclastic sedimentary units that dip toward the river at 2° – 10° , a wet winter climate, and steep unbuttressed slopes [Palmer, 1977; Pierson et al., 2016]. Approximately two thirds of this terrain in the western Columbia Gorge comprises old or currently active, mostly translational landslides [Pierson et al., 2016]. The infiltration of winter rainfall and snowmelt elevates pore-water pressure and reduces frictional strength at a number of potential failure surfaces at different levels within the volcanoclastic units, resulting in landslide reactivation [Mackey and Roering, 2011; Handwerger et al., 2015].

The $\sim 36\text{-km}^2$ Cascade landslide complex (Figure 2.1), a translational landslide complex in Skamania County, Washington [Pierson et al., 2016], was originally mapped as four landslides: Carpenters landslide, Bonneville landslide, Red Bluffs landslide, and Mosley Lakes landslide [Wise, 1961]. More recent mapping [Randall, 2012] has shown that what was thought to be the Mosley Lakes landslide was a part of the Red Bluffs landslide. However, another part of the Red Bluffs landslide has reactivated within the last few decades, and is now mapped as the Crescent

Lake landslide [Pierson and Lu, 2009; Pierson et al., 2016]. Immediately east of the Cascade landslide complex is the newly recognized Stevenson landslide [Randall, 2012; Pierson et al., 2016], which is in the City of Stevenson (population ~1,500).

Landslides in the western Columbia River Gorge have occurred for at least tens to hundreds of thousands of years, but the landslides in the Cascade landslide complex are all less than 600 years old [Pierson et al., 2016]. The Bonneville landslide broke off from terrain near Table Mountain in the early 15th century and filled the Columbia Gorge with about 1 km³ of debris, dammed the river for a period of at least months, and formed a natural “bridge” across the Gorge that gave birth to the Native American legend of the Bridge of the Gods [Lawrence and Lawrence, 1958; Palmer, 1977; O’Connor, 2004 and 2009; Pierson et al., 2016] (Figure 2.1b). After the natural dam was breached, the river channel was displaced about 1 km to the south. Morphologic features of the Carpenters Lake and Red Bluffs landslides suggest that they are both younger than the Bonneville landslide, and a radiocarbon date from the toe of the Red Bluffs landslide suggests that it could be as much as 200 to 300 years younger than the Bonneville landslide [Pierson et al., 2016]. Furthermore, reactivated parts of the Carpenters Lake and Red Bluffs landslides have been active within the last 20 years—the Hot Springs and Crescent Lake landslides, and at least the latter is currently active [Pierson and Lu, 2009]. In addition, the Greenleaf Basin rock avalanche (about 375,000 m³—small in comparison to the other landslides making up the Cascade landslide complex) broke off from the western side of the headscarp of the Red Bluffs landslide on January 3, 2008 [Randall, 2012].

All of the Cascade complex slides are composed of poorly sorted coarse landslide debris (blocks up to at least many tens of meters in diameter), derived from Quaternary lavas of andesite and basaltic andesite composition, thick lavas of the middle Miocene Columbia River Basalt

group, and lahar and coarse fluvial deposits (andesite and dacite particles) of the lower Miocene Eagle Creek Formation and the upper Oligocene Weigle Formation (informal name) [Wise, 1961; Palmer, 1977; Randall, 2012; Pierson et al., 2016]. The failure planes of these dominantly translational landslides occur in bedding-parallel, clay-rich weathering horizons developed throughout the lower parts of Eagle Creek Formation and the upper parts of Weigle Formation that dip from 2° to 10° southward toward the river [Waters, 1973; Palmer, 1977; Korosec, 1987; Randall, 2012; Pierson et al., 2016].

The focus of the study is the ~4-km² Crescent Lake landslide, with an average surface slope of 10–11 percent (6°) facing southeast, a reactivated portion of the Red Bluffs landslide within the ~36-km² Cascade landslide complex. This landslide moves mainly during the winter, much of it at an average rate of 15–20 cm/yr [Hu et al., 2016; Tong and Schmidt, 2016], and it has been active for at least several decades [Braun et al., 1998]. The Crescent Lake landslide has not been drilled to determine thickness, but the adjacent Bonneville landslide (Figure 2.1) has a maximum thickness of about 150 m and an average thickness of about 76 m [Pierson et al., 2016], based on a cross section determined by drilling [Palmer, 1977].

Monitoring the movement of the landslides in this area is important due to their potential threats to the residents, roads, and infrastructure, which includes a natural gas pipeline, high-voltage electric transmission lines, a major rail line, a commercial navigation channel in the river, two large tourist facilities, and Bonneville Dam.

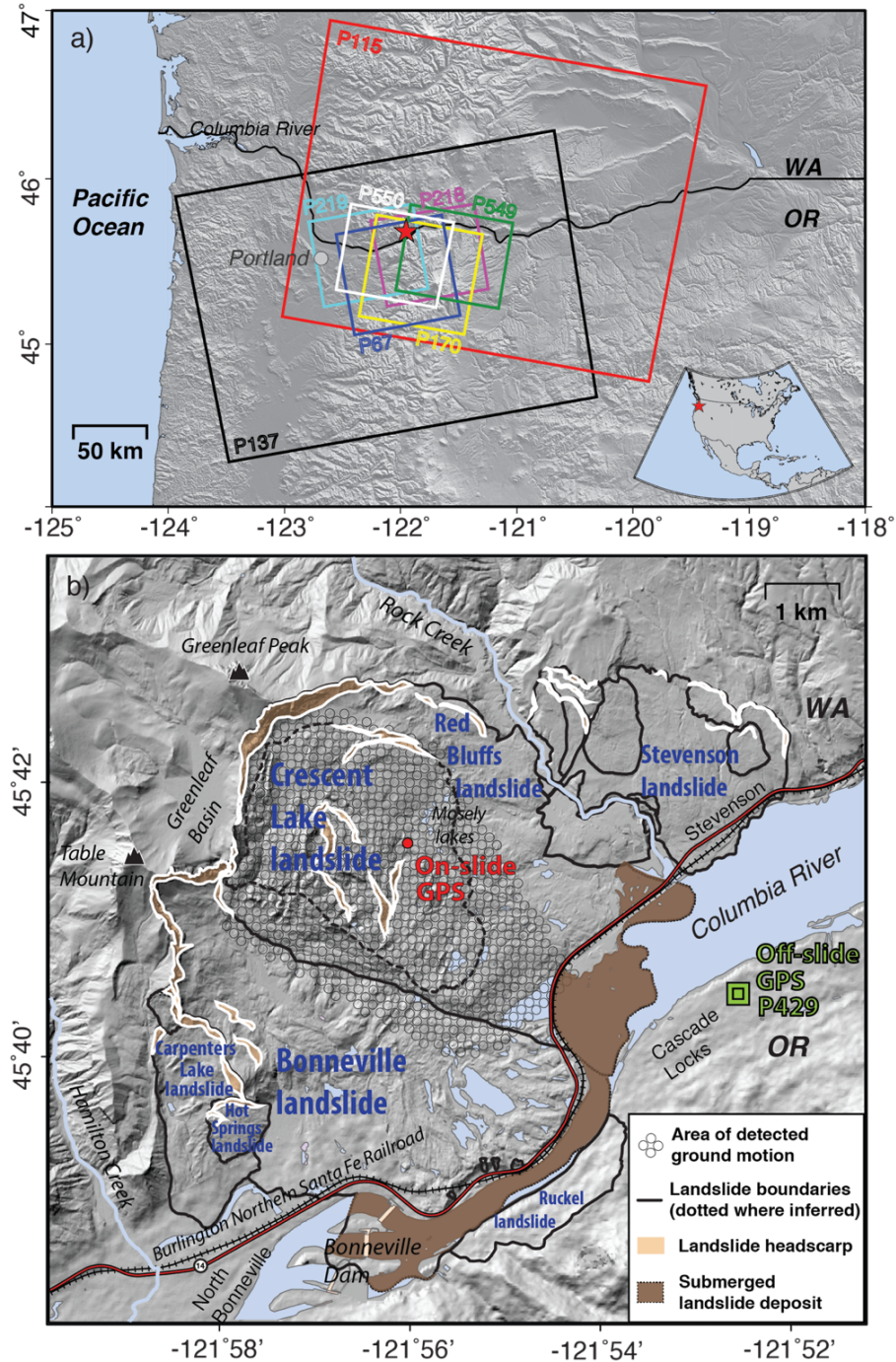


Figure 2.1 Geographic maps of the Cascade landslide complex. (a) SAR data coverage; and (b) shaded relief map of the Cascade landslide complex [Pierson et al., 2016], with dashed outline of Crescent Lake landslide determined by geomorphic evidence and early InSAR interferograms. Solid black lines show other landslides within the complex. The shaded area (covered by the array of circles) encompasses the area of detected movements [Hu et al., 2016], downsampled to 100 m by 100 m grids for smoothness preservation; it is the area used for thickness inversion. The red dot marks the location of the continuous GPS station that provided the data for this study. Green square shows the location of the off-slide GPS campaign.

2.4 Methodology

2.4.1 Time-series InSAR analysis

The Crescent Lake landslide is covered with forest vegetation that is moderate to sparse in coverage density. This makes it compatible with SAR analysis, which can readily reveal creeping landslide motion in areas larger than 0.2 km² with limited vegetation cover [Zhao et al., 2012]. Previous InSAR results of ALOS-1 PALSAR-1 data suggested a cumulative ~0.7 m slope-parallel displacement of the Crescent Lake landslide during 2007-2011 [Hu et al., 2016]. However, the basal geometry at depth and its movement timing had not been investigated in the prior study. To reveal details of ground deformation and to invert for landslide body thickness, I collected multiple spaceborne SAR data, including two ascending tracks (P218 and P219 data) and two descending tracks (P549 and P550 data) acquired by ALOS-1 PALSAR-1 from 2007 to 2011; one ascending track (P67 data) and one descending track (P170 data) acquired by ALOS-2 PALSAR-2, and one ascending track (P137 data) and one descending track (P115 data) acquired by Sentinel-1A from the end of 2014 to 2016 (Figures 2.1a and 2.2). For radar tracks with multiple images (e.g., ALOS-1's P218 and P219, and Sentinel-1A's P137 and P115), LOS displacements are retrieved by a set of interferograms with small to moderate baselines [Hu et al., 2016]. For the other tracks with a limited number of images, such as, ALOS-1's P549 and P550, and ALOS-2's P67, LOS velocity is simply derived by the single interferogram 20061118-20081123 (Bprep = -450 m), 20061020-20081025 (Bprep = -111 m), and 20150723-20141211 (Bprep = -85 m), respectively; additionally, LOS velocity of ALOS-2's P170 is generated by averaging/stacking 4 interferograms: 20150413-20150427 (Bprep = 192 m), 20150413-20160523 (Bprep = -102 m), 20150427-20160523 (Bprep = -293 m), 20160314-20160523 (Bprep = -152 m). The results from multiple images and thus dozens of interferograms are more credible than averaging/stacking from a single or merely 4

interferogram(s) as the artifacts have been largely suppressed during time-series analysis [Hu et al., 2016].

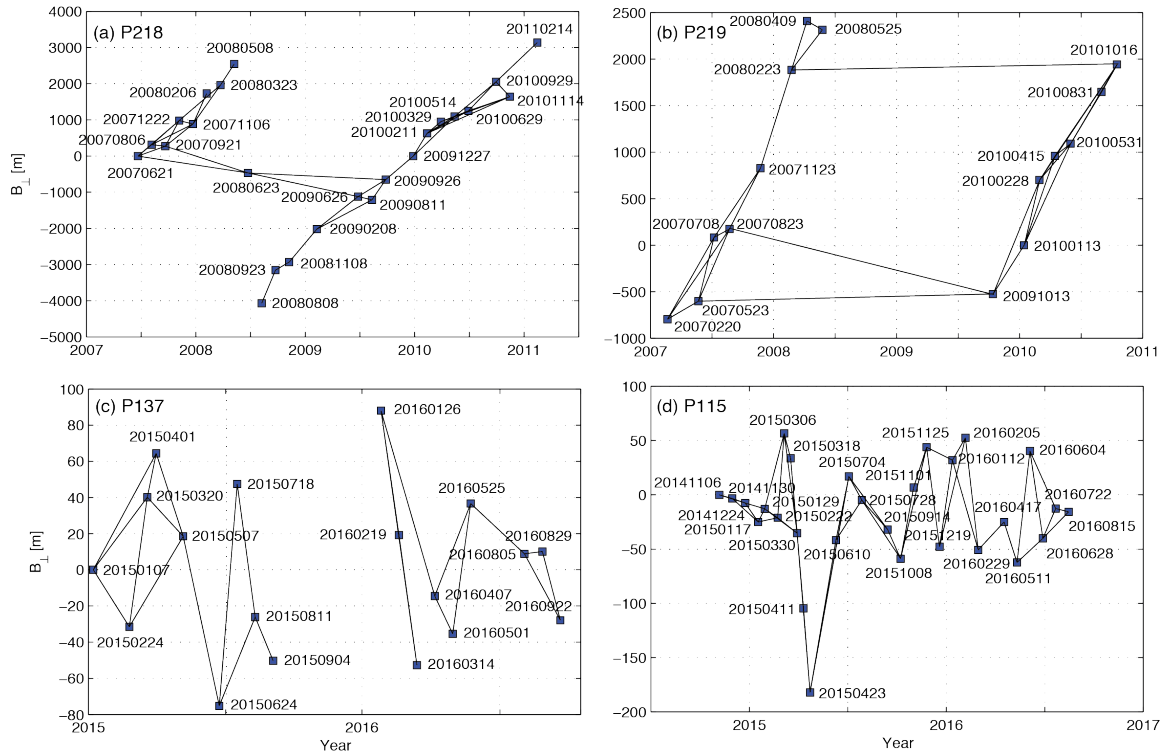


Figure 2.2 Image graph of interferometric pairs.

In order to retrieve the temporal behavior of landslide motion, I carried out time-series InSAR analysis based on unwrapped interferograms. The processing can be divided into three sections (Figure 2.3): coherent target (CT) detection, topographic error (topo-error) removal and atmospheric phase screen (APS) removal.

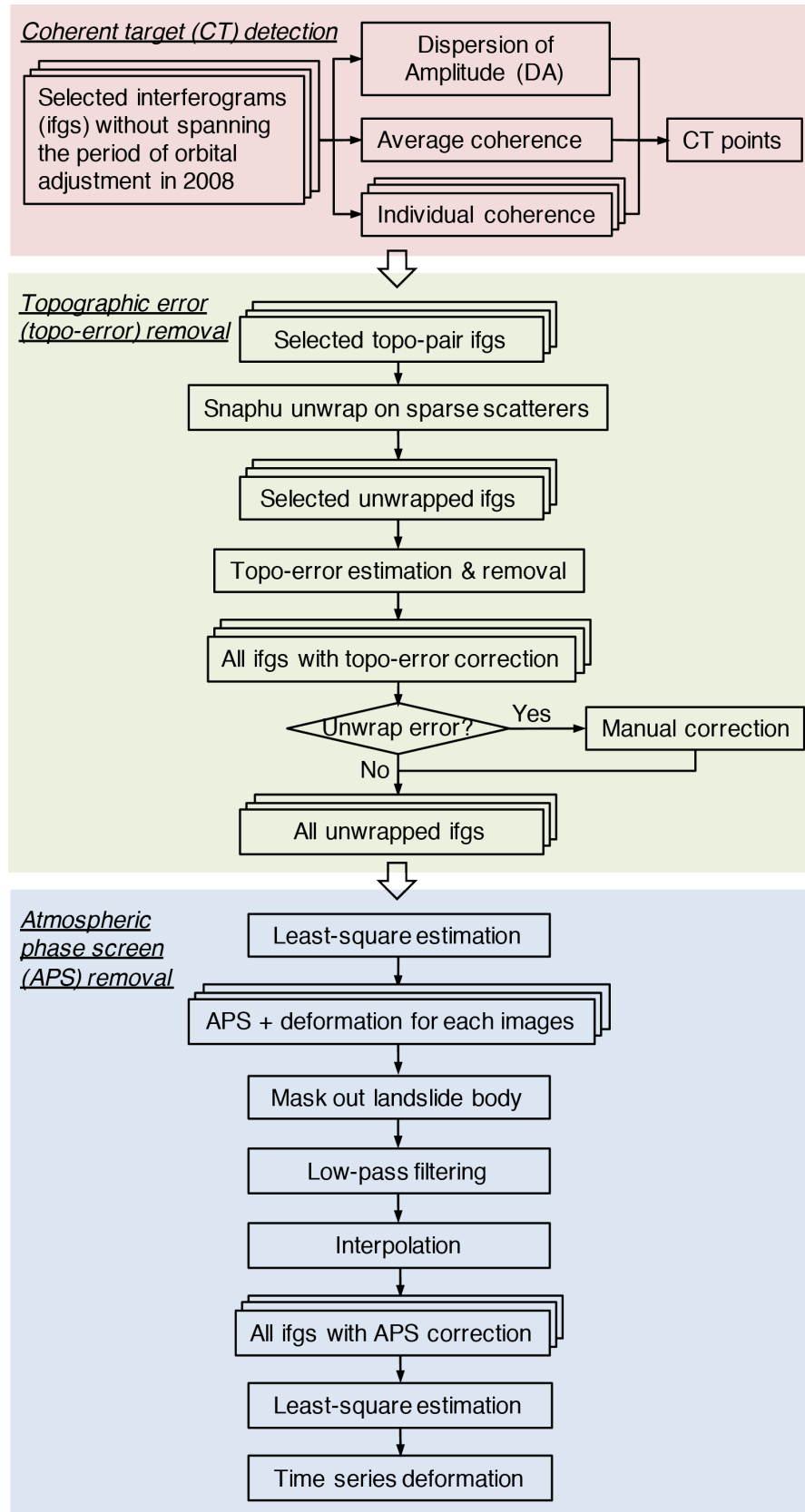


Figure 2.3 Workflow of time-series InSAR processing.

2.4.1.1 Coherent target (CT) selection

CT points are defined as pixels with high coherence and stable amplitude series in time. To separate CT points from water bodies, vegetated areas, and other sources with inconsistent scattering, I set thresholds on coherence and dispersion of amplitude (DA, the ratio between the standard deviation and the mean of the amplitude). For the case study of Cascade landslide complex, the pixels with DA less than 0.35, averaged coherence larger than 0.8, and each pixel with an individual coherence larger than 0.3 are chosen as CT points. The scarcity of CT points on the lower part of the Bonneville landslide deposit for both P218 and P219 can be explained by the existence of many lakes and dense forest vegetation. Because the study area is located on the far range of P219 swath (no data are available from P219 beyond this eastern boundary), the satellite antenna received backscattering with a lower signal-to-noise-ratio for this zone, thereby reducing the interferometric coherence. Hence, the CT points in P219 are even sparser than those in P218.

To achieve spatial consistency for each interferogram, I set up a reference assuming no deformation during the observation period. The phase value of a few reference points might be contaminated by the atmospheric effects during some acquisitions, thereby biasing the measurements of all connected interferometric pairs. Therefore, I selected the CT points at two independent residential areas in North Bonneville and Stevenson (Figure 2.1b) as the reference, where the coherence is good and the interferograms do not show fringes, and subtracted their averaged phase value from all the CT points. Note that all the following data processing is based on these discrete CT points.

2.4.1.2 Topographic error (topo-error) removal

To remove the topographic phase component from each interferogram, a 10-m-posting DEM was generated by using a 5-m-resolution LiDAR bare-earth DEM [DNR, 2005] and filling out the

remaining area with a 30-m-resolution SRTM DEM to best utilize available DEM resources. The systematic error was corrected by minimizing the elevation difference of the overlapping regions (Figure 2.4a). However, the two DEMs are still inconsistent with a large elevation difference (Figures 2.4a and b). Interestingly, the DEM difference map seems to reflect the distribution of forest vegetation, suggesting that the origin of this inconsistency may be explained by the sensors' different sensitivities to the vegetated terrain and the resulting difference in scatterer center height. SRTM used C-band radar data acquired in 2000, which is sometimes incapable of fully penetrating the tree crown in dense canopy. Therefore, SRTM-derived elevation could be situated at a level between canopy and ground surface containing (partial) tree height. On the other hand, LiDAR DEM corresponds to the bare-earth elevation in 2005. The misfits between two DEM sources can vary from pixel to pixel, and the effects are more notable in vegetated terrain. Most commonly, the differences of acquisition time, scattering centers, and the volumetric scattering effects, as well as the inaccuracy of geocoding and coregistration, contribute to such inconsistency.

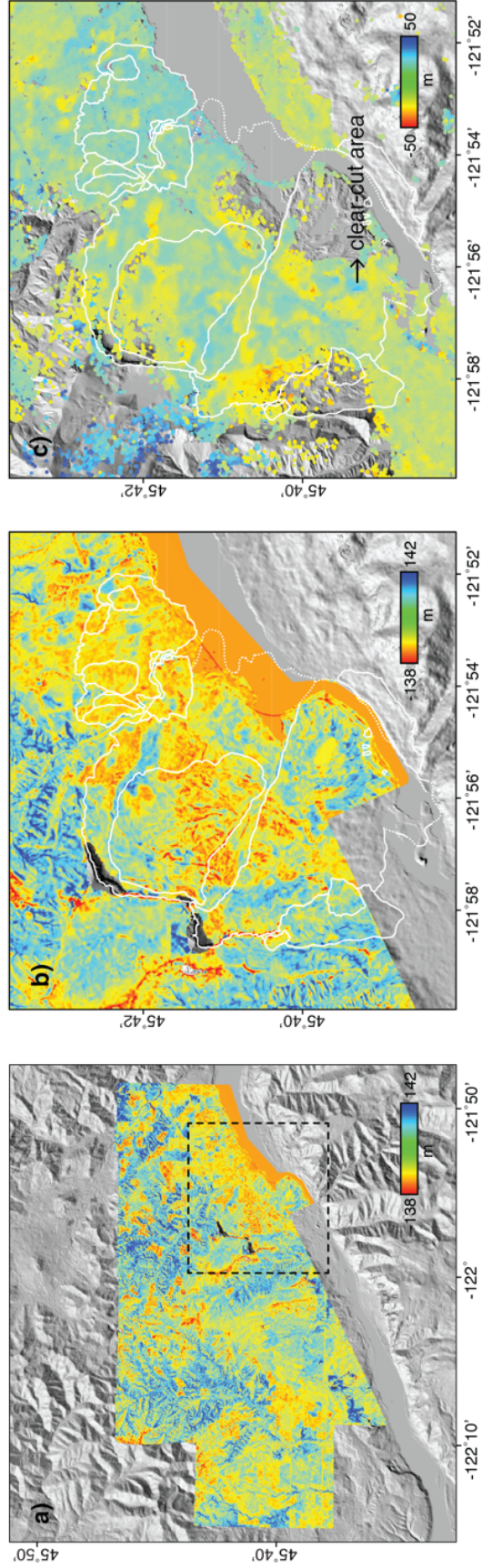


Figure 2.4 Sources of topographic error. The elevation difference map between SRTM DEM and LiDAR DEM over the DEMs overlapping area (a) and the study area (b). The study area is outlined by the dashed box in panel a. The color scales in panels a and b show the elevation difference in meters. (c) Topographic error of the merged DEM estimated by P218 and P219 datasets with respect to the merged LiDAR and SRTM DEMs. The color scale in panel c shows the topographic error in meters.

The elevation difference between the SRTM and LiDAR DEMs represents their different scattering centers, but neither of the DEMs can precisely reflect the actual scattering center of the L-band ALOS-1 data for the time-series InSAR processing. I therefore need to estimate the topo-errors before investigating the deformation signal. I first selected the interferograms (Figure 2.4) with temporal intervals within 92 days (i.e., two orbital cycles for ALOS-1 data) during dry seasons for which I assumed no deformation. Then I conducted Snaphu unwrapping on sparse CT points [Chen, 2001; Hooper, 2010], and estimated the topo-errors by analyzing the time-series unwrapped phase behavior with respect to the perpendicular baseline for each CT point. I encountered difficulty with phase unwrapping some decorrelated interferograms (e.g., the bridging data pairs of P219); in those cases, I applied manual corrections by adding or subtracting an integer number of phase cycle(s) at the phase discontinuity.

The topo-error estimations from the P218 and P219 datasets are shown in Figure 2.4c. Interestingly, the localized bluish area at the toe of the Bonneville landslide, which is only covered by the SRTM DEM, corresponds to a clear-cut area. Historic aerial images show that the logging activities have been ongoing for decades. Without topo-error correction, the fringes will result in spurious subsidence signals, as the temporal and spatial baselines are correlated for ALOS-1 data (Figure 2.2) [Samsonov, 2010]. Similar phenomena also exist in other logged areas covered only by the SRTM DEM to the east side (out of the boundary) of the study area. On the other hand, the reddish area close to the north tip of Bonneville landslide, where I used the LiDAR DEM, corresponds to a vegetated hillslope facing east. Without topo-error correction, the estimation can be contaminated by spurious uplift signals. I removed the derived topo-error phase component on each CT from all the interferograms before phase unwrapping.

2.4.1.3 Atmospheric phase screen (APS) removal

Based on the unwrapped interferograms, I used LSE to derive time-series deformation for each point, and applied the coherence as a weighting function during the inversion. However, the deformation signals here are likely to be contaminated by APS at low frequency in the spatial domain. Hence, I masked out the landslide body and conducted low-pass spatial filtering (linear interpolation) to extract the APS signals. Based on the APS estimated on the remaining scatterers, I applied an interpolation method (e.g., the Kriging interpolation) to interpolate APS on all the CT points for each acquisition [Ferretti et al., 2001]. After removing the APS from each interferogram and applying additional LSE, the time-series deformation map was produced.

2.4.2 Mapping slope-parallel displacement using LOS measurements

InSAR can only measure the projection of the three-dimensional ground motion along the radar LOS direction while the actual sliding is generally in the slope-parallel direction. Landslides in the Cascade landslide complex are dominantly translational landslides [Palmer, 1977; Pierson et al., 2016]. For translational landslides, I can assume that the landslide basal failure planes and the surface slope are approximately parallel, so that the projection of the slope-parallel vector on the horizontal plane can be referred to as the slope aspect. Figure 2.5a illustrates two general situations given smooth slopes: one is on the slope facing the incoming radar pulses, the downslope motion corresponds to the slant range decrease; the other is on the slope facing away from the incoming radar pulses, the downslope motion corresponds to the slant range increase. In both cases, the magnitude of downslope sliding vector is always no less than that of the radar look vector. This amplification/scaling factor A of the LOS measurement when projected into the hillslope can be expressed as [Hilley et al., 2004],

$$A = 1/(l \cdot s^T) \quad (2.1)$$

where l is the radar look direction unit vector $l = [-\sin \varphi_{look} \sin \alpha_{head} \quad \sin \varphi_{look} \cos \alpha_{head} \quad -\cos \varphi_{look}]$, and s is the downslope sliding unit vector $s = [\cos \sigma_{slp} \cos \beta_{asp} \quad \cos \sigma_{slp} \sin \beta_{asp} \quad -\sin \sigma_{slp}]$, in which φ_{look} is the radar look angle, α_{head} is the radar heading angle, σ_{slp} is the slope angle, and β_{asp} is the slope aspect, α_{head} and β_{asp} are positive when rotating clockwise from the north/zero orientation (Figures 2.5b and c).

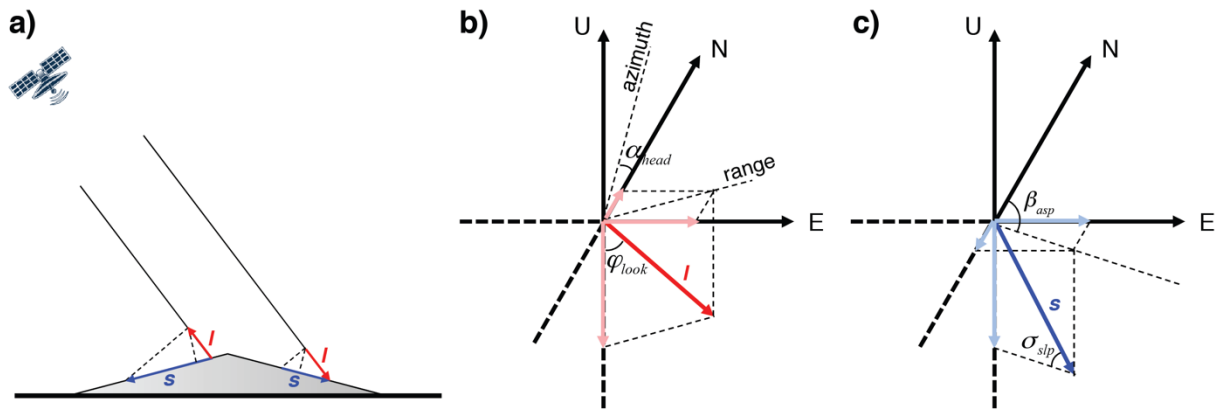


Figure 2.5 Implications of radar look angles. (a) Lateral view of the projection of radar look vector l into slope-parallel vector s . Projection corrections for (b) radar look vector and (c) slope-parallel vector in 3D space. The vectors are defined by the left-handed Cartesian coordinate system, where north, east and up directions are x, y and z axes respectively, and clockwise rotation from the axes indicates an increase in the angles.

2.4.3 Mapping a quasi-3D creeping landslide using spaceborne InSAR observations

The Crescent Lake landslide primarily moves to the southeast horizontally. However, spaceborne InSAR observations are largely insensitive to north-south motion, regardless of the orbit direction (ascending or descending). For InSAR available at the Crescent Lake landslide, the radar heading angle is $\sim 10^\circ$ and the looking direction is $\sim 80^\circ$ for ascending data, which is nearly orthogonal to the slope aspect ($\sim 170^\circ$) at the lower southeast section of the landslide (Figure 2.6). Therefore, the motion in this part of the landslide is nearly undetectable.

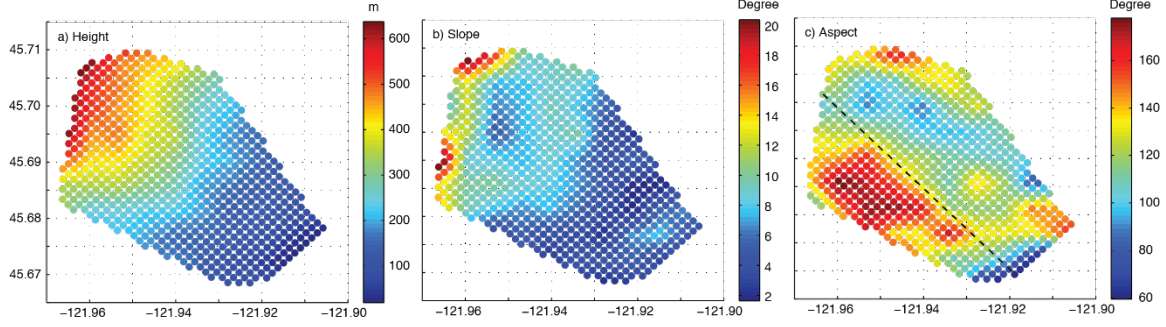


Figure 2.6 Topography information over the area of interest: (a) elevation in meters, (b) slope in degrees, and (c) slope aspect in degrees. The approximation of the basal plane is based on 500 m by 500 m downsampled DEM (sources: 5-m-resolution 2005 LiDAR bare-earth DEM [DNR, 2005] with voids filled by 30-m-resolution 2000 SRTM DEM).

Four ascending/descending tracks of SAR data were used for each observation time period. The InSAR time-series processing method detailed in section 2.4.1 was used to process ALOS-1 and Sentinel-1A datasets. For the other datasets with limited numbers of images, I used averaging/stacking to obtain their LOS velocity. Data from ascending tracks share one radar-imaging geometry, and data from the descending tracks share another. Therefore, there are essentially two independent measurements for each time period, making it difficult to constrain the complete 3D displacement fields. I therefore assume that the long-term surface movement is exclusively downslope in the direction of slope aspect on the slope-parallel basal surface under the force of gravity, i.e., motion in the cross-slope direction (v) is negligible (Figure 2.7). This assumption is supported by the observed GPS data, which indicate that v is much smaller than u (Figure 2.15). Given this constraint, I can obtain the quasi-3D displacement fields.

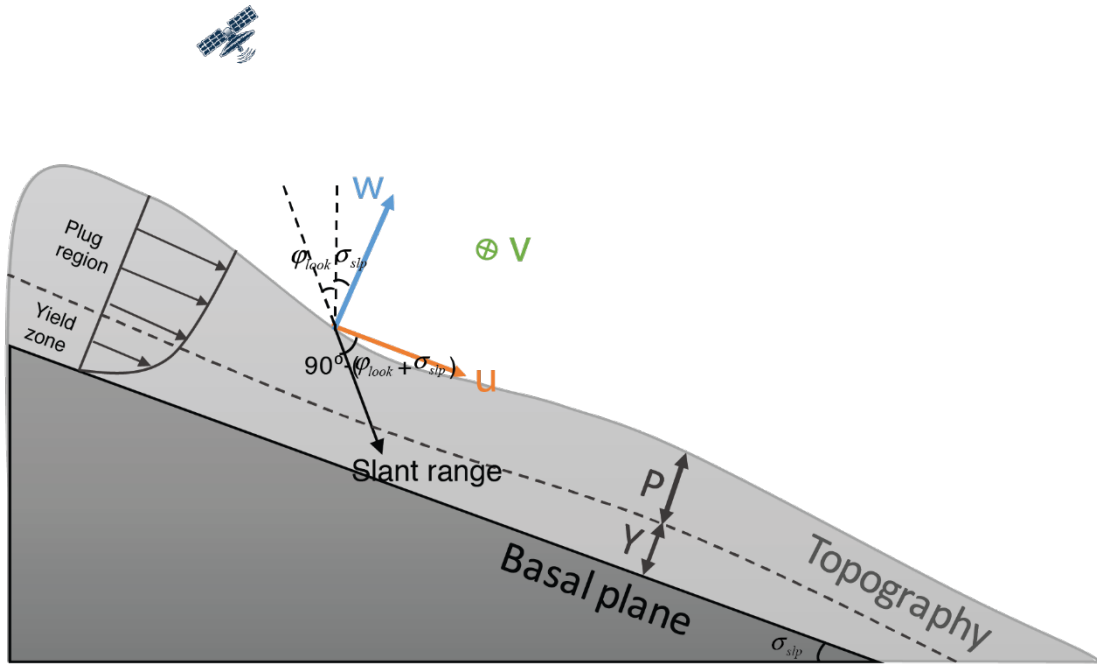


Figure 2.7 Primed coordinate system that fits on the slope-parallel/perpendicular plane.

InSAR LOS measurements LOS are given in the unprimed coordinates (north, east and up) by

$$l \begin{bmatrix} N \\ E \\ U \end{bmatrix} = LOS \quad (2.2)$$

where l is the radar look vector $l = [-\sin \varphi_{look} \sin \alpha_{head} \quad \sin \varphi_{look} \cos \alpha_{head} \quad -\cos \varphi_{look}]$, φ_{look} is radar look direction, and α_{head} is satellite heading angle.

Although I have four LOS measurements of two ascending passes and two descending passes, the look vectors of the same orbit direction are similar. Therefore, I essentially only have two independent measurements, which are insufficient to solve for the three unknowns of the 3D displacement vector.

To better explain the solution, I introduce the primed coordinate system that fits on the slope-parallel/perpendicular plane (u is slope aspect that direct the largest topographic gradient, w is outwardly perpendicular to the slope plane, and v is the direction normal to u and contained in the slope-parallel plane). I assume that there is no motion normal to slope aspect u on the slope-parallel plane, i.e., $v = 0$. In other words, I add a constraint on the horizontal plane.

$$\begin{bmatrix} l_{asc1} \\ l_{asc2} \\ l_{dec1} \\ l_{dec2} \\ s_v \end{bmatrix} \begin{bmatrix} N \\ E \\ U \end{bmatrix} = \begin{bmatrix} LOS_{asc1} \\ LOS_{asc2} \\ LOS_{dec1} \\ LOS_{dec2} \\ v \end{bmatrix} \quad (2.3)$$

where s_v is the unit vector of v 's projection on the unprimed coordinates and $s_v = [\sin \beta_{asp} \quad -\cos \beta_{asp} \quad 0]$, and v is set to 0.

The primed and unprimed coordinates can be correlated using the orthogonal matrix s ($s^{-1} = s^T$),

$$\begin{bmatrix} N \\ E \\ U \end{bmatrix} = s \begin{bmatrix} u \\ w \\ v \end{bmatrix} \quad \text{or} \quad \begin{bmatrix} u \\ w \\ v \end{bmatrix} = s^T \begin{bmatrix} N \\ E \\ U \end{bmatrix} \quad (2.4)$$

where

$$s = \begin{bmatrix} \cos \sigma_{slp} \cos \beta_{asp} & \sin \sigma_{slp} \cos \beta_{asp} & \sin \beta_{asp} \\ \cos \sigma_{slp} \sin \beta_{asp} & \sin \sigma_{slp} \sin \beta_{asp} & -\cos \beta_{asp} \\ -\sin \sigma_{slp} & \cos \sigma_{slp} & 0 \end{bmatrix},$$

σ_{slp} is slope angle and β_{asp} is aspect angle.

Another way to derive N, E and U measurements is by expressing LOS measurements under the primed coordinate system.

$$T \begin{bmatrix} u \\ w \\ v \end{bmatrix} = LOS \quad (2.5)$$

where the transformation matrix T is given by

$$T = l \cdot s \quad (2.6)$$

Under the condition of $v = 0$, the third column of s can be removed, and I can solve u and w when I have two independent LOS measurements. I can then obtain the N, E and U measurements using Equation (2.4).

To prepare the input data for the inverse problem, I extract and sample all datasets covering the active Crescent Lake landslide (e.g., LOS displacements, local incidence angle, and heading angle of each radar pass) at the resolution of 100 m by 100 m grids. Assuming that the basal surface is smoother and less varied than the hummocky top surface, I also smooth the slope angle and aspect of the upper topographic surface.

2.4.4 Landslide thickness inversion

Landslide thickness can be determined from the governing equation for mass conservation, given the assumption of incompressibility, which requires the 3D velocity field to be divergence-free ($\nabla \cdot \mathbf{V} = 0$). By vertically integrating this equation between the basal slip surface and upper surface, and applying kinematic boundary conditions, a 2D governing equation is derived,

$$\frac{\partial h}{\partial t} + \nabla \cdot (h\bar{\mathbf{v}}) = 0 \quad (2.7)$$

where h is the landslide thickness, t is time, and $\bar{\mathbf{v}} = (v_x, v_y)$ is the depth-averaged horizontal velocity. This equation states that the horizontal mass flux divergence is balanced by the rate of thickness change. Calculating the approximate depth-averaged horizontal velocity, given only the

velocity at the upper surface, requires assumptions about the vertical variation of velocity through the depth of the landslide.

Proposed velocity profiles are, in part, based on rheological assumptions. The depth-averaged horizontal velocity can be related to the surface horizontal velocity \mathbf{v}_{surf} by: $\bar{\mathbf{v}} = f \cdot \mathbf{v}_{surf}$, where f depends on rheological assumptions and ranges from 0 to 1. I assume that the vertical profile of the landslide has a lower yield zone and an overlying plug region (Figure 2.7). In the yield zone, the stress equals the yield stress and the material is assumed to be deforming with a no-slip boundary condition at the basal surface, while in the plug region, the material is assumed to have little variation in velocity in the vertical direction.

I further assume that the rheology of the landslide body is spatially uniform, yielding a constant f that can be expressed as $f = 1 - \frac{Y}{3(Y+P)}$, where Y and P are the thickness of the lower yield zone and overlying plug region, respectively (Figure 2.7) [Delbridge et al., 2016]. For the case of a power law rheology, $f = 1/2$ corresponds to a linear vertical velocity profile; $f = 2/3$ corresponds to Newtonian viscous flow, such that the entire depth has yielded and the plug region vanishes; $2/3 < f < 1$ indicates plug flow (with a thin yield zone); and $f = 1$ implies a rigid sliding block with no yield zone [Booth et al., 2013]. While the inverted thickness is affected by the rheological parameter, the spatial pattern of thickness is unaffected by the uniform value of the parameter f [Delbridge et al., 2016].

Assuming that the landslide basal surface does not change over the observation period, the rate of thickness change is equivalent to the vertical surface velocity, v_z . Equation (2.7) can then be written as

$$v_z = -f \nabla \cdot (h \mathbf{v}_{surf}) \quad (2.8)$$

I invert for h by using the non-negative least squares method [Booth et al., 2013; CVX Research, Inc., 2013]. I set the upper threshold as 150 m at this site based on the thickness of an adjacent landslide [Pierson et al., 2016]. The boundary condition is that the landslide thickness vanishes at its lateral boundaries.

I discretize Equation (2.8) in the main text on a regular grid using finite difference approximations,

$$v_z(i, j) = -\frac{f v_x(i, j)}{2\Delta x} \cdot h_{i+1, j} + \frac{f v_x(i, j)}{2\Delta x} \cdot h_{i-1, j} - \frac{f v_y(i, j)}{2\Delta y} \cdot h_{i, j+1} + \frac{f v_y(i, j)}{2\Delta y} \cdot h_{i, j-1} - f \left(\frac{v_x(i+1, j) - v_x(i-1, j)}{2\Delta x} + \frac{v_y(i, j+1) - v_y(i, j-1)}{2\Delta y} \right) \cdot h_{i, j} \quad (2.9)$$

In matrix form,

$$\mathbf{v}_z = \mathbf{G} \cdot \mathbf{h} \quad (2.10)$$

where \mathbf{v}_z is a vector of vertical velocity, \mathbf{h} is the unknown landslide thickness, and \mathbf{G} is a diagonally-dominant sparse matrix (with five separated diagonals) that is formulated using the spatial sampling interval, rheological parameter, and horizontal velocities.

The thickness can be solved by minimizing the expression [Booth et al., 2013],

$$\|\mathbf{v}_z - \mathbf{G} \cdot \mathbf{h}\|^2 + \alpha^2 \|\nabla^2 \mathbf{h}\|^2$$

where α is a smoothing factor, and the double brackets indicate the Euclidian norm. A higher α renders a smoother model. During the inversion, I set α as 0.1.

2.4.5 Analysis of landslide stability and mobility

Critical to this analysis is the wetness and rainfall intensity. The wetness W is given by the ratio of the water head above the basal surface/failure plane h_w to the landslide thickness h .

Assuming that the soil matrix is cohesionless, the infinite slope stability model states that the wetness is the proportion of the soil column that is saturated at instability:

$$W = \frac{h_w}{h} = \frac{\rho_s}{\rho_w} \left(1 - \frac{\tan \theta}{\tan \varphi} \right) \quad (2.11)$$

where ρ_s is the bulk density of the soil, ρ_w is water density, θ is the local slope at the ground surface, and φ is the angle of internal friction of the soil mass at the basal surface. Analysis of the surface slope gradient and assuming a dry friction angle (~ 36 to 45°) can provide a map of maximum stable basal pore fluid pressures, relative to hydrostatic basal pore fluid pressure. The ratio is an approximation of the maximum pore fluid pressure that could be sustained without a failure.

Under the conditions of no overland flow, no significant deep drainage, and no significant flow in the bedrock, the hydrologic model states that the wetness is determined by a hydrologic ratio and a topographic ratio

$$W = \frac{h_w}{h} = \frac{q}{T} \cdot \frac{a}{b \sin \theta} \quad (2.12)$$

where q is the net rainfall rate, T is the depth-integrated soil transmissivity when saturated, a is the local upslope contributing area, and b is the contour length of the lower bound. The contributing area per unit contour length can be resolved by the D-infinite algorithm [Tarboton, 1997]. The critical steady-state rainfall is given by

$$q_c = \frac{Tb \sin \theta}{a} \cdot \frac{\rho_s}{\rho_w} \left(1 - \frac{\tan \theta}{\tan \varphi} \right) \quad (2.13)$$

Landslide mobility is an important index to characterize the relationships between volume, area, runout distance, fall height, and coefficient of friction. The best-known landslide mobility

index is L/H , where L is the runout distance and H is the elevation from the head to the flat toe area. Figure 2.8 shows the index and various best power-law fit models for diverse landslides. Another mobility index is $A/V^{2/3}$, where A is the planimetric area of the landslide. The resultant ratio of 20 is calibrated for rock and debris avalanches as well as non-volcanic debris flow. The third mobility index is given by $\rho g V H$, where ρ is the bulk density and g is gravitational acceleration. The landslide mobility indices have been empirically formulized so that I can constrain the unknown using the other known parameters. For example, I can derive the landslide thickness and thus the volume V using the approaches mentioned in section 2.4.4, and I can also obtain H from DEM, then I can estimate the potential maximum runout distance L through the empirical upper-bound linear relationship between L/H and V . The estimate of maximum L will greatly assist the decision-making process for landslide mitigation. In addition, I can evaluate the derived landslide mobility by comparing with other landslides worldwide.

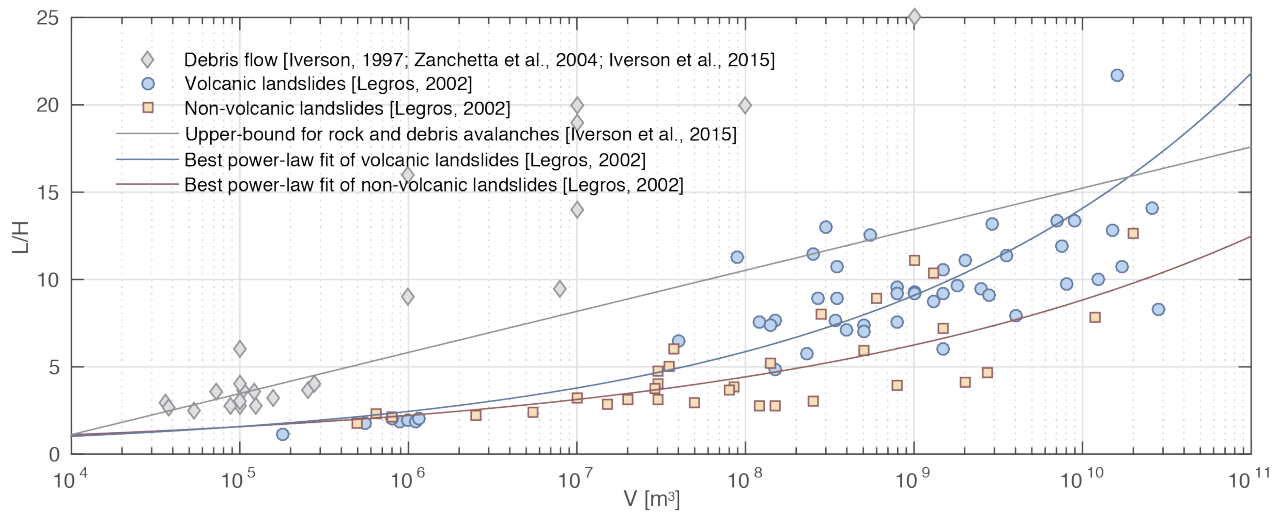


Figure 2.8 Landslide mobility index (L/H) graphs for diverse landslides, including worldwide data from Iverson, 1997; Legros, 2002; Zanchetta et al., 2004; Iverson et al., 2015.

2.5 Characterization of incipient motion of Greenleaf Basin rock avalanche

The Greenleaf Basin rock avalanche was reported to have occurred at the headscarp conjunction of the Red Bluffs and Bonneville landslides on 3 January 2008 [Randall, 2012]. Nevertheless, phase information cannot be utilized to detect this rock avalanche because of the complete loss of coherence. Instead, I extracted the scatterers along the flow path of the avalanche in areas with relatively large amplitude dispersion ($DA > 1$). The averaged time-series amplitude values of both P218 and P219 datasets on those scatterers show a sudden drop by ~ 15 decibel (dB) at the end of 2007, which may suggest the fractures might have initiated between 23 November 2007 and 22 December 2007, close to a month earlier than the reported date of rapid collapse on 3 January 2008.

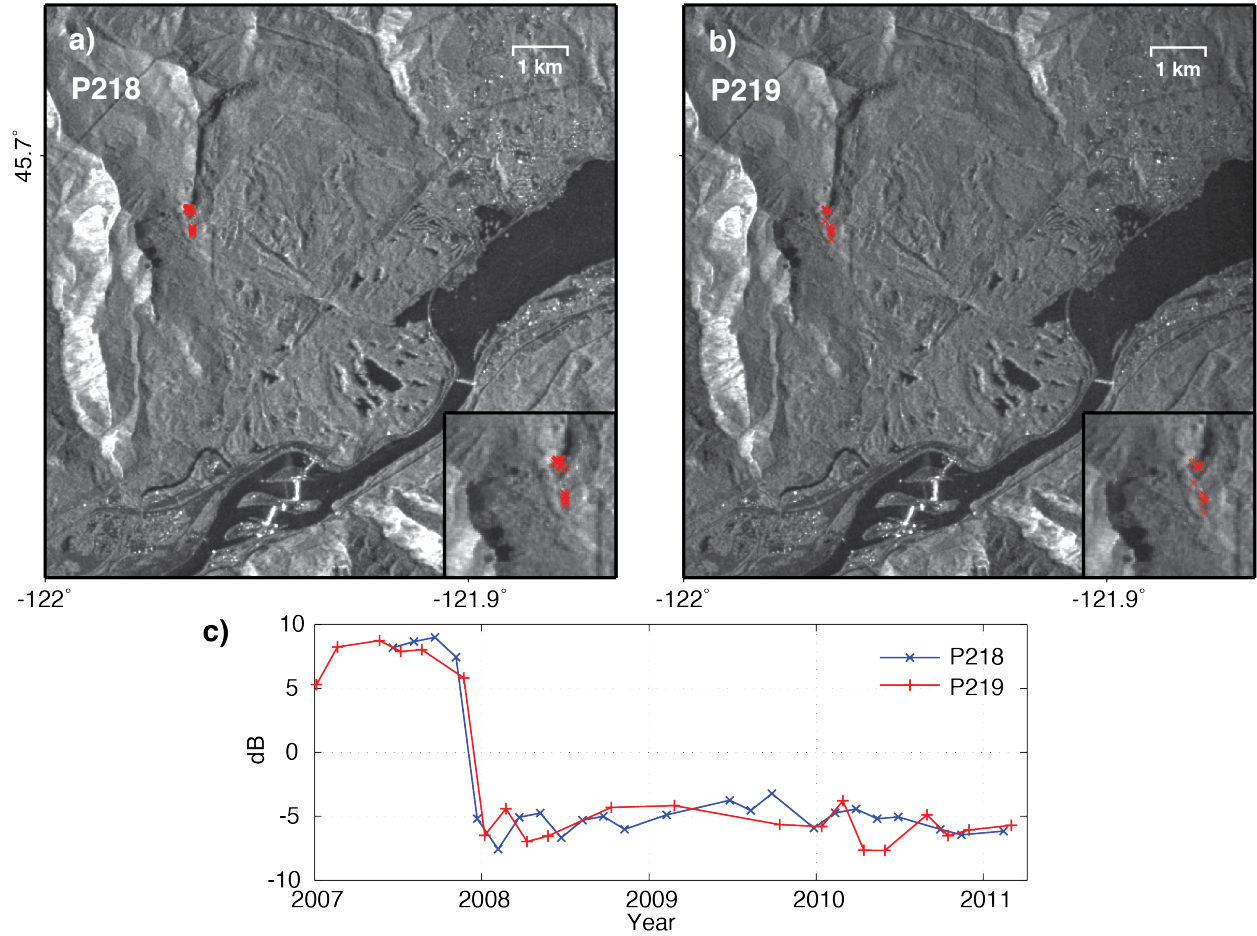


Figure 2.9 Detection of the Greenleaf Basin rock avalanche. Averaged amplitude image of P218 (a) and P219 (b) datasets. Red “X”s indicate pixels with DA larger than 1, consistent with the reported location of the Greenleaf Basin rock avalanche. Insets show the enlarged view of selected pixels. (c) Averaged time-series amplitude of those selected pixels.

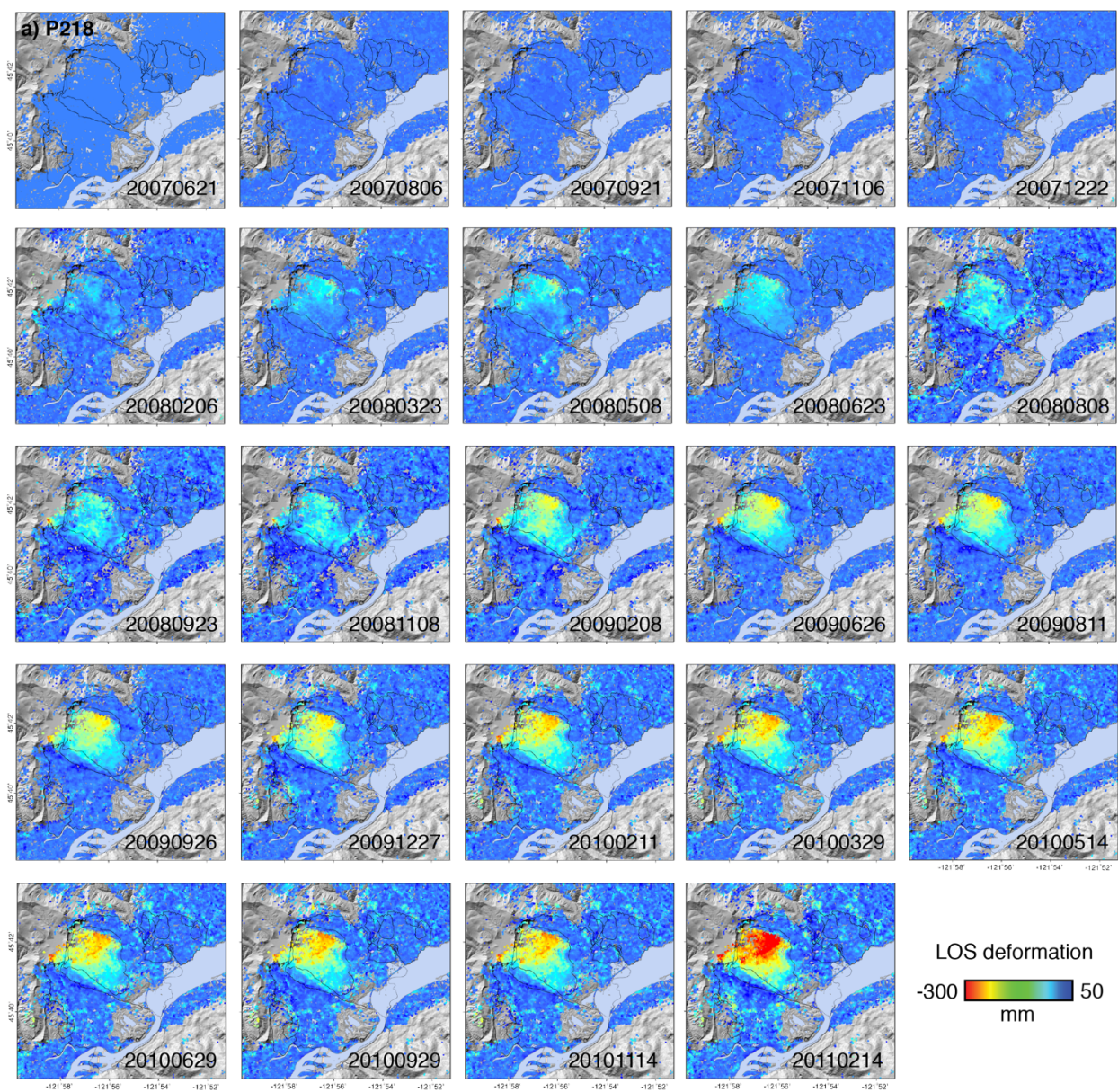
2.6 Spatio-temporal landslide motion

2.6.1 Spatial pattern of landslide motion

The landslide motion of the Crescent Lake landslide can be successfully detected using the InSAR processing strategy after DEM and atmospheric artifacts have been reduced. Figures 2.10a and b show the time-series deformation along the radar LOS, as estimated from two independent datasets P218 and P219. Although the radar geometry of these two datasets differs by 2 degrees, the temporal and spatial movement patterns are generally consistent. In general, there is subtle ground movement ($\sim 1\text{-}2$ cm along LOS) in dry seasons, and the landslide moves the most (>10

cm along LOS) during the wet seasons from November to February with a precipitation greater than ~50 cm [Randall, 2012]. The motion is not spatially uniform within the landslide; the zone of greatest movement is in the upper and northeastern parts of the landslide. This movement has formed a steep-fronted landslide toe that terminates just upslope of the Mosely Lakes (Figures 2.1b and 2.10).

Detectable ground motion also extends into the Greenleaf Basin upslope of the Red Bluffs landslide headscarp (Figures 2.1b and 2.10)—terrain that had previously been assumed to be stable. This could be the incipient movement leading to another rock avalanche. The results show that the moving area is more than 0.8 km² with an averaged cumulative LOS movement of around 200 mm, corresponding to approximately 300 mm slope-parallel movement from 2007 to 2011, and the movement mainly occurred during the wet seasons. Notably, the basin terrains relatively far from the headscarp show larger magnitude of movement than the near field, suggesting the bulk of the rock fragments may break away from a new segment in the basin, rather than along the existent headscarp like the 2008 rock avalanche. The potential avalanche could perhaps involve as much as 100 million m³, which could possibly reach important infrastructure downslope.



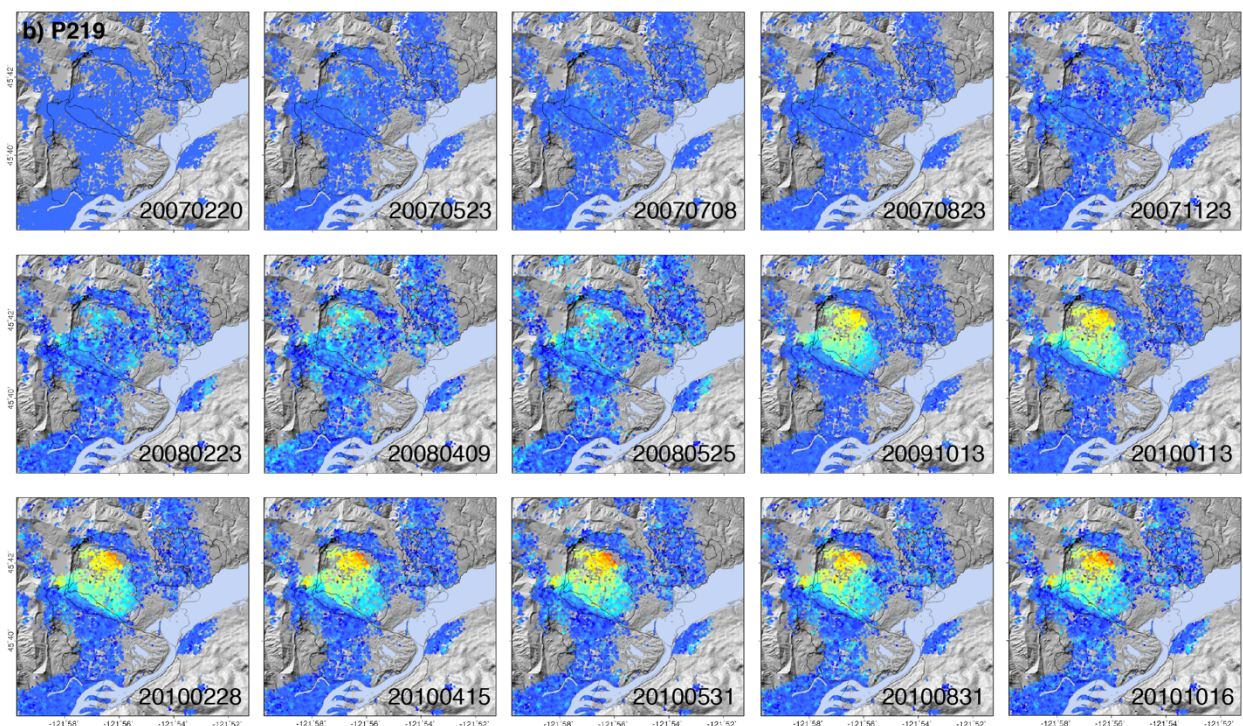


Figure 2.10 Time-series deformation along radar line-of-sight (LOS) from satellite track P218 between June 21, 2007 and February 14, 2011 (a) and from satellite track P219 between February 20, 2007 and October 16, 2010 (b). The color scale shows LOS deformation in millimeters, with areas having no deformation shown in color blue. The study area is located near the central range of P218, yet at very far range of P219. No data are available from P219 beyond this eastern boundary. The signal-to-noise ratio is lower at the far range than the central range, and thus lower interferometric coherence, resulting in a sparser CT points distribution of P219. All results are calibrated to the first acquisition on February 20, 2007.

The deformation map derived from interferograms allows us relocate parts of the Crescent Lake landslide boundaries as defined by surface morphology [Pierson et al., 2016]. Namely, the northeast and southwest boundaries should be stepped back ~ 150 m southwestward. Furthermore, the clear deformation discontinuity on the boundary between the Crescent Lake and Bonneville landslides, combined with the compressional morphologic features indicated from the hillshading (Figure 2.1b) suggest two independent and resisting basal planes for these two slides. In contrast to the Crescent Lake landslide, coherent parts of Red Bluffs, Bonneville and Stevenson landslides have remained stable during the observation period. The activity of the Hot Springs landslide and the remaining part of Carpenters Lake landslide are still undetermined due to a lack of CT points.

2.6.2 Slope-parallel movement of Cascade landslide complex

Generally, slopes in the Columbia Gorge directly face the Columbia River. Thus, the two opposite river banks have opposite aspects (Figure 2.11a). In the study region, the slope aspects reflect a divergent fan pattern from the main upland area toward the river, resulting in the angle between the aspect vector and radar look vector ranging from acute to obtuse, and therefore, the amplification factor can be either positive or negative (Figure 2.11b). When this angle reaches 90 degrees, i.e. the radar look vector and slope are perpendicular to each other, the absolute value of amplification will result in an invalid infinite number. Therefore, the amplification factors are especially undetermined around the areas of transition from blue to red, such as along Rock Creek (Figure 2.1b), the sharp topographic relief in between the east-facing slope (deep blue), and the area of deep red within the Bonneville landslide.

The study area is located in the middle range of P218, but it is on the far range of the P219 swath. Thus, the radar look vectors for the same ground target in the P218 and P219 datasets are slightly different, but the slope-parallel vectors are identical. This results in different amplification values. At location *P* for example (Figure 2.11d), the incidence angle is 38.16° for P218 and 40.53° for P219, resulting in an amplification of 1.69 for P218 and 1.63 for P219. Given the same downslope movement of 100 mm, the corresponding LOS movement will be 59 mm for P218 and 61 mm for P219.

Figures 2.11c and d show the cumulative LOS movement from P218 and the derived slope-parallel movement after applying the amplification correction pixel by pixel. Considering the possible divergence between the failure plane aspect and the surface slope aspect at any given point within the landslide, the surface slope aspect may not always point to the direction of sliding, which can lead to inaccurate amplification factors. To control the large deviations of slope-parallel

movement estimates, I culled out isolated pixels with absolute amplification values larger than a certain threshold (e.g., 5) to facilitate the interpretation. Consequently, the number of CT points in Figures 2.11c and d is less than that shown in Figure 2.11b. Nevertheless, the slope-parallel movement allows us to better identify the sliding body and improve the quantification of real motion. Besides the change in movement magnitude, the overall movement pattern after applying amplification also looks different from that of LOS measurements. Apart from the active area on the upper NE lobe of the Crescent Lake landslide, I see another area concentrated with increased movement in the upper SW part of the Crescent Lake landslide. The slope-parallel movement map suggests similar amount of total movement for the two areas.

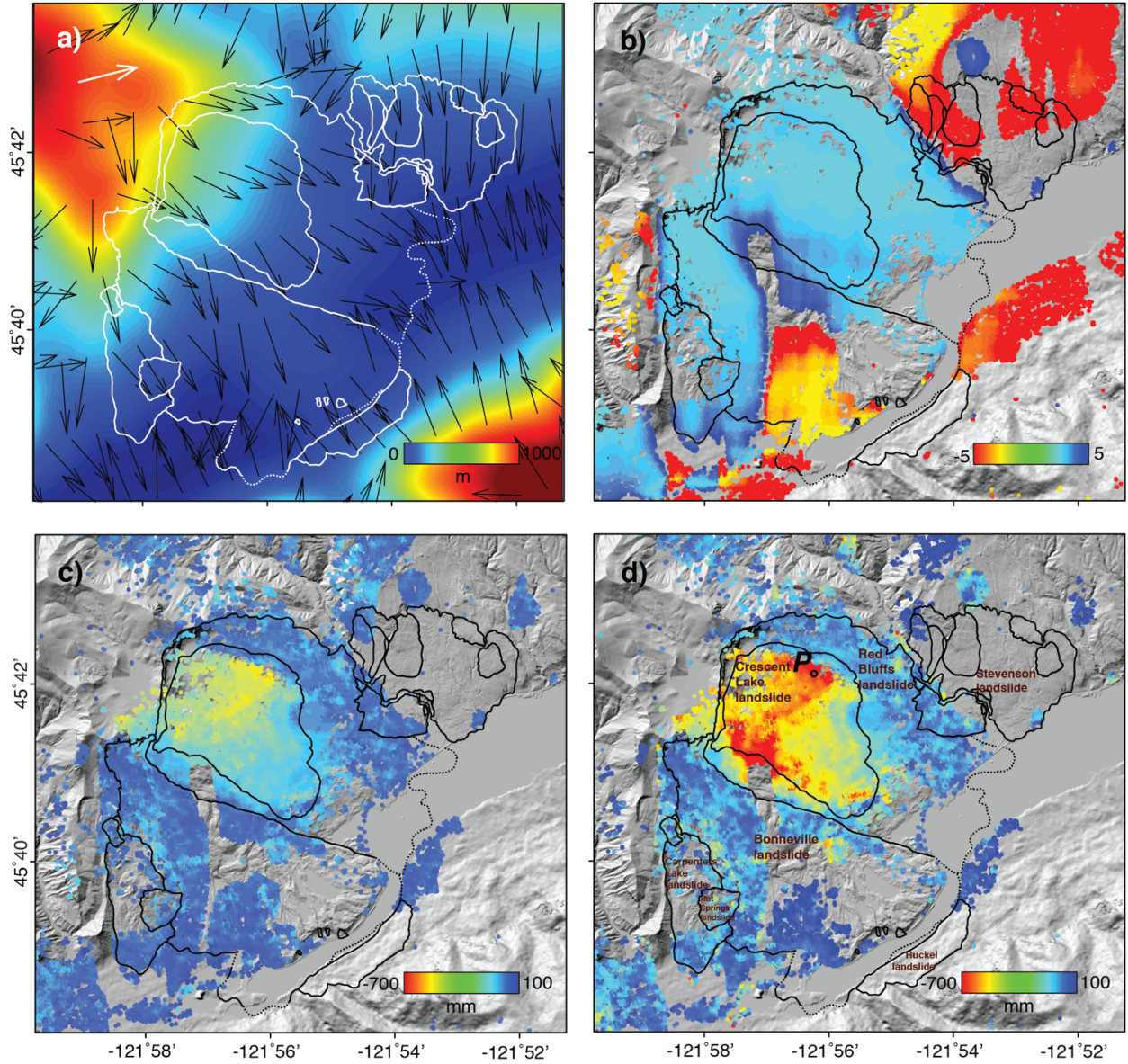


Figure 2.11 Derived slope-parallel landslide motion in the study area. (a) Slope aspects (black arrows) superposed on topography with landslide boundaries delineated by white lines. The color scale shows the elevation in meters. The white arrow on the top left corner represents radar look vector, which is nearly constant for all scatterers in the study area. (b) Amplification factor A for each CT point of P218 dataset. The color scale shows the value of amplification. Only coherent targets with amplification from -5 to 5 are plotted. Cumulative apparent LOS movement (c) and cumulative slope-parallel movement (d) from 2007 to 2011. The color scales of c and d show the movement in millimeters with stable areas shown in color blue. P is a location with active movement that is used in the analysis.

2.6.3 Seasonal deformation in response to precipitation

An advantage of data from ALOS-1 PALSAR-1 satellite passes occurring every 46 days is that correlations between landslide movement and the amount and timing of precipitation can be performed. I used singular value decomposition (SVD) [Berardino et al., 2002] to integrate time-series deformation measurements of the P218 and P219 datasets. An example at point *P* (Figure 2.11d) is shown in Figure 2.12, and the results from those two independent satellite tracks have good consistency. This active area is consistently moving away from the satellite between 2007 and 2011. The cumulative movement is 400 mm along LOS converts to as much as 700 mm movement along the slope. The increased InSAR temporal sampling made possible by integrating these two tracks will allow us to better explore landslide behavior in response to rainfall.

* Negative slope-parallel movement on the left Y-axes means the motion is downslope.

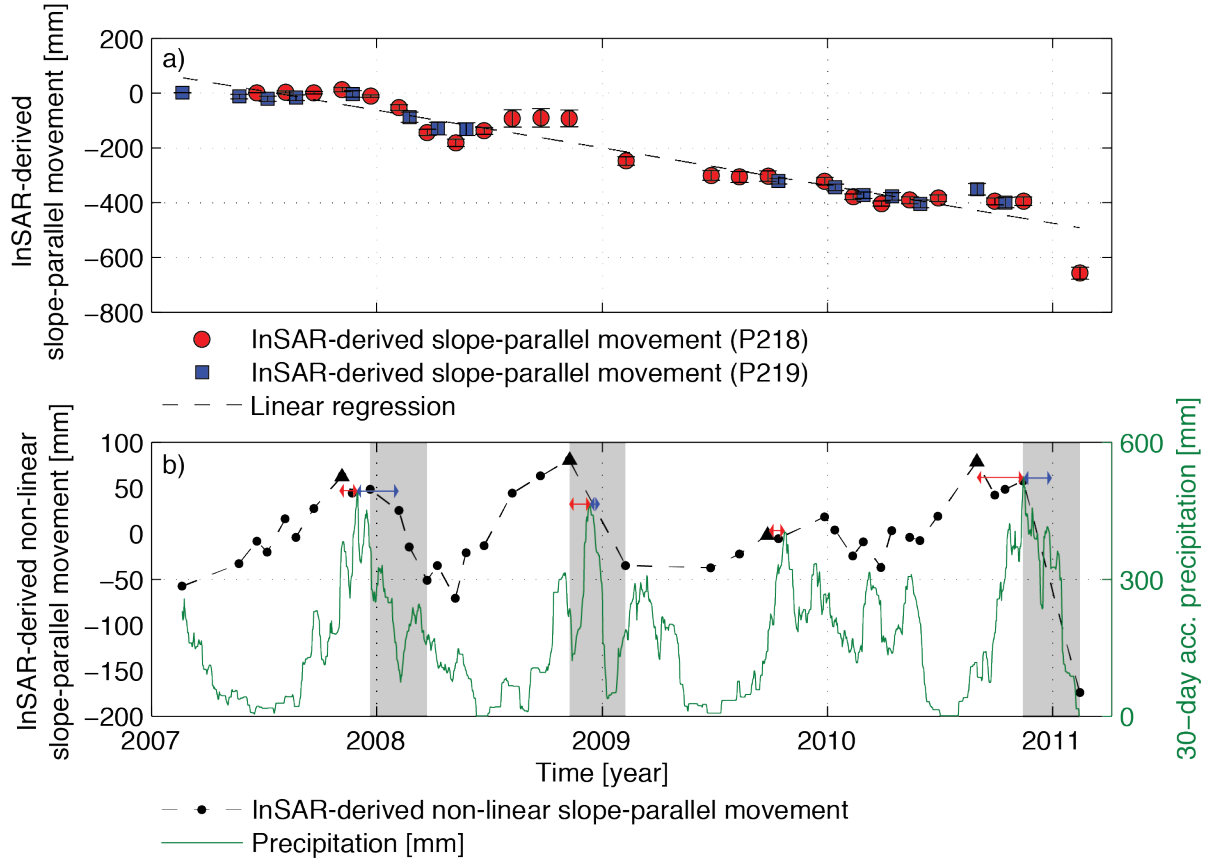


Figure 2.12 Time-series InSAR-derived slope-parallel ground motion correlating with 30-day accumulated precipitation total. (a) InSAR-derived slope-parallel movement at location P (shown in Figure 2.11d) on the active Crescent Lake landslide. All CT points within 100 meters w.r.t. location P are considered in the calculation, and their averaged phase values are used for the integration of time-series deformation by P218 (red circles) and P219 (blue squares) using singular value decomposition (SVD). The error bars represent the standard deviation (up to 33 mm) of the measurements at the selected CT points. The linear regression showing the averaged movement rate is denoted with black dashed line (same to Figure 2.13a). (b) InSAR-derived non-linear slope-parallel movement (black dashed line) compared with the precipitation records (green line). To investigate the slide motion in response to the start of rainfall season as well as rainfall volume, the residual movement (black circles) after the removal of linear component (using left Y axis from -200 to 100 mm) and the 30-day accumulated precipitation total (using right Y axis from 0 to 600 mm) have been plotted together (same to Figure 2.13b). Black triangles depict the initiation of downslope motion, red arrows show the gaps between the initiation of downslope motion and the precipitation peak, gray bars indicate the sliding acceleration timespan that can be determined by the existing measurements, in which higher data sampling rate contributes to narrower bars and more precise estimation, and blue arrows show the gaps between the precipitation peak and the midpoint of sliding acceleration (same to Figure 2.13b).

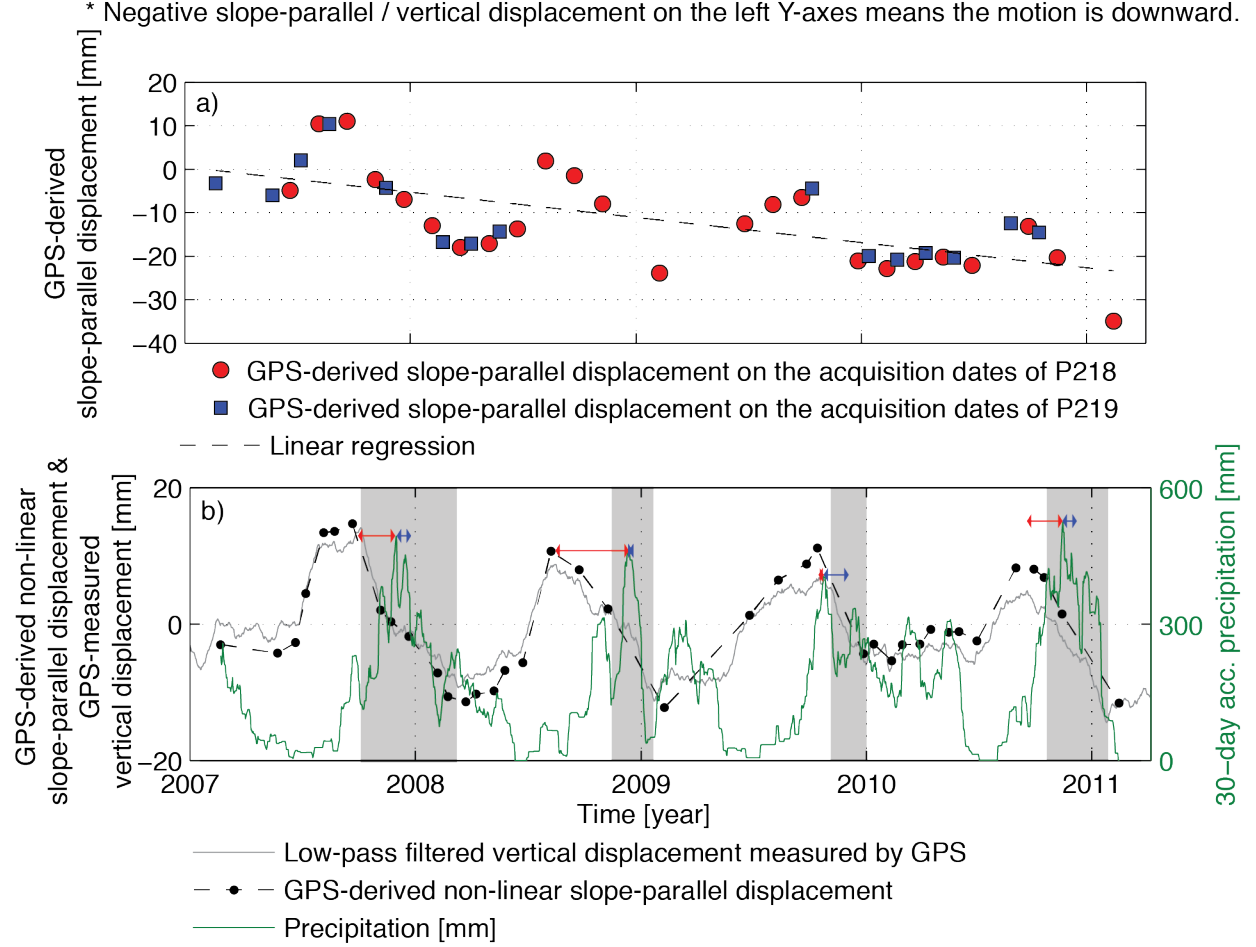


Figure 2.13 GPS-derived slope-parallel ground motion correlating with 30-day accumulated precipitation total. (a) Regional movement of a nearby GPS station unaffected by landslides is projected into the slope-parallel direction at P to reflect the regional movement component along the slope at this location. (b) GPS-derived non-linear slope-parallel movement (black dashed lines) superposed on the low-pass filtered vertical deformation (gray line), and compared with the 30-day accumulated precipitation total (green line). The difference between this plot and the one in 9 B is that the initiation of downslope motion (black triangles) and the sliding acceleration timespan (gray bars) are determined by the vertical movement measured by GPS, rather than by the non-linear slope-parallel movement obtained from InSAR.

I obtained the daily precipitation records from the Bonneville Dam meteorological station, which span the entire SAR observation period. The temporal intervals of ALOS-1 satellite passes ranged from 17 to 138 days with an average of around 40 days. To synchronize the temporal resolution of precipitation and SAR observations, I compared the slope-parallel motions with the 30-day accumulated precipitation total preceding the acquisition date (Figure 2.12b). To

investigate the seasonal kinematics of the landslide system, I removed the linear component (black dash line in Figure 2.12a) from the original InSAR-derived motion history. The positive values in Figure 2.12b mean the motion magnitude falls above the linear regression; similarly, the negative values mean the motion magnitude falls below the linear regression. The time-series deformation demonstrates clear seasonal variation, and strong correlation with the quasi-periodic 30-day accumulated precipitation total (Figure 2.12b). During the wet seasons, sufficient precipitation infiltrates and saturates the ground in the basal part of the landslide body. This saturation likely elevates the pore pressure, thereby reducing the effective stress on the skeletal matrix along the failure plane, decreasing grain-to-grain friction and effective shear strength. Meanwhile, the loading by the weight of the water in the matrix increases the gravitational driving force [Saar and Manga, 2003].

The data show that the sliding motion tends to initiate shortly after the autumn rains begin in October or November (roughly when the 30-day accumulated precipitation total exceeds 300 mm), normally one to three months ahead of the arrival of the precipitation peak (red arrows). The gaps between the precipitation peak and the midpoint of sliding acceleration are typically within two months (blue arrows). Slope movement is triggered when the shear stress exceeds shear strength.

Phenomena other than sliding also affect ground movement. During a dry season, the soil-material matrix undergoes stress release and poroelastic rebound as the soil dries during the summer and early autumn, causing a slight regional uplift, which is similar to post-glacial or isostatic rebound [e.g., Cossart et al., 2014]. In addition, GPS can detect transient near-surface mass loading by precipitation, which contributes to seasonal vertical ground oscillation in wet regions of Washington and Oregon [Fu et al., 2015]. In particular, the elastic deformation of the ground in mountainous areas (e.g., the Cascade Range) occurs with larger amplitudes than in

valley/basin areas. This is because the total precipitation accumulated during the wet seasons in the mountains at higher elevation is larger than that in the valleys/basins at lower elevation. This phenomenon can be seen at GPS station P429 (green benchmark in Figure 2.1b) at Cascade Locks across the river from the landslide complex. Assuming that the positioning data of P429 exhibit the same regional movement as the landslide study area, I derived the slope-parallel movement from GPS measurements at each SAR acquisition date using the same geometry parameters of location P that applied to InSAR results (Figure 2.13a). The non-linear component of GPS-derived slope-parallel movement was superposed on the continuous low-pass filtered vertical movement measured by GPS, and was compared with the precipitation records (Figure 2.13b). As expected, the GPS-derived seasonal slope-parallel oscillations are mainly dependent on the vertical movement (gray line in Figure 2.13b) as shown by being in phase. Both measurements derived from GPS and InSAR data depict a lower-than-average seasonal oscillation in 2010, as would be expected in a drought year [Fu et al., 2015] with lower-than-average precipitation totals. In addition, I also found that the InSAR and GPS results show fluctuations that are in phase and at similar frequency. However, the magnitude of InSAR-derived non-linear peak-to-trough slope-parallel movement (~ 120 mm) on the slide body is four times as large as that of off-slide GPS site (~ 30 mm). Inspired by the mechanism of the motion magnitude difference in mountainous and valley/basin areas [Fu et al., 2015], the exaggeration of the fluctuation magnitude on the landslide body can be explained by the fact that the GPS station at Cascade Locks site is next to the river (reservoir pool) and there is very little capacity for changes of shallow water storage under the condition of high water table; however, the landslide body has a much thicker unsaturated zone, and thus more capacity to soak up water in the winter, indicative of a magnified hydrological loading effect.

2.6.4 Validation of InSAR results using GPS data

I have acquired partially continuous GPS data from a station located in the central part of the Crescent Lake landslide (red dot in Figure 2.1b) for two periods between late 2014 to mid-2016; data were missing during the summer months of 2015. The semipermanent GPS station [Dzurisin et al., 2017] is mounted in ~5-m block of rock “floating” in landslide debris and sits at an elevation of 260 m, where the landslide has a local average slope angle of 9° and a slope aspect of 100° (measured clockwise from 0° at the north; Figure 2.6 for slope geometry; Figure 2.14 for GPS measurements in north, east and up directions).

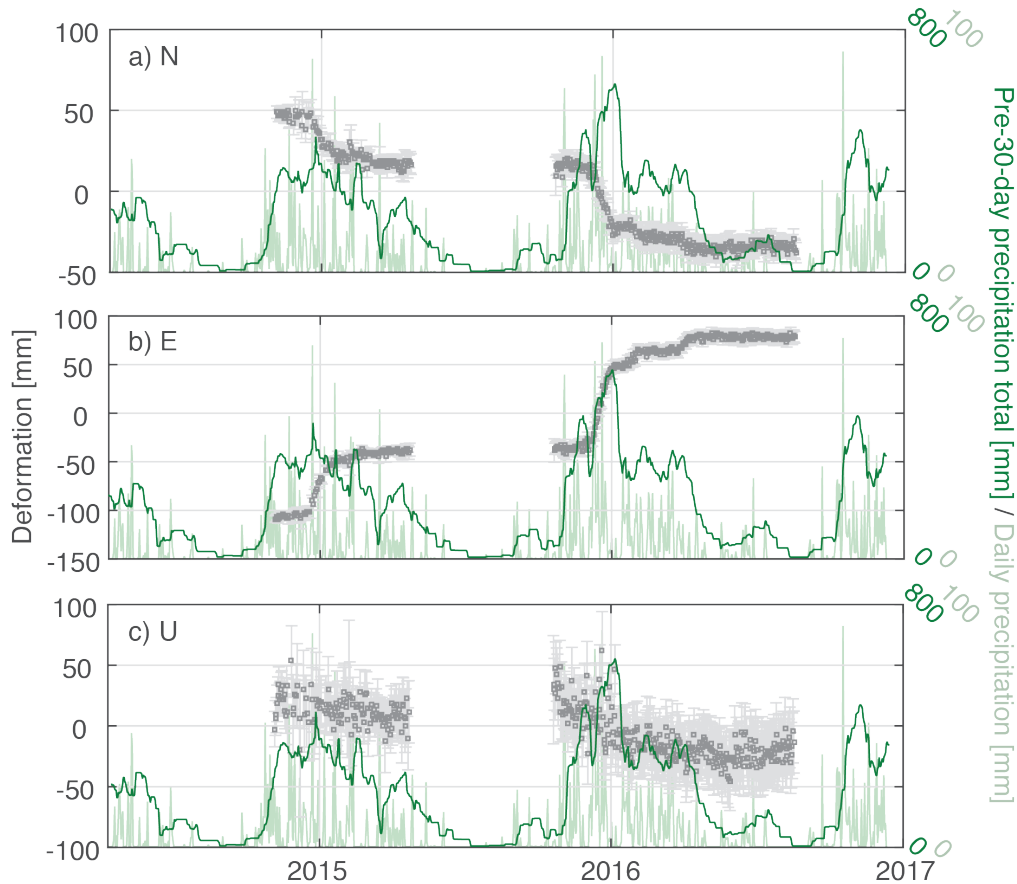


Figure 2.14 GPS displacements at the semipermanent GPS station (red dot location in Figure 2.1). (a)-(c) are measurements in N, E and U directions, respectively, along with pre-30-day and daily precipitation records.

Comparing the LOS displacements of Sentinel-1A data to that derived by GPS (Figures 2.15a and b), suggests good agreement with an average RMSD of 5.68 mm and 10.11 mm for P137 and P115, respectively. The orbit of P115 is descending, and the active lobe moves towards the satellite along the slant range, in contrast to the results of ascending orbit of P137. The high temporal resolution of Sentinel-1A data reveals a peculiar signal in the early part of the wet season (primarily November): apparent upslope or slope-normal downward motion, which is also seen in the GPS data, particularly in late 2015 (Figure 2.14).

To further investigate this anomalous movement, I transform the GPS measurements to the slope-fit coordinates (see Figure 2.7 for the coordinate systems, and Figures 2.15c-e for GPS results). Generally, v (normal to slope aspect and contained in the slope-parallel plane) is approximately northward, u (slope aspect of the largest topographic gradient) is approximately eastward and w (normal to slope plane) is approximately upward. The precursory motion doesn't show in the u component, indicating that there is no actual upslope motion; the phase change is detectable only in v component. However, the magnitude is only around 10 mm, much less than what is expressed in LOS by nearly 50 mm. These results suggest that the early wet season signal must be the result of subsidence.

The precursory slope-normal subsidence and the subsequent downslope movement of the landslide mass have been clearly captured by the descending Sentinel-1A satellite. This is because slope-normal subsidence corresponds to slant range increase (movement away from the satellite), and the downslope motion corresponds to slant range decrease (movement toward the satellite). The descending LOS measurements pick up the motions well, because the satellite LOS is looking nearly straight at the direction of oncoming landslide motion.

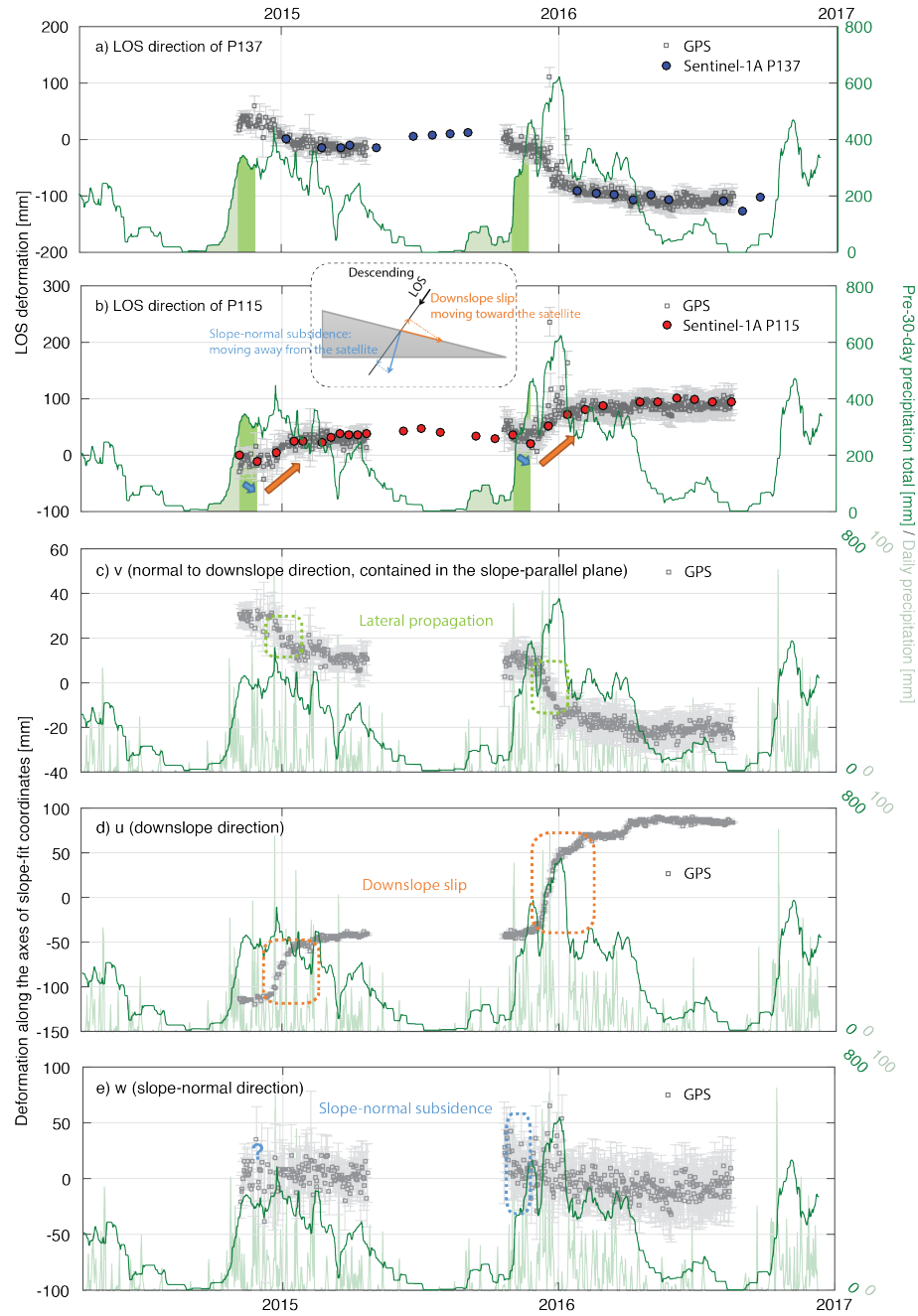


Figure 2.15 GPS displacements at the semipermanent GPS station (red dot in Figure 2.1b), projected onto the LOS direction in comparison with the Sentinel-1A measurements of (a) ascending track P137 and (b) descending track P115, along with pre-30-day precipitation total (30-day cumulative precipitation before the assigned date) from a nearby weather station (Cascade Locks, Oregon). Light green shading under the pre-30-day precipitation curves shows the antecedent rainfall period, and the dark green shading corresponds to the period of slope-normal subsidence when the precipitation is more intense. The inset diagram shows how ground displacement is sensed by a right-looking satellite on a descending track. (c)-(e) GPS measurements with the corresponding components on u , v , and w directions based on the slope-fit coordinate system, along with pre-30-day and daily precipitation records.

2.6.5 Quasi-3D displacement fields

Figure 2.16 shows the LOS deformation velocity over the active Crescent lake landslide for each radar path. The first row shows the results of ascending data and the second row is for descending data, so the area of interest is moving in opposite trend.

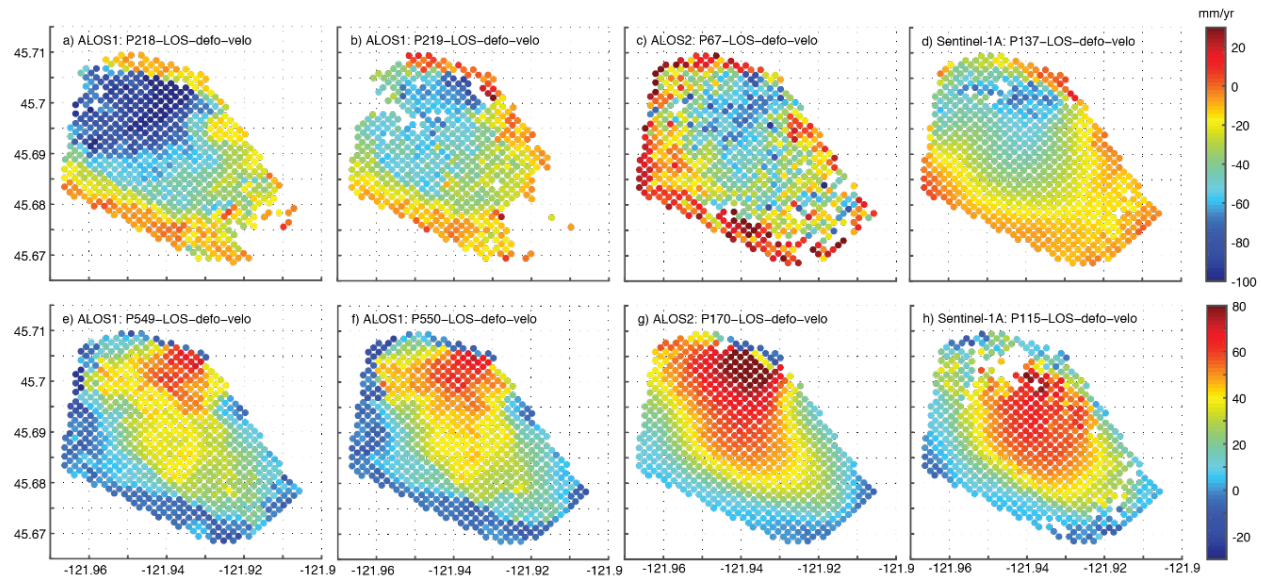


Figure 2.16 LOS deformation velocity in mm/yr over the area of interest. The figures in the first row show the results of ascending data: (a) P218 of ALOS1, (b) P219 of ALOS1, (c) P67 of ALOS2 and (d) P137 of Sentinel-1A. The figures in the second row show the results of descending data: (e) P549 of ALOS1, (f) P550 of ALOS1, (g) P170 of ALOS2 and (h) P115 of Sentinel-1A. The left four figures, (a), (b), (e) and (f) correspond to the time period of 2007-2011, and the right four figures, (c), (d), (g) and (h) correspond to the time period of 2015-2016.

I use the estimated LOS velocity of each dataset to define the quasi-3D displacement field (horizontal and vertical movement) for the Crescent Lake landslide (Figure 2.17). Horizontal motion over much of the landslide, shown by velocity vectors, is divergent away from the approximate center line of the landslide. Along the southwest margin of the slide, motion is primarily to the south and deviates nearly 45° from the average direction of movement. Along this margin the Crescent Lake landslide appears to be overlapping onto the older Bonneville landslide deposit, based on the morphologic appearance of this lateral margin [Pierson et al., 2016] and on

an abrupt change in landslide thickness along a lineament, where velocity changes direction and magnitude. Vertically, localized subsidence is clearly evident across the entire upper part of the landslide (particularly in 2007–2011), and along much of the southwest margin. Additionally, several localized zones near the mapped toe of the landslide exhibit some localized uplift. Uplift along the northeast margin during 2007–2011 (but with different vertical motion in 2014–2016) might reflect tilting of one or more large slide blocks.

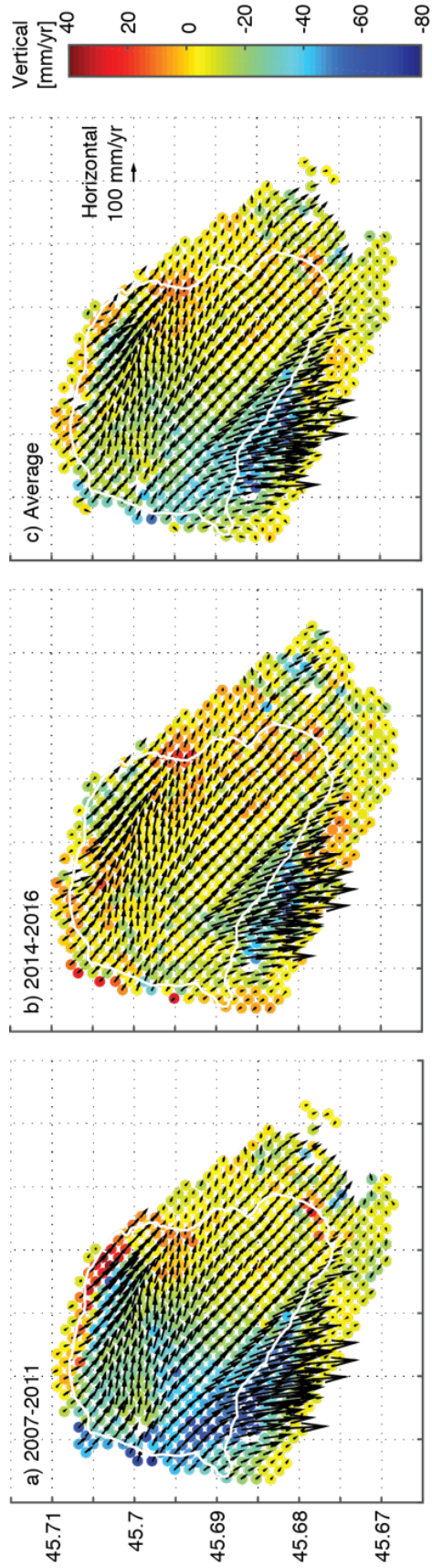


Figure 2.17 Quasi-3D displacement velocity maps in unit of mm/yr during (a) 2007-2011, (b) 2014-2016 and (c) the average of 2007-2011 and 2014-2016 of the shaded zone shown in Figure 2.1b. Horizontal velocity vectors indicate direction (effectively imposed by topographic slope) and magnitude of horizontal displacements, and color shows magnitude of vertical displacements. The solid line shows the mapped boundary of the Crescent Lake landslide [Pierson et al., 2016].

2.7 Active landslide thickness

The landslide thickness inversion model, derived from mass conservation, requires an inferred displacement field on the topographic surface, and it is based on the assumption that the motion occurs above a basal surface. The displacement velocity of each time period (2007-2011 and 2015-2016) is derived from four LOS measurements, in which both time frames contain two LOS measurements from a limited number of interferograms of relatively lower coherence. Therefore, to minimize the uncertainty in the deformation measurements, I use the average displacement field from the two time periods.

The inversion results indicate that Crescent Lake landslide is thickest (assumed up to 150 m) in a wide band across the middle of the landslide that strikes across the topographic surface slope (Figure 2.18). The area outside of the active slide on the southwest margin has been masked out (cross-hatched zone in Figures 2.18a-c). Within the boundaries of the mapped landslide (solid line in Figures 2.18a-c), the thick zone terminates abruptly against a southeasterly trending subsurface escarpment (immediately left of the dashed line). Longitudinally the landslide thins toward its head and its toe areas.

Use of a larger f value (more plug region and less yield zone) yields smaller thicknesses for the same displacement fields. The results render landslide volume estimates of 6.6×10^8 , 7.8×10^8 , and 8.2×10^8 m³ for f value equals to 1, 1/2, and 2/3, respectively, and assuming a maximum thickness of 150 m and unbiased slope and aspect angles (Table 2.1). The results are on the same order as the estimated volume (6.5×10^8 m³) of the active part of the Red Bluff landslide (i.e., the Crescent Lake landslide) by Randall [2012]. The inversion-derived basal surface is hummocky (Figures 2.18d and e). This is realistic because most of the landslides in this area have slid onto hummocky deposits of older landslides [Pierson et al., 2016]. I obtain a longitudinal thickness

profile of the landslide (transect at dashed line) by determining the elevation of the basal surface as the smoothed surface elevation minus the derived thickness (Figure 2.18f). Surface slope aspect along this transect is fairly uniform. The dependence of basal surface depth on f is more pronounced in the downslope part of the profile.

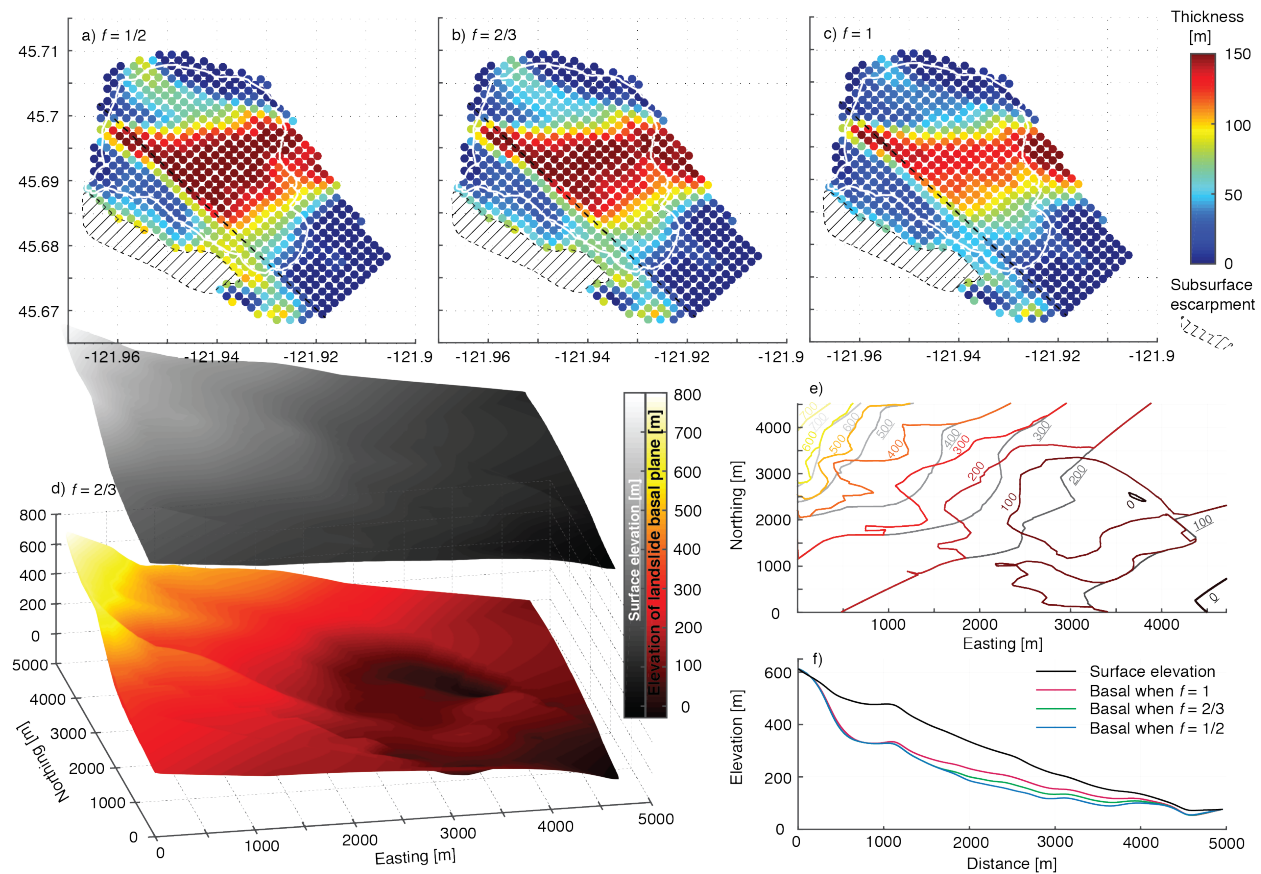


Figure 2.18 Thickness variation of the Crescent Lake landslide, obtained by inversion of the quasi-3D displacement field. Thickness is shown in meters when (a) $f = 1/2$, (b) $f = 2/3$, and (c) $f = 1$, respectively. The solid line shows the mapped boundary of the Crescent Lake landslide [Pierson et al., 2016], and the cross-hatched zone marks the area outside of the southwest margin of the landslide. (d) Geometry of the smoothed landslide top surface and basal surface when $f = 2/3$. Note that the boundaries of the topographic ground surface and the basal surface are superimposed, but the topographic ground surface is raised to better reveal the basal surface variations. (e) Elevation contours of the smoothed slope surface (gray lines and underlined digits) and the basal surface (colored lines and digits). (f) Profiles of surface elevation and landslide basal surface elevations along the dashed-line transect.

2.8 Landslide stability and mobility

I assumed that $\rho_s = 1800 \text{ kg/m}^3$, $\varphi = 45^\circ$, $T = 65 \text{ m}^2/\text{d}$. According to the daily precipitation data at the Cascade Locks, the rainfall rate q was set as 1 mm/d, 50 mm/d and 100 mm/d to calculate the stability under different rainfall conditions. Some headscarp areas are unconditional unstable (red areas in Figure 2.19c). The other unstable areas (yellow areas in Figure 2.19c), expressing as irregular linear features, are concentrated in the most deforming central to upper lobes.

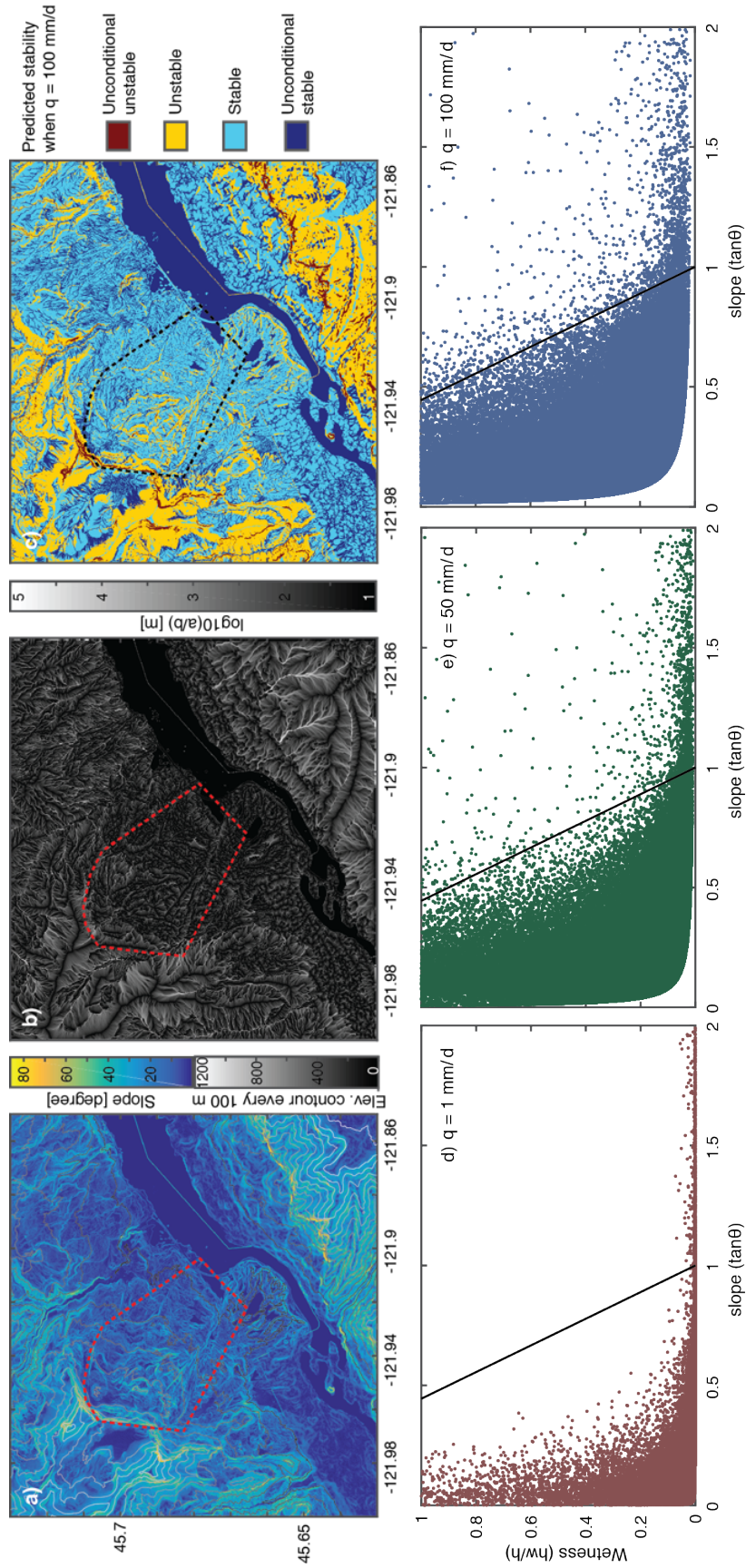


Figure 2.19 Wetness analysis at Crescent Lake landslide (outlined by the dashed lines in a-c). (a) Topographic slope superimposed by elevation contours. (b) Spatial pattern of the topographic ratio a/b . (c) Map of predicted stability when $q = 100$ mm/d. (d)-(f) Plots of wetness versus slope within the area of interest (dashed lines in a-c) when $q = 1$ mm/d, $q = 50$ mm/d, and $q = 100$ mm/d, respectively.

Based on the inversed results of landslide basal surface, the landslide volume V ranges between $7.1\sim 8.4\times 10^8\text{ m}^3$ when $f = 2/3$. I also know that the elevation difference H between the head and toe is 550 m. Referring to the empirical upper-bound linear relationship between the landslide mobility index L/H and V [Iverson, 2015], the maximum L can reach 7150 m ignoring the bounding river, which is about 1000 m larger than the sum of the planimetric length of the landslide (5000 m) and the river width (1200 m) at the toe, suggesting that a highly mobile runout at this landslide could potentially block the river.

2.9 Discussion and conclusions

The Crescent Lake landslide is a moderately large ($\sim 4\text{ km}^2$), seasonally active, translational landslide in forested terrain, the motion of which would be difficult to characterize using standard geophysical methods. I implemented the specific time-series InSAR method to extract various artifacts contaminated the deformation fringes in landslide landscape. I have investigated the hydrologically driven landslide dynamics of Cascade Landslide Complex, WA. Results show that the active Crescent lake landslide has moved 700 mm along the slope from 2007 to 2011, while other slide bodies are generally stable. The pace and amplitude of the seasonal deformation can be quantitatively correlated with the intensity of precipitation, suggesting a hydrologically driven landslide dynamic. I also used spaceborne InSAR analysis to augment data from a semipermanent GPS station to track motion of the landslide over two wet seasons. InSAR analysis offers major advantages in characterizing kinematics of a complex landslide: (a) motion of the whole landslide can be evaluated, not just motion at a few points; (b) temporal and spatial resolution of variations in motion can be determined at a weekly or biweekly scale that allows the seasonal and transient movements to be captured; and (c) variations in landslide thickness can be determined by ground

displacement measurements at a scale that allows the complexity of the landslide basal surface to be characterized.

Spatial variations in surface movement of the landslide are complex. The field of InSAR-derived ground-surface movement is larger than the previously mapped area of the landslide, which was defined on the basis of geomorphic features visible in LiDAR imagery [Pierson et al., 2016]. Variable amounts of subsidence during sliding occur primarily in the upper half of the landslide body, which correlates strongly with zones of accelerated horizontal movement. Accelerated sliding is also evident along the southwest lateral margin, where the landslide laps onto the older Bonneville landslide deposit and thins substantially. Horizontal surface motion vectors vary in magnitude from nearly zero to about 350 mm/yr and vary in direction by nearly 90°.

2.9.1 Biases in 3D displacements and thickness inversion

I propose a method to derive quasi-3D displacement fields using two independent spaceborne InSAR measurements (ascending and descending) that could have applications for studying other deforming bodies (glaciers, volcanic cones, natural dams, etc.). Determination of displacement fields also allows variations in active landslide thickness to be approximated, based on mass conservation and assuming a homogeneous deforming mass. Depth-averaged horizontal velocities are approximated from surface velocities using the rheological parameter f . The assumption of downslope motion, taking as the reference for the derivation of quasi-3D displacements, is in essence based on the topography, or more specifically, the angles of slope and aspect at each target. Assuming that the uncertainty of slope and aspect is in ± 3 degrees, the consequent landslide average thickness and volume (e.g., $f = 2/3$) can vary by about 8% (Table 2.1), yet the spatial patterns of landslide thickness are not changed much (Figure 2.20). In addition to the input

displacement maps, the thickness approximations depend on: (a) choice of the rheological parameter f , which is essentially a scaling factor; (b) assigned landslide areas and boundary conditions, which assert that the landslide thickness and motion vanish at the lateral margins; and (c) a priori knowledge or estimation of maximum landslide thickness. The results show that the thickest part of Crescent Lake landslide is approximately in the middle and that there are abrupt changes in thickness, likely reflecting underlying topography.

Table 2.1 Summary of 3D displacements, landslide thickness and volume due to the uncertainty in angles ($\pm 3^\circ$) of slope and aspect.

Slope [°]		Original	+3	+3	-3	-3
Aspect [°]		Original	+3	-3	+3	-3
Avg. N [mm/yr]		-28.6642	-31.0987	-25.2545	-31.6559	-25.7208
Avg. E [mm/yr]		50.0668	46.8905	53.2843	47.5806	54.1703
Avg. U [mm/yr]		-11.1393	-14.2802	-14.2802	-8.1548	-8.1548
f = 1/2	Avg. thickness [m]	73.5706	73.1607	78.3534	68.1935	70.8567
	Volume [$\times 10^8$ m³]	8.1958	8.1501	8.7286	7.5968	7.8934
	Thickness/volume change w.r.t original		-0.56%	6.50%	-7.31%	-3.69%
f = 2/3	Avg. thickness [m]	69.8656	70.7487	75.4428	63.7134	65.3924
	Volume [$\times 10^8$ m³]	7.7830	7.8814	8.4043	7.0977	7.2847
	Thickness/volume change w.r.t original		1.26%	7.98%	-8.81%	-6.40%
f = 1	Avg. thickness [m]	59.1270	62.4629	67.5616	47.8301	51.5556
	Volume [$\times 10^8$ m³]	6.5868	6.9584	7.5264	5.3283	5.7433
	Thickness/volume change w.r.t original		5.64%	14.27%	-19.11%	-12.81%

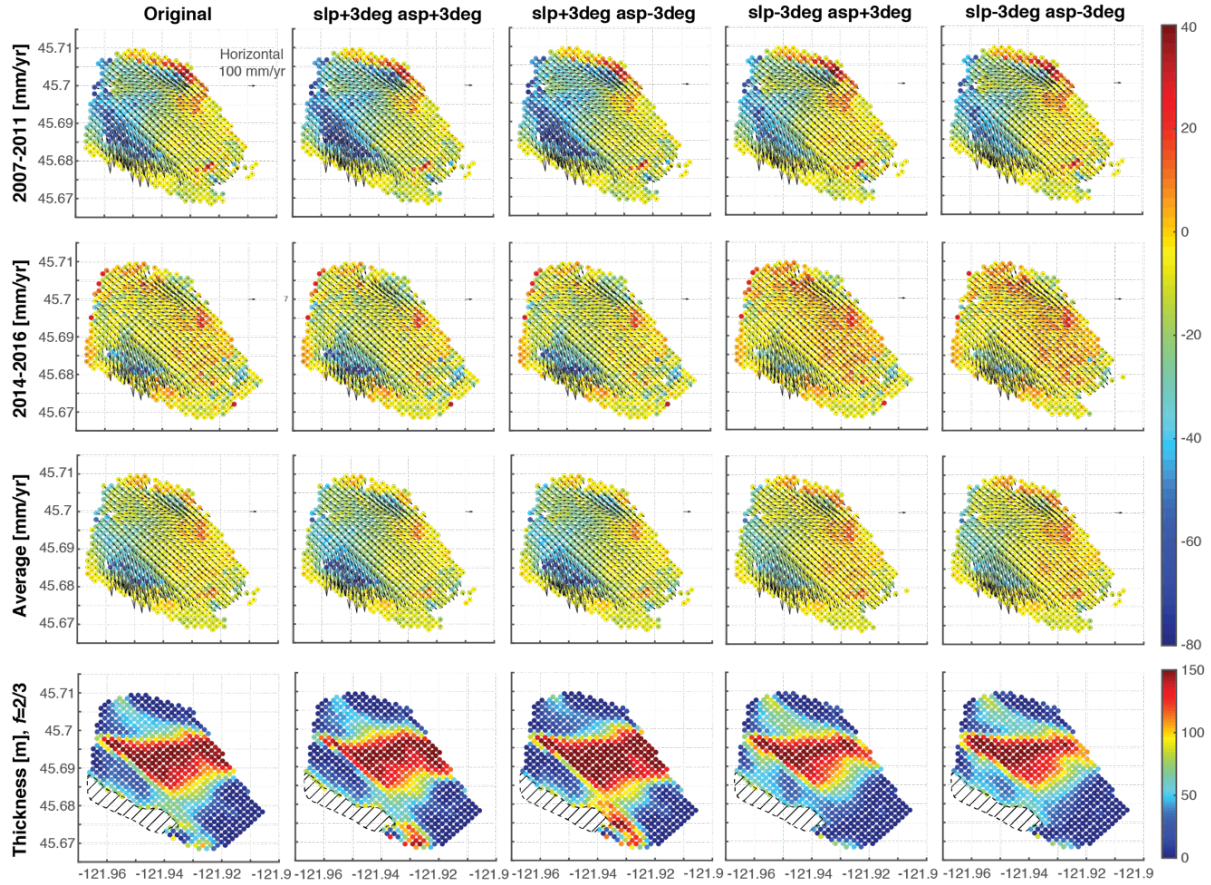


Figure 2.20 Biases in thickness inversion considering the uncertainty of $\pm 3^\circ$ in slope and aspect angles. First three rows show quasi-3D displacement maps during 2007-2011, 2014-2016, and the average of the mentioned time periods, respectively. The last row shows the consequent landslide thickness with the rheological parameter $f = 2/3$. Each column shows the estimates under the indicated angles of slope and aspect.

2.9.2 Plausible mechanism for precursory subsidence

Temporal variations in slide movement are also complex at the GPS station location in the middle of the landslide body. Under proper configuration between radar looking geometry and slope geometry, InSAR LOS observations may provide a unique perspective to better differentiate motions at different directions. Not only is the onset of seasonal downslope sliding detected using Sentinel-1A data, but a multi-week period of ground subsidence prior to the onset of sliding is also detected. Pronounced subsidence began early in the rainy season after ~ 140 mm of antecedent

rainfall accumulated. Once a total of ~270 mm of rain had accumulated, major downslope sliding began (Figure 2.15 and Table 2.2).

Table 2.2 Time points of the start of rainfall season and incipient landslide motion, and the cumulative precipitation in between.

		Rainfall season starts	Incipient motion	
			Slope-normal subsidence	Downslope sliding
2014-2015	Dates	09/24/2014	11/06/2014	11/30/2014
	Cumulative precip. [mm]	144.65	266.33	
2015-2016	Dates	08/29/2015	11/01/2015	11/25/2015
	Cumulative precip. [mm]	130.40	277.29	

The reason for the apparent pre-sliding surface subsidence is uncertain. It could be due to elastic loading in response to the accumulating mass of infiltrated rainfall [Fu et al., 2015; Hu et al., 2016], which from the InSAR data arguably could have started at the beginning of the fall rain in 2016. In loose soils subjected to shear stress, contractive soil behavior can occur during wetting or incipient motion [Iverson et al., 2000], and this can cause subsidence. Such contraction of saturated granular soil causes pore pressure at the failure surface to be rapidly elevated, and this if widespread within the mass, in turn, leads to abrupt decreases in shear strength that can trigger runaway acceleration [Iverson, 2005; Iverson et al., 2015]. But contractive soil behavior is unlikely in this case, because where subsidence was detected, the slip surface is deep and subject to high normal stress – 50 mm of slope-normal subsidence would reflect only an overall 0.051%-0.03% volume decrease in a landslide mass on the order of 100-150 m thick, which may be too little to significantly affect pore pressure at depth. In addition, the soil material is chemically altered and clay-rich, and slip has been occurring intermittently for decades. Given these constraints, shear has

almost certainly reduced porosity and strength at the slip surface to a residual state in which further contraction is highly unlikely.

The observed seasonal creep of this landslide argues for the opposite of contractive behavior—dilatant soil behavior. Dilatant strengthening during shear in already compact granular material leads to slow, limited shear in landslides [Moore and Iverson, 2002; Iverson, 2005]. If critical-state porosity is never reached during shear and if recompaction occurs during periods of no shear, episodes of slow shear can regularly recur, as observed at the Crescent Lake landslide. The observation that slip in this landslide occurs at its fastest rate initially, followed by a long period of deceleration (Figure 2.15), suggests that shear strength gradually increases during shear after the initial release. This mechanism would theoretically cause the ground surface to rise, not subside, so further investigation is needed to explain the direction and magnitude of observed ground-surface movement prior to the onset of downslope sliding.

This study has shown that the combined application of continuous GPS data having high temporal resolution with spaceborne InSAR data having high spatial resolution can reveal much more about the complexities of large landslide 3D shape and movement than is possible with geodetic measurements tied to only a few specific measurement sites. It shows the variations in landslide thickness and the configuration of the basal slip surface. It allows timing of the onset of sliding and the rate of sliding to be linked with threshold intensities and durations of rainfall. It allows spatial variations in sliding direction and rate to be assessed. And it also allows interannual differences in landslide behavior to be assessed in light of year-to-year variations in rainfall and other climatic factors.

ACKNOWLEDGMENTS

I thank Dr. Thomas C. Pierson, Dr. David L. George, and Dr. Rebecca Kramer from U.S. Geological Survey (USGS) Cascades Volcano Observatory for providing on-slide GPS data and their contributions to the study; Dr. Teng Wang from Nanyang Technological University (previously at the Radar Lab of Southern Methodist University) for his assistance during InSAR data processing and Dr. Jin-Woo Kim from our Radar Lab on ALOS-2 data acquisition; Dr. Roland Bürgmann from UC, Berkeley and the USGS internal reviewer Dr. Chuck Wicks, anonymous reviewers, and *Geophysical Research Letter* Editor Dr. Andrew V. Newman for their insightful comments. This research was financially supported by NASA Earth and Space Science Fellowship (NNX15AN10H), NASA Interdisciplinary Research (IDS) in Earth Science Program (80NSSC17K0022), and the Shuler-Foscue Endowment at Southern Methodist University. GPS data were obtained by the USGS Cascades Volcano Observatory, and are archived at <https://earthquake.usgs.gov/monitoring/gps/Helens/rdbf>; <https://doi.org/10.5066/F7NG4NRK>. Precipitation data were obtained from Western Regional Climate Center (WRCC) (<https://wrcc.dri.edu/cgi-bin/cliMAIN.pl?orbonn>). ALOS-1 and ALOS-2 raw data are copyrighted by the Japan Aerospace Exploration Agency (JAXA). Copernicus Sentinel Sentinel-1A data can be obtained from European Space Agency (ESA) or Alaska Satellite Facility (ASF).

REFERENCES

- Aryal, A., B. A. Brooks, and M. E. Reid (2015), Landslide subsurface slip geometry inferred from 3-D surface displacement fields, *Geophys. Res. Lett.*, *42*, 1411–1417, doi:10.1002/2014GL062688.
- Berardino, P., G. Fornaro, R. Lanari, and E. Sansosti (2002), A new algorithm for surface deformation monitoring based on small baseline differential SAR interferograms, *IEEE Transactions on Geoscience and Remote Sensing*, *40*, 2375–2383.
- Bishop, K. M. (1999), Determination of translational landslide slip surface depth using balanced cross sections, *Environ. Eng. Geosci.*, *5*(2), 147–156.
- Booth, A. M., M. P. Lamb, J.-P. Avouac, and C. Delacourt (2013), Landslide velocity, thickness, and rheology from remote sensing: La Clapière landslide, France, *Geophys. Res. Lett.*, *40*, 4299–4304, doi:10.1002/grl.50828.
- Braun, J., G. Major, D.O. West, and M. Bukovansky (1998), Geologic hazards evaluation boosts risk-management program for Western U.S. pipeline, *Oil and Gas J.*, *96*(45), 11/09/1998, 13 p.
- Calabro, M. D., D. A. Schmidt, and J. J. Roering (2010), An examination of seasonal deformation at the Portuguese Bend landslide, southern California, using radar interferometry, *J. Geophys. Res.*, *115*, F02020.
- Cannon, S. H., R. M. Kirkhamb, and M. Parise (2001), Wildfire-related debris-flow initiation processes, Storm King Mountain, Colorado, *Geomorphology*, *39*(3–4), 171–188.
- Chaussard, E., R. Bürgmann, M. Shirzaei, E. J. Fielding, and B. Baker (2014), Predictability of hydraulic head changes and characterization of aquifer system and fault properties from InSAR-derived ground deformation, *J. Geophys. Res. Solid Earth*, *119*, 6572–6590, doi:10.1002/2014JB011266.
- Chen, C. W., and H. A. Zebker (2001), Two-dimensional phase unwrapping with use of statistical models for cost functions in nonlinear optimization, *Journal of the Optical Society of America A*, *18*(2), 338–351.

- Cossart, E., D. Mercier, A. Decaulne, T. Feuillet, H. P. Jónsson, and P. Sæmundsson (2014), Impacts of post-glacial rebound on landslides spatial distribution at a regional scale in northern Iceland (Skagafjörður), *Earth Surf. Process. Landforms*, 39, 336–350.
- CVX Research, Inc. (2013), CVX: Matlab software for disciplined convex programming, version 2.0 beta., edited.
- Delbridge, B. G., R. Bürgmann, E. Fielding, S. Hensley, and W. H. Schulz (2016), Three-dimensional surface deformation derived from airborne interferometric UAVSAR: Application to the Slumgullion Landslide, *J. Geophys. Res. Solid Earth*, 121, doi:10.1002/2015JB012559.
- DNR (2005), LiDAR DEM of Skamania County. Washington Department of Natural Resources, Olympia Washington, www.dnr.wa.gov.
- Dzurisin, D., M. Lisowski, and C. W. Wicks Jr. (2017), Semipermanent GPS (SPGPS) as a volcano monitoring tool: Rationale, method, and applications, *J. Volcanol. Geotherm. Res.*, 344, 40–51, doi:10.1016/j.jvolgeores.2017.03.007.
- Farinotti, D., M. Huss, A. Bauder, M. Funk, and M. Truffer (2009), A method to estimate the ice volume and ice-thickness distribution of alpine glaciers, *J. Glaciol.*, 55(191), 422–430.
- Ferretti, A., C. Prati, and F. Rocca (2001), Permanent scatterers in SAR interferometry, *IEEE Trans. Geosci. Remote Sens.*, 39(1), 8–20.
- Fu, Y., D. F. Argus, and F. W. Landerer (2015), GPS as an independent measurement to estimate terrestrial water storage variations in Washington and Oregon, *J. Geophys. Res. Solid Earth*, 120, 552–566, doi:10.1002/2014JB011415.
- George, D., and R. M. Iverson (2014), A depth-averaged debris-flow model that includes the effects of evolving dilatancy II: Numerical predictions and experimental tests, *Proc. R. Soc. A*, 470:20130820.
- Gili, J. A., J. Corominas, and J. Rius (2000), Using Global Positioning System techniques in landslide monitoring, *Engineering Geology*, 55(3), 167–192.
- Handwerger, A. L., J. J. Roering, D. A. Schmidt, and A. W. Rempel (2015), Kinematics of earthflows in the Northern California Coast Ranges using satellite interferometry, *Geomorphology*, 246, 321–333.
- Hanssen, R. F. (2001), *Radar Interferometry: Data Interpretation and Error Analysis*, Norwell, MA, USA: Kluwer Academic Publishers.

- Highland, L. M., and P. Bobrowsky (2008), The landslide handbook—a guide to understanding landslides, *U.S. Geological Survey Circular 1325*, 129.
- Hilley, G. E., R. Bürgmann, A. Ferretti, F. Novali, F. Rocca (2004), Dynamics of slow-moving landslides from permanent scatterer analysis, *Science*, 304(5679), 1952–1955, <http://dx.doi.org/10.1126/science.1098821>.
- Hooper, A. (2010), A statistical-cost approach to unwrapping the phase of InSAR time series, *European Space Agency Special Publication, ESA SP-677*.
- Hooper, A., H. Zebker, B. Segall, and B. Kampes (2004), A new method for measuring deformation on volcanoes and other natural terrains using InSAR persistent scatterers, *Geophys. Res. Lett.*, 31, L23611.
- Hu, X., T. Wang, and M. Liao (2014), Measuring coseismic displacements with point-like targets offset tracking, *IEEE Geosci. Remote Sens. Lett.*, 11(1), 283–287.
- Hu, X., Z. Lu, T. C. Pierson, R. Kramer, and D. L. George (2018), Combining InSAR and GPS to determine transient movement and thickness of a seasonally active low-gradient translational landslide, *Geophys. Res. Lett.*, 45, 1453–1462.
- Hu, X., T. Wang, T. C. Pierson, Z. Lu, J. Kim, and T. H. Cecere (2016), Detecting seasonal landslide movement within the Cascade landslide complex (Washington) using time-series SAR imagery, *Remote Sens. Environ.*, 187, 49–61.
- Huang, M.-H., E. J. Fielding, C. Liang, P. Milillo, D. Bekaert, D. Dreger, and J. Salzer (2017), Coseismic deformation and triggered landslides of the 2016 Mw 6.2 Amatrice earthquake in Italy, *Geophys. Res. Lett.*, 44, 1266–1274, doi:10.1002/2016GL071687.
- Iverson, R. M. (2000), Landslide triggering by rain infiltration, *Water Resources Res.*, 36(7), pp. 1897–1910.
- Iverson, R. M. (2005), Regulation of landslide motion by dilatancy and pore pressure feedback, *J. Geophys. Res.*, 110, F02015, doi:10.1029/2004JF000268.
- Iverson, R. M., George, D. L., Allstadt, K., Reid, M. E., Collins, B. D., Vallance, J. W., Schilling, S. P., Godt, J. W., Cannon, C. M., Magirl, C. S., Baum, R. L., Coe, J. A., Schulz, W. H., and Bower, J. B. (2015), Landslide mobility and hazards: implications of the 2014 Oso disaster, *Earth Planet. Sci. Lett.*, 412, 197–208.
- Iverson, R. M., M. E. Reid, N. R. Iverson, R. G. LaHusen, M. Logan, J. E. Mann, and D. L. Brien (2000), Acute Sensitivity of Landslide Rates to Initial Soil Porosity, *Science*, 290(5491), 513–516, doi:10.1126/science.290.5491.513.

- Iverson, R. M., M. E. Reid, and R. G. LaHusen (1997), Debris-flow mobilization from landslides, *Annu. Rev. Earth Planet. Sci.*, 25(1), 85-138, doi:10.1146/annurev.earth.25.1.85.
- Kargel, J. S., Leonard, G. J., Shugar, D. H., Haritashya, U. K., Bevington, A., et al. (2016). Geomorphic and geologic controls of geohazards induced by Nepal's 2015 Gorkha earthquake, *Science*, 351(6269), doi:10.1126/science.aac8353.
- Kim, J. W., Lu, Z., Qu, F., and Hu, X. (2015), Pre-2014 mudslides at Oso revealed by InSAR and multi-source DEM analysis, *Geomatics, Natural Hazards and Risk*, 6(3), 184-194.
- Korosec, M. A. (1987), Geologic map of the Hood River quadrangle, Washington and Oregon – 1987, *Washington Division of Geology and Earth Resources Open File Report 87-6*, scale 1:100,000.
- Lacroix, P., H. Perfettini, E. Taïpe, and B. Guillier (2014), Coseismic and postseismic motion of a landslide: Observations, modeling, and analogy with tectonic faults, *Geophys. Res. Lett.*, 41, 6676–6680.
- Lawrence, D. B., and E. G. Lawrence (1958), The Bridge of the Gods Legend, Its Origin, History, and Dating, *Mazama*, 40(13), 33-41.
- Mackey, B. H., and J. J. Roering (2011), Sediment yield, spatial characteristics, and the long-term evolution of active earthflows determined from airborne LiDAR and historical aerial photographs, Eel River, California, *Geol. Soc. Am. Bull.*, 123, 1560–1576.
- Malamud, B., Turcotte, D., Guzzetti, F., and Reichenbach, P. (2004), Landslides, earthquakes, and erosion, *Earth Planet. Sci. Lett.*, 229, doi:10.1016/j.epsl.2004.10.018.
- Michel, R., J. P. Avouac, and J. Taboury (1999), Measuring ground displacements from SAR amplitude images: Application to the Landers earthquake, *Geophys. Res. Lett.*, 26(7), 875–878.
- Morlighem, M., E. Rignot, H. Seroussi, E. Larour, H. Ben Dhia, and D. Aubry (2011), A mass conservation approach for mapping glacier ice thickness, *Geophys. Res. Lett.*, 38, L19503, doi:10.1029/2011GL048659.
- Moore, P. L., and N. R. Iverson (2002), Slow episodic shear of granular materials regulated by dilatant strengthening, *Geology*, 30 (9), 843–846.
- Nikolaeva, E., T. Walter, M. Shirzaei, and J. Zschau (2014), Landslide observation and volume estimation in central Georgia based on L-band InSAR, *Nat. Hazards Earth Syst. Sci.*, 14(3), 675–688.

- O'Connor, J. E. (2004), The evolving landscape of the Columbia River Gorge–Lewis and Clark and cataclysms on the Columbia, *Oregon Historical Quarterly*, 105(3), 390–421.
- O'Connor, J. E., and S. F. Burns (2009), Cataclysms and controversy–Aspects of the geomorphology of the Columbia River Gorge, *Geological Society of America Field Guides* 2009, 15, 237-251.
- Palmer, L. (1977), Large landslides of the Columbia River Gorge, Oregon and Washington, *Reviews in Engineering Geology*, 3, 69-84.
- Petley, D. (2012), Global patterns of loss of life from landslides, *Geology*, 40(10), 927–930, doi:10.1130/G33217.1.
- Petley, D. (2016), Landslides from the Kumamoto earthquake in Japan, Online access: <http://blogs.agu.org/landslideblog/2016/04/18/kumamoto-earthquake-1/> Post on April 18, 2016, Last access on June 18, 2017
- Pierson, T. C., and Z. Lu (2009), InSAR detection of renewed movement of a large ancient landslide in the Columbia River Gorge, Washington, *Geological Society of America Abstract with Programs*, 2009 Portland Annual Meeting, 41(7), 497.
- Pierson, T. C., R. C. Evarts, and J. A. Bard (2016), Landslides in the western Columbia Gorge, Skamania County, Washington, *U.S. Geological Survey Scientific Investigations Map* 3358.
- Priest, G. R., W. H. Schulz, W. L. Ellis, J. A. Allan, A. R. Niem, and W. A. Niem (2011), Landslide stability: role of rainfall-induced, laterally propagating, pore-pressure waves, *Environmental and Engineering Geoscience*, 17(4), 315–335.
- Randall, J. R. (2012), Characterization of the Red Bluff Landslide, Greater Cascade landslide complex, Columbia River Gorge, Washington, Master thesis, Portland State University.
- Rogers, J. D., and J. Chung (2016), Applying Terzaghi's method of slope characterization to the recognition of Holocene land slippage, *Geomorphology*, 265, 24–44.
- Saar, M. O., and Manga, M. (2003), Seismicity induced by seasonal groundwater recharge at Mt. Hood, Oregon, *Earth Planet. Sci. Lett.*, 214, 605-618.
- Samsonov, S. (2010), Topographic Correction for ALOS-1 PALSAR Interferometry, *IEEE Trans. Geosci. Remote Sens.*, 48(7), 3020-3027.
- Scambos, T. A., M. J. Dutkiewicz, J. C. Wilson, and R. A. Bindshadler (1992), Application of image cross-correlation to the measurement of glacier velocity using satellite image data, *Remote Sens. Environ.*, 42(3), 177–186.

- Schulz, W. H., J. W. Kean, and G. Wang (2009), Landslide movement in southwest Colorado triggered by atmospheric tides, *Nat. Geosci.*, 2, 863–866, doi:10.1038/NGEO659.
- Simons, M., and P. Rosen (2015), *A Interferometric Synthetic Aperture Radar Geodesy*, In: Gerald Schubert (editor-in-chief) *Treatise on Geophysics*, 2nd edition, Vol 3. Oxford: Elsevier, 339–385.
- Tong, X., and D. A. Schmidt (2016), Active movement of the Cascade landslide complex in Washington from a coherence-based InSAR time series method, *Remote Sens. Environ.*, 186, 405–415.
- Walsh, T. J., M. A. Korosec, W. M. Phillips, R. L. Logan, and H. W. Schasse (1987), *Geologic map of Washington—Southwest quadrant. Washington Division of Geology and Earth Resources, Geologic Map GM-34, scale 1:250,000.*
- Wang, T., S. Wei, and S. Jónsson (2015), Coseismic displacements from SAR image offsets between different satellite sensors: Application to the 2001 Bhuj (India) earthquake, *Geophys. Res. Lett.*, 42(17), 7022–7030.
- Wang, T., and S. Jónsson (2015), Improved SAR Amplitude Image Offset Measurements for Deriving Three-Dimensional Coseismic Displacements, *IEEE J. Sel. Top. Appl. Earth Obs. Remote Sens.*, 18, doi:10.1109/JSTARS.2014.2387865.
- Waters, A. C. (1973), The Columbia River Gorge - Basalt stratigraphy, ancient lava dams, and landslide dams. In Beaulieu, J. D., *Geologic field trips in northern Oregon and southern Washington, Oregon Department of Geology and Mineral Industries Bulletin*, 77, 133–162.
- Wise, W. S. (1961), The Geology of the Wind River Area, Washington, and the Stability Relations of Celadonite, PhD dissertation, John Hopkins University, 191–195.
- Zhao, C., Z. Lu, Q. Zhang, J. Fuente (2012), Large-area landslide detection and monitoring with ALOS/PALSAR imagery data over Northern California and Southern Oregon, USA, *Remote Sens. Environ.*, 124, 348–359, doi:10.1016/j.rse.2012.05.025.

CHAPTER 3

CHARACTERIZATION OF HYDRODYNAMICS OF SALT LAKE VALLEY, UTAH

Hu, X., Z. Lu, and T. Wang, 2018, Characterization of hydrogeological properties in Salt Lake Valley, Utah using InSAR, *J. Geophys. Res.: Earth Surf.* (accepted)

3.1 Introduction

Aquifer systems play an important role as a stable water source, by storing rainfall and snowmelt underground during the recharge process and supplying rivers and/or lakes with water during the discharge process. This is certainly true in the Salt Lake Valley of Utah, where humans rely on groundwater for domestic and municipal uses [Wallace and Lowe, 2009]. While extreme changes in climate (e.g. decadal drought or sustained intense precipitation) can disrupt the normal seasonal groundwater balance held in aquifer systems, agricultural and industrial development, and other human activities (e.g., over-pumping and/or injection) are the primary threat to their stability. Changes in aquifer reservoir volumes may manifest as surface deformation, which can be observed using InSAR techniques.

Water recharge and discharge modulates subsurface pore pressure and the effective stress that is usually accompanied by deforming an aquifer skeleton. For example, groundwater removal through pumping has been widely performed for domestic, municipal, industrial, and irrigational uses, which may lead to land subsidence at rates of tens of cm/year associated with the drastic decline of water level [Bell et al., 2002]. In addition to removing groundwater from aquifer

systems, artificial recharge, or pumping into an aquifer, is sometimes implemented as a technique to manage the long-term removal of water and/or to store water in anticipation of upcoming demand, which may exert regional uplift [Amelung et al., 1999; Lu and Danskin, 2001; Schmidt and Burgmann, 2003; Chaussard et al., 2014]. The resulting deformation can generally be classified as either elastic (recoverable) strain that is typically associated with cyclic compression and dilation of the aquifer skeleton, or inelastic strain that is often associated with irreversible subsidence following long-term discharge when the effective stress is larger than the preconsolidation stress [e.g., Casagrande, 1932; 1936; Galloway et al., 1999; Amelung et al., 1999; Miller and Shirzaei, 2015; Miller et al., 2017].

Spaceborne multi-temporal InSAR observations represent a useful method to quantify ground deformation due to water level changes with mm/yr accuracy. For example, vertical deformation and associated hydrological properties have been studied for cities built in the desert, such as Las Vegas [Amelung et al., 1999], Tucson [Kim et al., 2015; Miller et al., 2017] and Phoenix [Miller and Shirzaei, 2015], for valleys with rapid urban and industrial development, such as Santa Clara Valley, California [Schmidt and Burgmann, 2003], and in valleys with heavy agricultural production, such as San Luis Valley, Colorado [Reeves et al., 2014; and Chen et al., 2016]. In this study, I combine InSAR data with water level data to derive hydrogeological properties in Salt Lake Valley, Utah. Based on the spatio-temporal correlation between vertical ground deformation and the water discharge and recharge processes, I discuss both natural and anthropogenic triggers to the observed deformation in the valley.

3.2 Study area

Salt Lake Valley, Utah, which includes the state capital Salt Lake City, is the commercial, industrial, and financial center of the State of Utah. One-third of the State's population (~3 million)

is concentrated in the valley. The basin is bounded on the west and east by the generally parallel, north-south trending mountain ranges, Oquirrh Mountains and Wasatch Range, respectively (Figure 3.1a). To the south, the west-east trending Traverse Mountains bound the valley. The 70-km long Jordan River traverses the center of Salt Lake Valley, connecting two remnants of prehistoric Lake Bonneville (30,000-14,000 yr BP) – the Great Salt Lake and Utah Lake. The well-known Wasatch fault zone (WFZ) is situated along the mountain front of the Wasatch Range, and the West Valley fault zone (WVFZ) is located within the valley. The basin-fill deposits (boundary outlined by the white line in Figure 3.1a) consist of the surficial and near-surficial unconsolidated Quaternary deposits by Lake Bonneville, and the underlying generally unconsolidated to semi-consolidated Tertiary deposits [Arnow et al., 1970; Thiros et al., 2010]. The main basin-fill deposits are vertically stratified into both shallow aquifers and deeper aquifers, with the latter marked by discontinuous layers of fine-grained deposits that inhibit the downward movement of groundwater.

3.2.1 Tectonic settings

The 390-km long WFZ extends from Malad City, Idaho, to Fayette, Utah and shadows the western flank of the Wasatch Range. WVFZ has similar orientation but locates in the central axis of the basin. The East Great Salt Lake fault zone is submerged beneath the Great Salt Lake (Figure 3.2). The fault segments underling Salt Lake City are believed to produce large earthquakes (M 7.0+) every 1,300 to 1,500 years. The last large earthquake occurred about 1,400 years ago, which implies that another large event is likely [EERI, 2015]. A recent report by U.S. Geological Survey (USGS) [2016] suggests a 43% likelihood of at least one large earthquake of magnitude 6.75 or greater, and 93% likelihood of a moderate quake of magnitude 5 or greater in the next 50 years in the Salt Lake Valley—home to approximately half of Utah’s ~3 million residents.

3.2.2 Hydrogeologic settings

Within the boundary of basin-fill sediments, the aquifer systems can be classified into three distinct areas: primary recharge area, secondary recharge area, and the discharge area (Figure 3.1a). The primary recharge area is in the uplands along the mountain fronts where there is an absence of confining fine-grained deposits and a downward hydrologic gradient flow (Figure 3.1b). The secondary recharge area, usually at a lower elevation from the primary recharge area, such as a mountain bench, contains both unconfined and confining layers in the subsurface. The hydraulic gradient is again downward and groundwater flows into deeper layers and/or towards the discharge area. Annual groundwater recharge to the aquifer systems is about 0.4 km^3 [Lambert 1995; Thiros et al., 2010]. Major sources of recharge include subsurface inflow from mountain streams (45%) and precipitation infiltration (21%) [Thiros et al., 2010]. In the discharge area, the hydraulic gradient is reversed, enabling groundwater to flow up into a confined area or to exit to the surface (Figure 3.1b). Naturally occurring discharge to the surface occurs under several circumstances: where the water table intersects the surface, discharge around the unconfined aquifer occurs into streams, canals, the Jordan River; where the surface elevation is low in the vicinity of the Great Salt Lake, discharge around the confined aquifer occurs at the northern part of the valley; finally, some water is lost through evapotranspiration. When there is sufficient natural pressure, water reaches the surface at artesian wells. Anthropogenic withdrawal of water from the systems may also be referred to as groundwater discharge, but a water well could be located in any of the three areas (primary recharge, secondary recharge, or discharge area) under the right conditions. The main components of groundwater discharge include seepage into streams (43%) and well withdrawal (33%) [Thiros et al., 2010].

The confined aquifer consists primarily of Quaternary deposits (0 to over 600 m) of clay, silt, sand, and gravel. Above the confined aquifer is a confining layer composed of individual Quaternary deposits of fine-grained clay and/or silt that creates an impermeable layer (Figure 3.1b). The confining layer is between 12 and 30 m thick with its top 15 to 46 m below the land surface. There might be a shallow unconfined aquifer overlying the confining layer, and it is sometimes hard to differentiate between them. The shallow unconfined aquifer is primarily composed of fine-grained sediments, and it has a maximum thickness of 15 m [Snyder and Lowe, 1998; Wallace and Lowe, 2009]. This study focuses on the vertical ground deformation and the related hydrodynamics of the confined and semi-confined aquifers, mainly over the water discharge area and secondary recharge area.

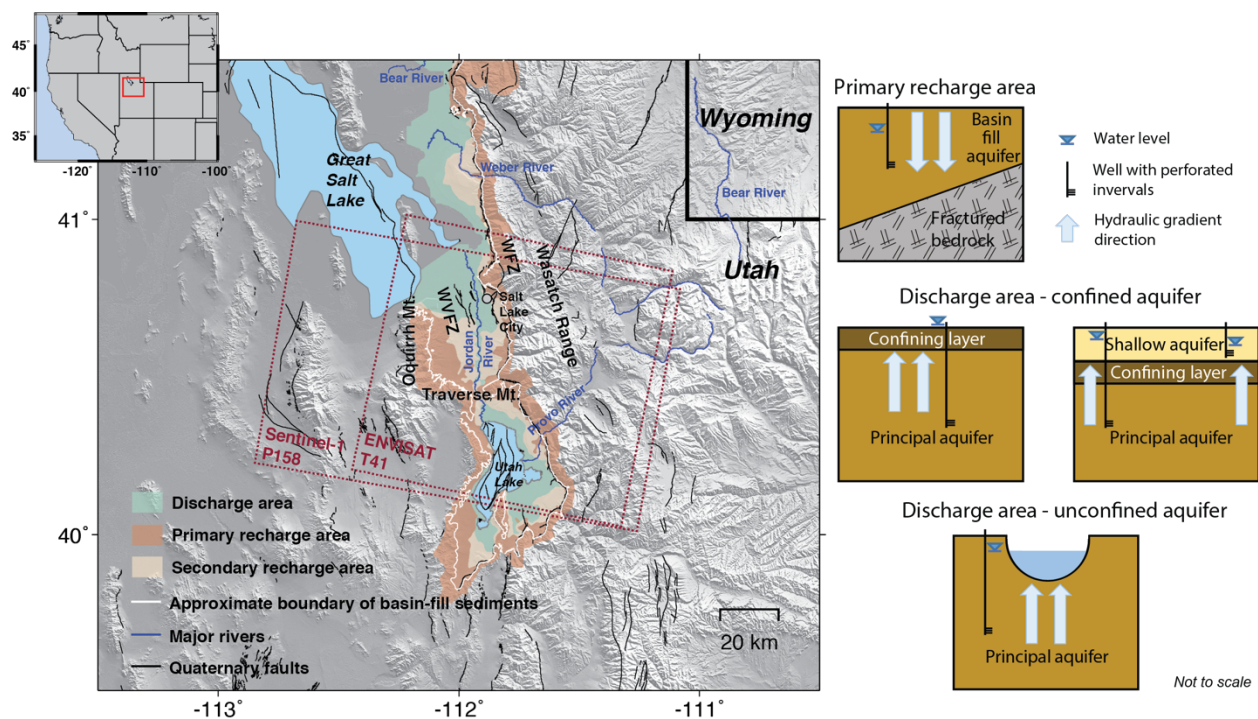


Figure 3.1 Locations and hydrogeologic architectures of groundwater discharge, primary recharge and secondary recharge areas in Salt Lake Valley, Utah. White lines delineate the boundary of basin-fill sediments, blue lines show the major river channels, and black lines show the known faults. The coverage of descending SAR tracks ENVISAT Track 41 (T41) and Sentinel-1A Path 158 (P158; cropped) are marked with red dotted rectangles. Sketch of hydrogeologic architectures on the right are modified from Wallace and Lowe (2009) and Snyder and Lowe (1998).

3.3 Methodology

3.3.1 Multi-temporal InSAR analysis

Forty ENVISAT ASAR strip mode data (2004-2010) and twenty Sentinel-1A Interferometric wide swath mode data (2015-2016) were used to derive the deformation field over the study area based on multi-temporal InSAR analysis [e.g., Ferretti et al., 2001; Berardino et al., 2002; Hooper 2008; Hu et al, 2016; Shirzaei et al. 2017]. ENVISAT's heading and incidence angles were -167.83° and 22.78° , and Sentinel-1A's heading and incidence angles were -166.38° and 41.97° . I processed the ENVISAT data using GAMMA software. I processed the Sentinel-1A data burst by burst and then merged them into one interferogram. The phase discontinuity was corrected from burst-overlap interferometry [Jiang et al., 2017]. A set of 126 ENVISAT interferograms with perpendicular baselines less than 300 m and temporal intervals fewer than 500 days, and 82 Sentinel-1A interferograms with perpendicular baselines less than 250 m and temporal intervals fewer than 180 days were chosen for time-series analysis (Figure 3.2). The topographic phase component of each interferogram was simulated by 2000 SRTM DEM.

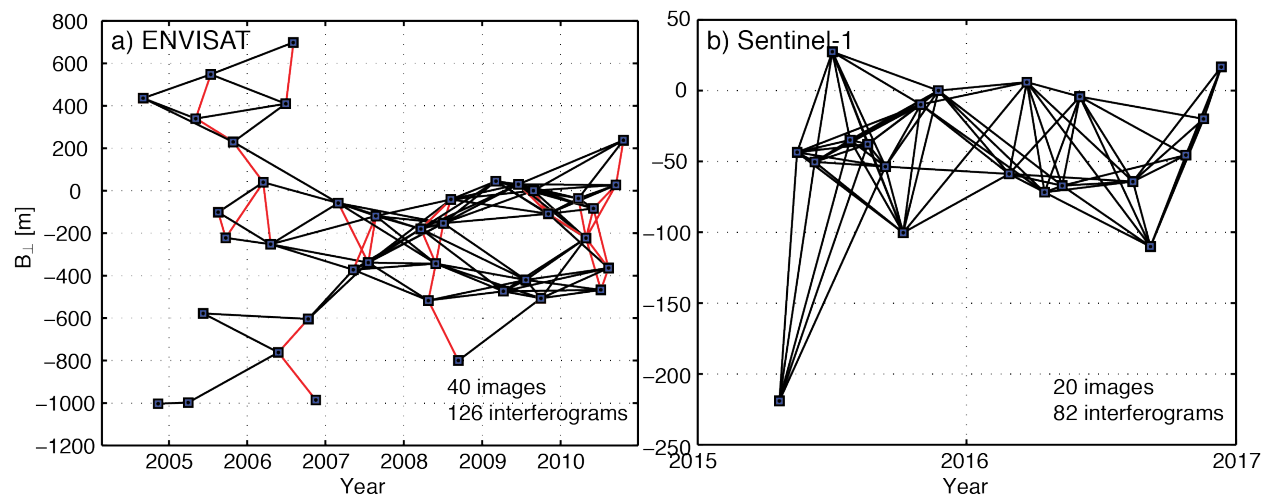


Figure 3.2 Image graph of the interferometric pairs: ENVISAT (a) and Sentinel-1 (b) datasets. Squares represent satellite images and connecting lines show the interferograms used to retrieve the time-series deformation, in which the red ones in (a) indicate the relatively large-baseline and short-interval interferograms used to estimate topographic error during ENVISAT data processing.

The urbanized basin terrain from Salt Lake City to Bluffdale maintains good InSAR coherence. However, it is mostly isolated by the mountainous areas to the west, east and south sides, as well as the wetland area in the vicinity to the Great Salt Lake to the east side, where the radar phase values are poorly correlated in time or incoherent in space (Figure 3.3). It results in very narrow channels (bounded by mountains) with decent coherence to connect the basin terrain to other urban areas to the north (e.g., North Salt Lake) and the south (e.g., Lehi). This spatial configuration of surface features may lead to phase jumps at the north and south mouths when using a general phase unwrapping routine. To address this issue, pixels with DA (see section 2.4.1.1) less than 0.35 and an averaged coherence larger than 0.5 were chosen as coherent targets (CT) for ENVISAT data. The corresponding thresholds were 0.15 and 0.7 for Sentinel-1A data. The window used to estimate the spatial coherence is 15 by 5 and 6 by 23 pixels for ENVISAT and Sentinel-1A data, respectively. Unwrapping was then performed exclusively on those CT points [Ferretti et al., 2001; Hooper, 2010; Hu et al., 2016]. Finally, the deformation signals were resolved by culling out the DEM errors, atmospheric phase screen and orbital artifacts inherent in each interferogram based on their spatial and temporal signatures [Hu et al., 2016].

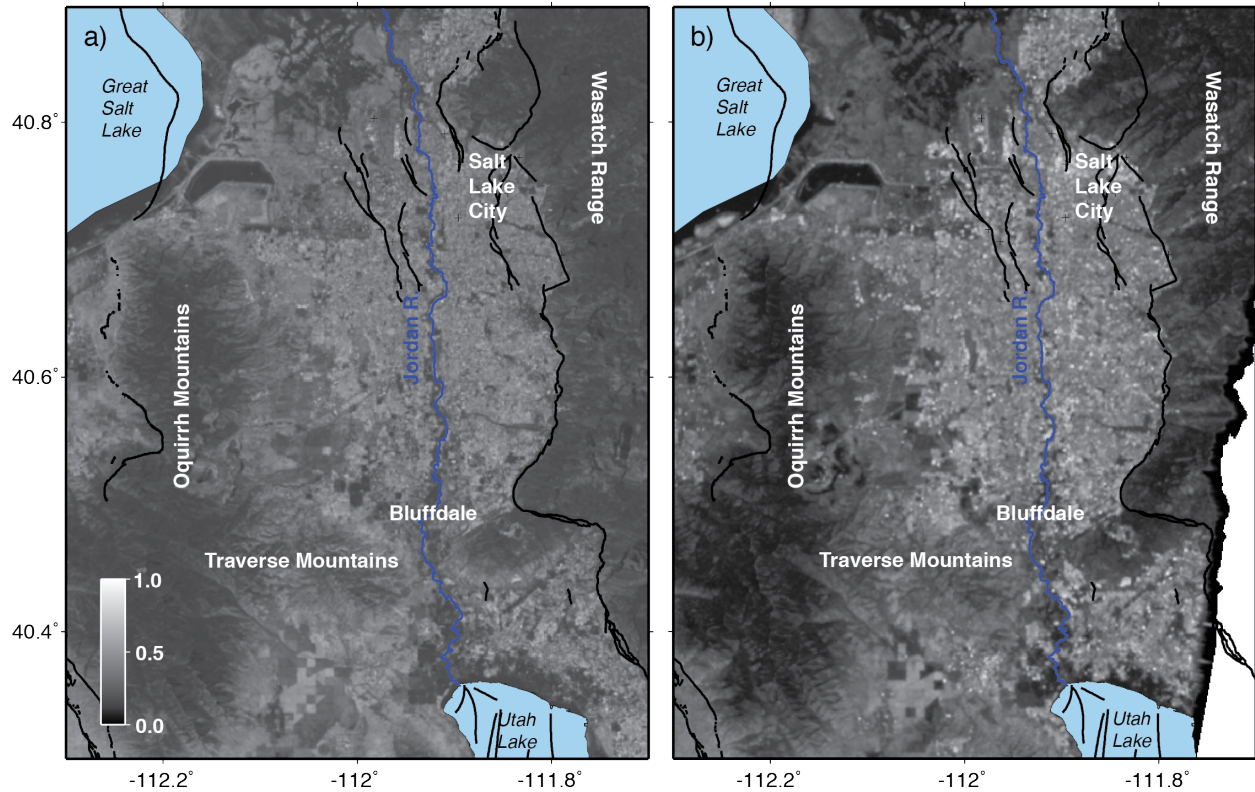


Figure 3.3 Mean coherence map of (a) ENVISAT and (b) Sentinel-1A. Brighter areas represent a higher coherence (maximum = 1; minimum = 0), suitable for time-series InSAR analysis. Both ENVISAT and Sentinel-1A datasets show coherence in a relatively narrow north-south channel, bounded by the mountain ranges.

The inconsistency of DEM sources and/or DEM errors can introduce phase artifacts, which may be expressed as spurious deformation signals [e.g., Hu et al., 2016]. This is particularly the case for the ENVISAT dataset due to its varied baseline configurations. Therefore, ENVISAT interferograms (red connecting lines in Figure 3.2a) with relatively larger perpendicular baselines (>100 m) and smaller time spans (<180 days) were selected to isolate the DEM errors [e.g., Massonnet and Feigl, 1998; Lu and Dzurisin, 2014], assuming that the phase is dominated by the error in DEM rather than ground deformation. Interestingly, the map of DEM errors highlights a nearly 1-km² area (40°45'52"N, 111°53'20"W) with an error of more than 15-m over downtown Salt Lake City; this observation is consistent with the anomaly in the differential DEM map between 2000 SRTM DEM and 2006 LiDAR DEM (Figure 3.4). Historic aerial photographs show

no visible change for the high-rise buildings clustered in downtown Salt Lake City. The agreement between these two independent estimations suggests that C-band SRTM radar data may contain height errors probably due to geometric artifacts and/or unwrapping errors associated with the urban landscape.

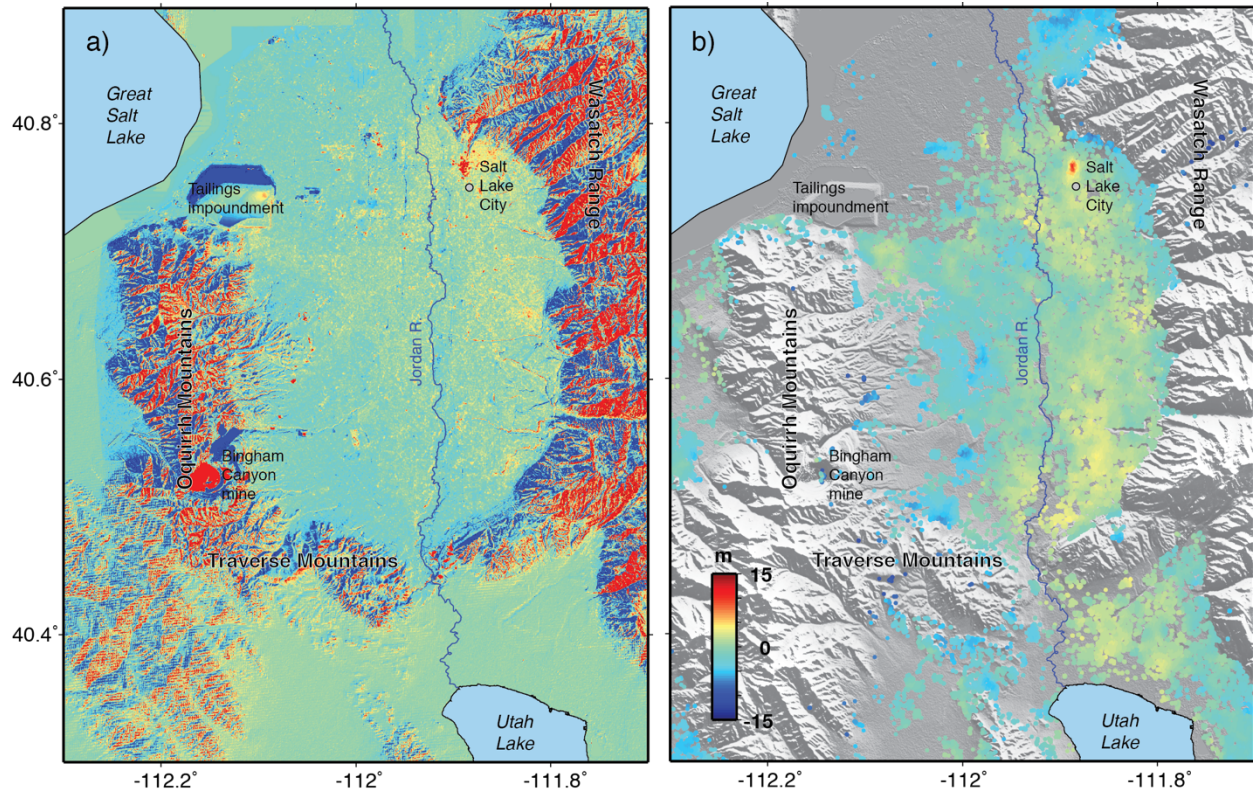


Figure 3.4 Topographic error analysis. (a) Differential DEM of 2000 SRTM DEM and 2006 LiDAR DEM (subtract LiDAR DEM from SRTM DEM). (b) Topographic errors estimated by ENVISAT dataset.

I assume that the derived deformation in the basin is mainly vertical, because the basin accommodates classic normal faults with steep dip angles $\sim 60\text{--}86^\circ\text{W}$ [Black et al., 1996]. In addition, the burst-overlapping interferometry of Sentinel-1A data (~ 2 cm accuracy) [Jiang et al., 2017], which is sensitive to deformation along the azimuth direction, also suggests no detectable horizontal deformation in the approximate north-south direction (Figure 3.5). All deformation

mentioned below, without specification, has already been projected into the vertical direction from the radar line-of-sight direction.

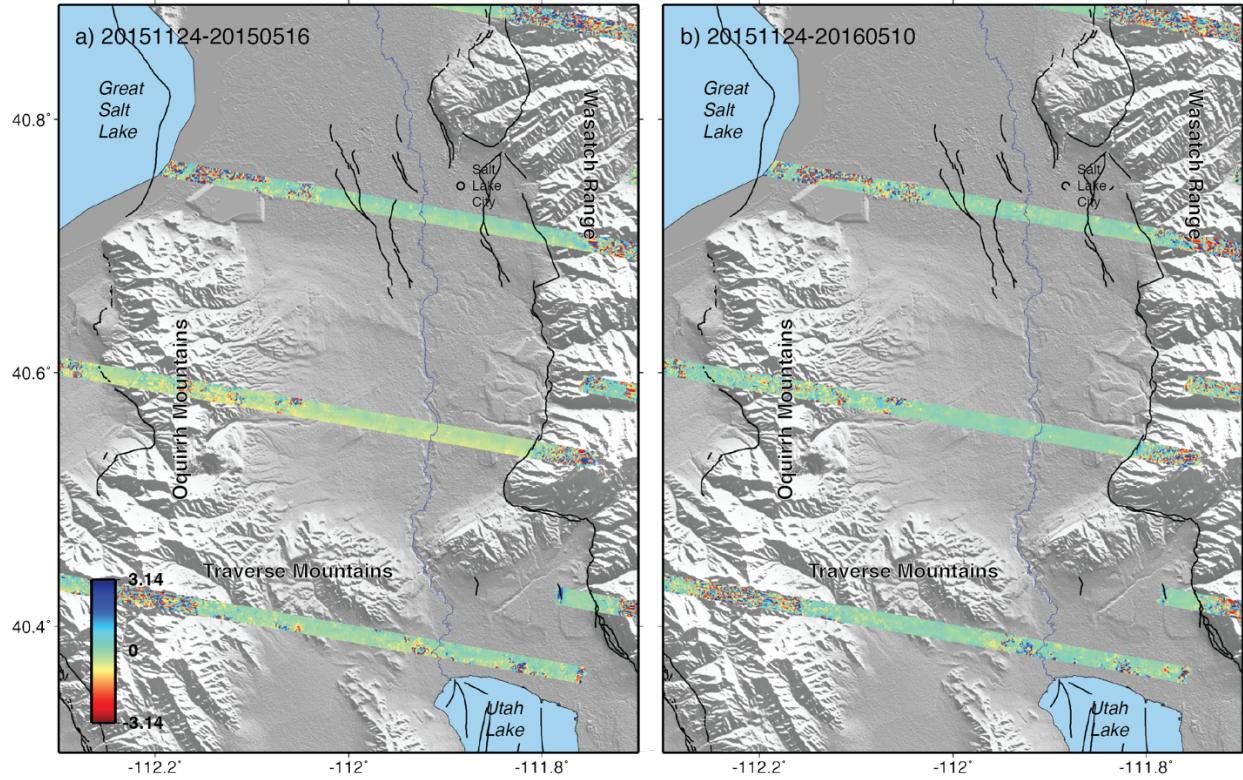


Figure 3.5 Azimuth interferometry over Sentinel-1A overlapping bursts: 20151124-20150516 (a) and 20151124-20160510 (b).

3.3.2 Separation of long-term and seasonal deformation signatures

The long-term deformation velocity of an aquifer is often related to prolonged hydraulic head changes, in contrast to the seasonal deformation considered a short-term response to groundwater redistribution. To characterize the time-series deformation, I need to separate out the long-term deformation from seasonal fluctuations. I first fit the non-linear component of time-series deformation at each CT using harmonic series to roughly simulate the periodicity of deformation behavior. The merits of this method are that I can obtain the seasonal deformation signal agreed with given apparent frequency. On the basis of the observations that the processes of water

discharge (Figure 3.7) and recharge (Figure 3.8) take a period of one year, and that water levels are also annual (Figure 3.11), I consider the pixel with deformation seasonality feature of deformation when the derived deformation waveform contains 10 to 14 peaks or troughs during the six-year period from 2004 to 2010; otherwise, the pixel is flagged without seasonality. The more sinusoidal functions used, the better fit with the observation. However, here the purpose is to extract the apparent seasonality. If I use many independent sinusoidal functions, the fit results will capture the high-frequency wiggles in the time series, and introduce unexpected peaks or troughs. In the study area, using three independent sinusoidal functions best simulates the apparent seasonality. For pixels with the seasonality feature of deformation, the remainder after subtracting the harmonic series from the original time series is considered to be the long-term signature. Using a sinusoidal function of time to perform the InSAR time-series analysis is not new [e.g., Ferretti et al., 2000; Agram et al., 2013; Riel et al., 2014; Agram and Simons, 2015; Reinisch et al., 2016; Fattahi et al., 2017]. However, the method has two advantages: first, not all targets deform with seasonality so I testify if the time-series deformation contains the seasonality or not rather than force the deformation pattern of all targets exclusively using sinusoidal wave; and second, I allow year-by-year variations in amplitude and frequency using the superposition of three independent sinusoidal functions, but constrain the waveform within the desired apparent frequency.

3.3.3 Estimation of aquifer properties from surface deformation and groundwater levels

3.3.3.1 Decay coefficient

The groundwater system in Salt Lake Valley's basin-fill deposits includes a shallow aquifer that is separated from a deeper aquifer by discontinuous layers or lenses of fine-grained materials. The existence and different thickness of the embedded clay lenses with low hydraulic conductivity may result in various time scales of delay for the equilibration to hydraulic head changes. The

delayed response can be characterized by modeling the long-term vertical deformation as an exponential function of time [Chaussard et al., 2014; Miller and Shirzaei, 2015; Miller et al., 2017]:

$$d_{long-term}(t) = M(e^{kt} - 1) \quad (3.1)$$

where $d_{long-term}(t)$ is long-term vertical deformation at time t , M is the magnitude coefficient ($M > 0$ when net subsidence and $M < 0$ when net uplift), and k is the decay coefficient (between -1 and 0), which is related to the compressibility and hydraulic conductivity of the aquifer-system skeleton and is used to simulate the decelerated deforming process. A smaller decay coefficient k (closer to -1) leads to a faster equilibration (leveling off), suggesting a faster response to a given hydraulic head change in a long-term view.

The decay coefficient k , which is used to describe the decelerated deforming process, was estimated from six-years of deformation measurements of ENVISAT data (2004-2010) using a least-squares inversion technique. Although the Sentinel-1A dataset provides deformation measurements between 2015 and 2016, the limited observation interval was too short to constrain the decay coefficient. After removing the seasonal component (if any), the remaining long-term deformation component was used to derive the decay coefficient at each CT based on Equation (3.1).

3.3.3.2 Storage properties and bulk aquifer compressibility

Storage properties are also important hydrological parameters for water management. The specific storage coefficient S_s for a confined aquifer is the amount of water drained from the compressed aquifer systems with per unit decline in hydraulic head, per unit volume of the aquifer [Riley, 1969; Saar and Manga, 2003]:

$$S_s = \rho g(\alpha + n\beta) \quad (3.2)$$

where ρ is the water density, g is the gravitational acceleration, α is the bulk aquifer compressibility (at constant vertical stress and zero lateral strain), n is the porosity, and β is the compressibility of water ($4.6 \times 10^{-10} \text{ m}^2/\text{N}$). The bulk aquifer compressibility α describes the relative volume change of the aquifer skeleton in response to a pressure change.

The dimensionless storage coefficient for a confined aquifer characterizes the volume of water drained per unit decline in hydraulic head, per unit area of the aquifer. The storage coefficient S is the vertical integration of the specific skeletal storage coefficient [Riley, 1969], assuming that the water compressibility is negligible with respect to the deformation of the aquifer systems,

$$S = S_s b \quad (3.3)$$

where S_s is the skeletal specific storage coefficient, and b is the aquifer thickness [Riley, 1969; Chaussard et al., 2014].

The storage coefficient can be classified into inelastic or elastic when the effective stress is larger or smaller than the preconsolidation stress, which is subject to the historical hydraulic head levels and ground deformation. The hydraulic head can be obtained from the water level measurement at piezometric wells when the piezometer bottom is fixed. I focus on characterizing the elastic storage coefficient because no long-term compaction has been observed in the study area (discussed in section 3.4.1). The elastic storage coefficient can be solved by the linear regression:

$$S = \Delta d_e / \Delta h \quad (3.4)$$

where Δd_e is the elastic (seasonal) vertical deformation and Δh is the head change [Riley, 1969; Chaussard et al., 2014; Miller and Shirzaei, 2015; Chen et al., 2016; Miller et al., 2017].

Different from the decay coefficient, the estimation of storage coefficient (S), specific storage coefficient (S_s) and bulk aquifer compressibility (α) require water level data in addition to the vertical deformation measurements. And more importantly, water level data with both a high sampling rate and a distinct peak-to-trough amplitude are highly desired for enhancing the signal-to-noise ratio.

Deformation and water level measurements provide a straightforward method to solve for the storage coefficient: first, pick up the peaks and troughs in each water level time series and resample the deformation for the common dates; second, calculate the change between adjacent estimates to obtain seasonal variations; and third, fit the linear regression that pass through (0, 0), and then the slope corresponds to storage coefficient [Chaussard et al., 2014]. However, this method is only useful when the time-series ground deformation is in phase with water levels at a similar frequency, i.e., there is no phase delay for the surface movement in response to head changes. An alternative method is to find the optimal storage coefficient S and time lag τ that minimize the objective function $\|d_{detrend}(t + \tau) - S \times h_{detrend}(t)\|$ [Chen et al., 2016], where $d_{detrend}(t)$ and $h_{detrend}(t)$ are the detrended ground deformation and water levels at time t , respectively. Time lags may occur and differ for the hydrologic units to equilibrate to the additional stress. The length of time lag depends on factors such as the specific storage, the thickness, and the vertical hydraulic conductivity of each stratum [Riley, 1969; Chen et al., 2016].

3.4 Results

3.4.1 Spatial features of the deformation field

The velocity map derived from ENVISAT data indicates six-year (2004-2010) net uplift southwest of downtown Salt Lake City at an average rate of 15 mm/yr (Figure 3.6a). The uplifting area of interest (UAOI) is constrained within the confined discharge areas, which to some extent,

confirms the validity of pre-defined aquifer boundaries. Nevertheless, subsidence occurs from April to August, 2016 according to Sentinel-1A results (Figure 3.6b) at the same location of the net uplift. The summer months' deformation represents the seasonal amplitude. The similar spatial distribution of the deforming signatures derived from these two independent datasets suggests that the observed long-term uplift and seasonal oscillation originate from the same aquifer unit.

The boundaries of the UAOI are also coincident with the locations of a few known faults, suggesting that these faults define and perhaps control the groundwater flow. I also identify a sharp discontinuity (black dashed line in Figures 3.6a and b) at the northern tip of the UAOI, and I suspect this indicates a blind fault orthogonal to the pre-existing $\sim 30^\circ$ northwest-trending fault west of downtown Salt Lake City, probably a step-over that bridges the parallel WFZ at the base of Wasatch Range and WVFZ to the west side of Jordan River.

CT points exhibiting seasonal deformation (red points in Figure 3.6c) are concentrated around downtown Salt Lake City, bounded by inner-valley WVFZ and mountain-front WFZ, and the seasonal cluster contains the UAOI. Additionally, I have identified two localized subsiding sites shown without seasonality in North Salt Lake and Lehi (locations marked with black circles in Figure 3.6, see details in section 3.5.1 and Figure 3.15).

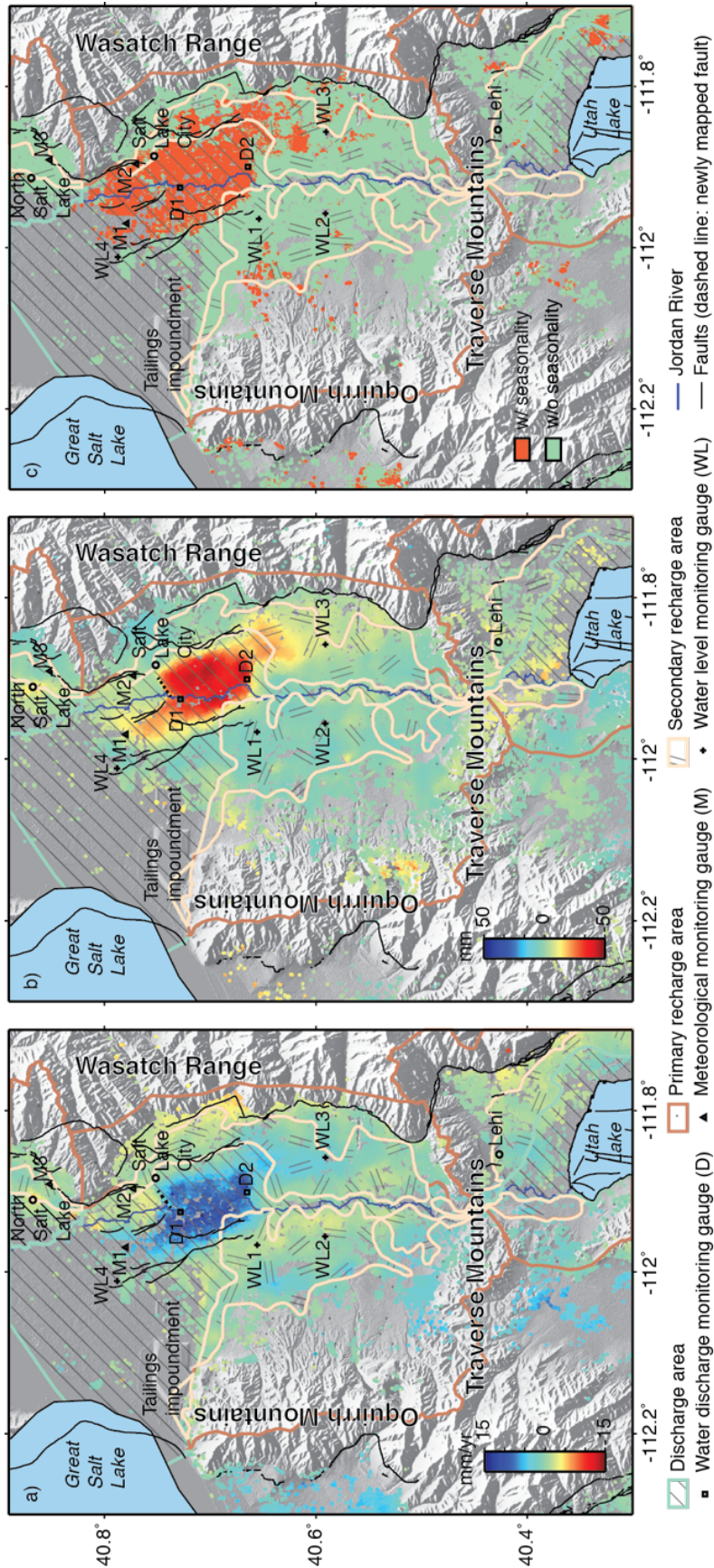


Figure 3.6 Vertical deformation and its feature of seasonality over Salt Lake Valley. (a) Long-term deformation velocity derived from ENVISAT dataset between September 2004 and October 2010 indicating uplift in blue. (b) Seasonal deformation derived from Sentinel-1A dataset between April and August 2015 indicating subsidence in red. (c) Map of deformation seasonality. Squares, triangles and crosses represent the locations of the water discharge monitoring gauges (D1 and D2), meteorological monitoring gauges (M1, M2 and M3) and water level monitoring gauges (WL1, WL2 and WL3), respectively. Black lines show the known faults. Black dashed line (west of Salt Lake City) delineates the deformation discontinuity which may correspond to a blind fault segment. Water discharge, primary recharge and secondary recharge areas are shown with the specified patterns.

3.4.2 Time-series vertical deformation versus water discharge and precipitation

The long-term trend from 2004-2010 indicates clear net uplift. Time-series InSAR analysis allows us to further discern the seasonal dynamics of the aquifer basin. The high frequency of Sentinel-1A data sampling improves our understanding of surface movement to less than one-month scale (when I only consider highly coherent acquisitions) over this valley.

To assess the correlation between groundwater and seasonal ground deformation, I collected water discharge time-series data at two gauges, D1 and D2 (squares in Figure 3.6), and precipitation time-series data at three gauges, M1 to M3 (triangles in Figure 3.6), and compared the gauge data to the InSAR-derived deformation of CT points coinciding with the gauge locations. Groundwater discharge into streams accounts for almost half of the total amount of discharge in Salt Lake Valley [Thiros et al., 2010], and can be approximated by hydrographs of streams at low elevations receiving the water discharge, such as the Jordan River. The two streamflow monitoring gauges (D1 and D2) are located around the boundary of the UAOI along the river. I observed a clear phase shift between ground deformation and the water discharge rate at the two gauges (Figure 3.7), prompting us to consider the modulation associated with the water recharge process, and specifically precipitation. Three meteorological monitoring gauges (M1, M2 and M3) are located in the discharge area: one (M3) is located in North Salt Lake, and the other two (M1 and M2) are equidistant to the axis of the Jordan River at two sides, with M1 on the west side located at the northern tip of the UAOI. Precipitation follows seasonal variation and peaks in winter (Figure 3.8).

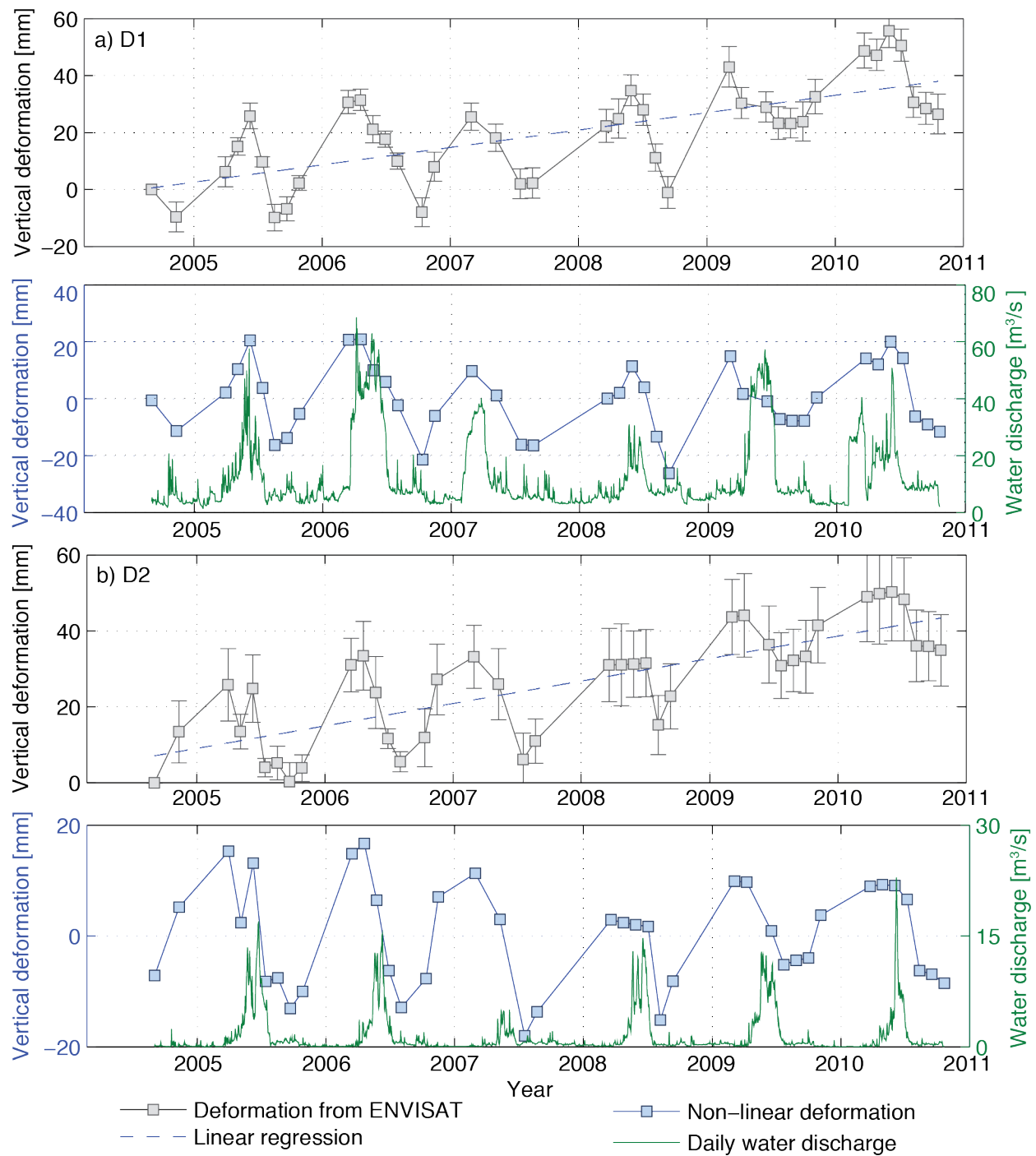


Figure 3.7 Comparison between time-series ground deformation and water discharge monitoring gauge D1 (a) and gauge D2 (b) (location shown in Figure 3.6). Gray squares show the original deformation measured by ENVISAT dataset, and the underlying blue dashed lines show the corresponding linear regression. Error bars are the standard deviations of the deformation estimates within 700 m of the water discharge monitoring gauge. Blue squares show the non-linear deformation component. Green lines show the water discharge rate in cubic meters per second.

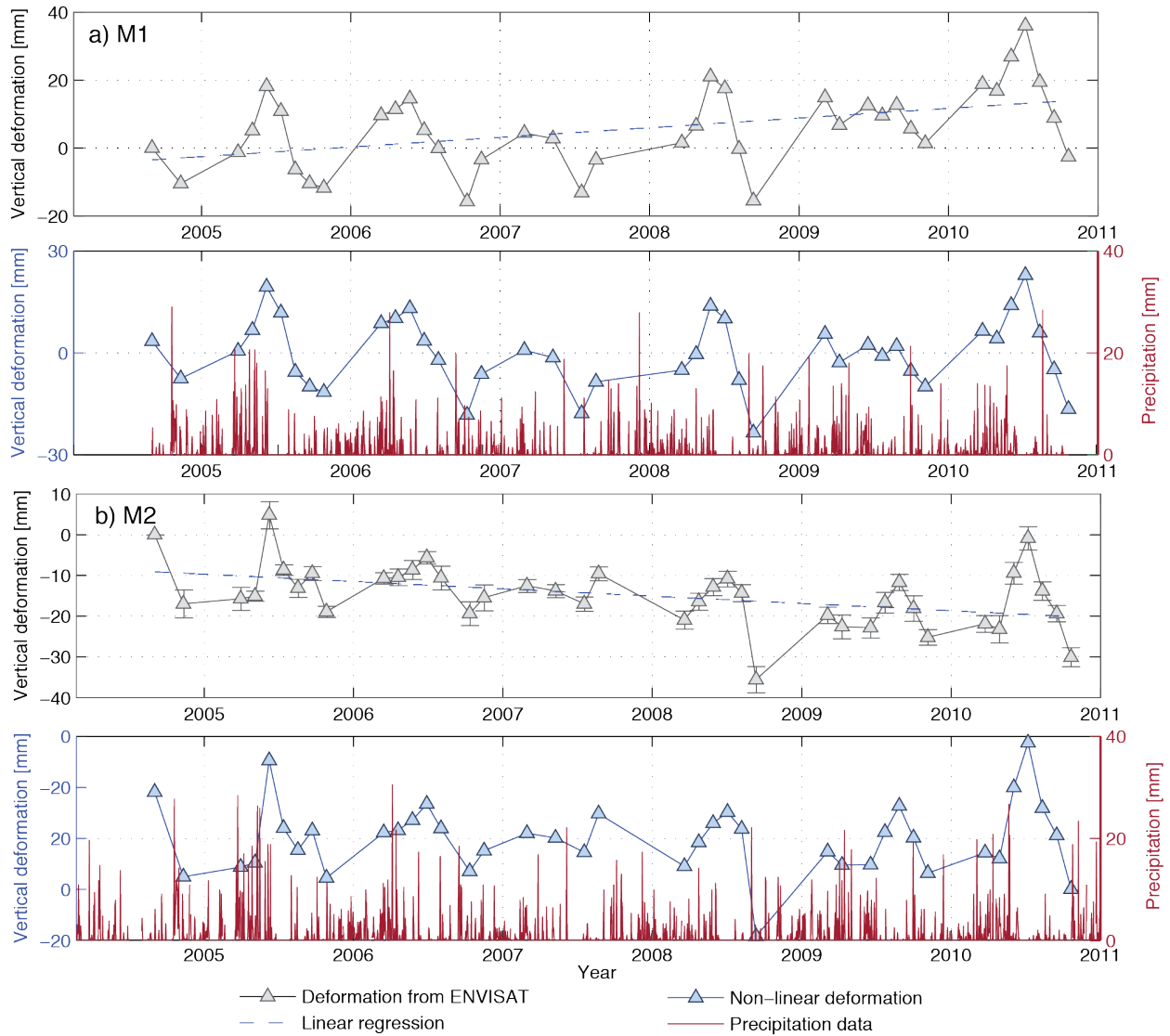


Figure 3.8 Comparison between time-series ground deformation and meteorological monitoring gauge M1 (a) and gauge M2 (b) (location shown in Figure 3.6). Gray triangles show the original deformation measured by ENVISAT dataset, and the underlying blue dashed lines show the corresponding linear regression. Error bars are the standard deviations of the deformation estimates within 700 m of the meteorological monitoring gauge. Only one target was located within the 700-m radius of gauge M1, so no error bar has been given. Blue triangles show the non-linear deformation component. Red lines indicate the volume of precipitation in millimeters.

To better understand the dynamics of hydrologically driven deformation, I need to consider both water discharge and recharge processes. Extraction of the deformation measurements of the CT points near the water discharge monitoring gauge D1 reveals a net uplift averaging 15 mm/yr from 2004 to 2010 (Figure 3.9a). I also observed a seasonal ground oscillation with subsidence during the mid-spring and summer months (March/April to August) and uplift during fall and winter months, with the largest peak-to-trough magnitude of more than 40 mm (Figure 3.9b). I consistently observed such seasonal signature during both time intervals. Assuming that the meteorological monitoring gauge at M1 depicts the precipitation received by the gauge 6.8 km southward at D1, I quantitatively compared the seasonal deformation component with water discharge rate and precipitation by calculating their cross-correlation. To facilitate the interpretation, I constrained the time shift to one year, and calculated the cross correlation between time-series deformation and water discharge/precipitation. The ground uplift and subsidence seem related to hydrological processes (such as precipitation and water discharge); all exhibit seasonal signatures. The influx of water, such as the infiltration of precipitation into the subsurface, can elevate the pore pressure, thereby reducing the vertical effective stress on the skeletal matrix of the aquifer and exerting regional uplift [e.g., Schmidt and Bürgmann, 2003]; when the amount of precipitation declines, the water discharge (such as seepage to the lower elevation Jordan River and Great Salt Lake, and anthropological groundwater extraction) exceeds influx, resulting in an elastic response to the reduction of pore pressure and an increase of the vertical effective stress, expressed as regional subsidence through the settling of grains.

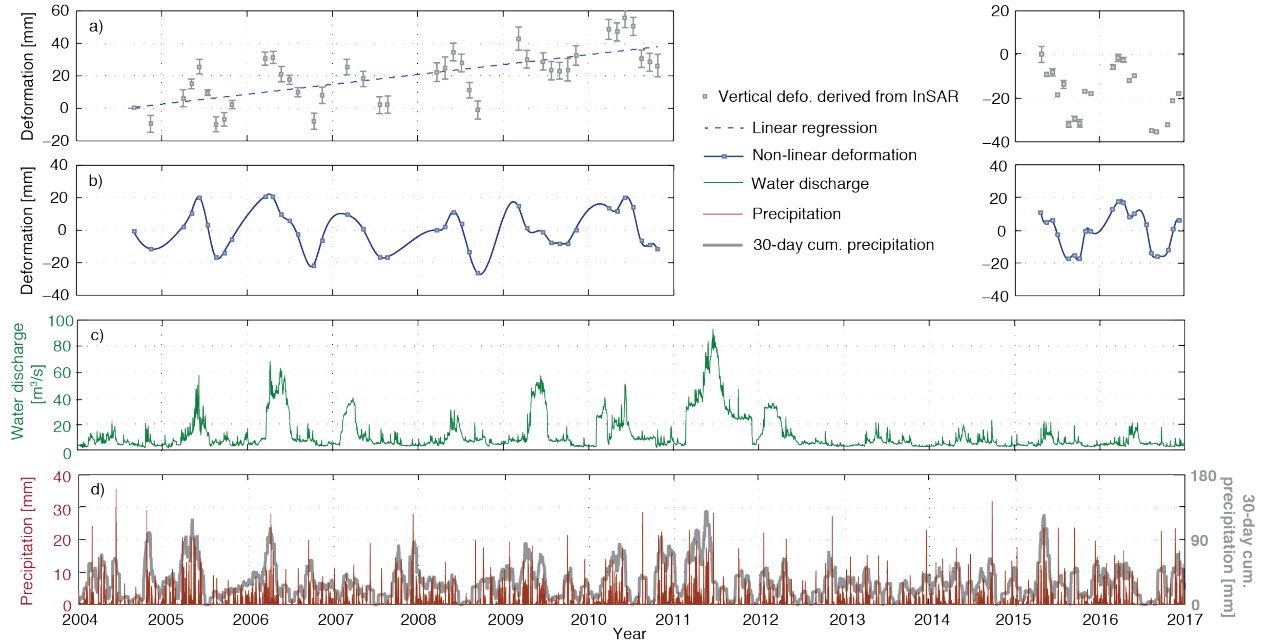


Figure 3.9 Time-series ground deformation (at location D1), water discharge (D1), and precipitation (M1). (a) InSAR-derived deformation (gray squares) and its linear fitting (dashed blue line). Error bars are the standard deviations of the deformation estimates within 700 m of gauge D1. (b) Linearly detrended/seasonal deformation (blue squares) and the spline fitting (solid blue line). In (a) and (b), the left panels are the results of ENVISAT (available for 2004-2010) and the right panels are the results of Sentinel-1A (available for 2015-2016). (c) Water discharge (green line). (d) Daily precipitation (red line, referring to the left Y axis) and 30-day cumulative precipitation (gray line, referring to the right Y axis).

3.4.3 Long-term decay coefficient

The decay coefficient describes the long-term delayed ground response to hydraulic head changes based on the exponential fitting of Equation (3.1). The characteristic time scale of the exponential decay can be taken from the absolute value of the inverse of decay coefficient. To enhance the robustness, I only considered those pixels with a Root Mean Square Error (RMSE) of the best fitting exponential regression of less than 0.8 cm. The distributions of fault systems on the maps of decay coefficient (Figures 3.10a and b) and deformation velocity (Figures 3.6a and b) suggest that the faults partition the hydrological units and control the deformation field. In particular, besides the $\sim 60^\circ$ northeast-trending fault unveiled by the deformation velocity map, I have also identified another previously unknown $\sim 30^\circ$ northwest-trending fault from the decay

coefficient map, all of which together provide a complete view of the fault configurations in the area of Salt Lake City.

Within the area exhibiting seasonal deformation (red dotted area in Figure 3.6c; yellow dotted-line area in Figure 3.10a), the northern and southern areas at the mountain front occupy a smaller decay coefficient, suggesting a faster response to a given hydraulic change than the central section (Figure 3.10a). The negative values of coefficient M suggest net uplift and the positive values suggest net subsidence (Figure 3.10b), which is consistent with the map of long-term deformation velocity (Figure 3.6a). The decay coefficient of the UAOI is mainly in the range between -0.1 and -0.01, suggesting a time constant of 10 to 100 years. This exponential fitting is designed to simulate the decaying process. Large RMSE (Figure 3.10c) accompanying the exponential fitting generally result from either substantially fluctuated deformation or the accelerated or quasi-linear trend of deformation, that I discuss further in section 3.5.1.

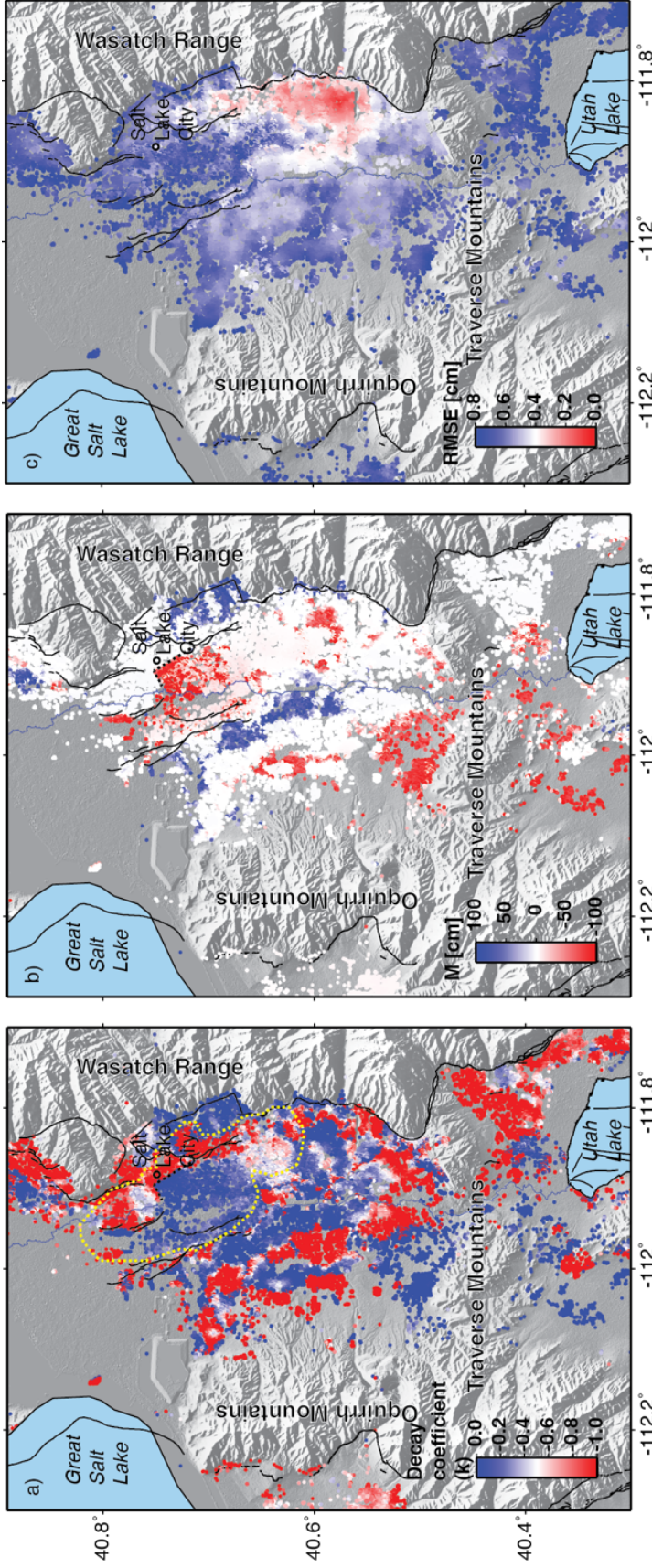


Figure 3.10 Exponentially decaying deformation explained by $d(t) = M(e^{kt} - 1)$. (a) Decay coefficient k . Blue (closer to 0) means slower equilibration, and red (closer to -1) means faster equilibration to the hydraulic head change. (b) Magnitude coefficient M . Red (negative value) means net uplift and blue (positive value) means net subsidence. (c) RMSE of the exponentially decaying model. Black dashed lines are known faults. Black dotted lines (west and south of Salt Lake City) in (a) and (b) are newly mapped faults in this study. Yellow dotted-line area in (a) highlights the seasonally deforming area.

3.4.4 Storage coefficient and bulk compressibility

Accurate derivation of the aquifer storage coefficient requires water level measurements. However, many long-term water leveling gauges in this region only record measurements once a year, and even worse, generally in the same season (February or March). Only four gauges (locations are indicated as crosses in Figure 3.6) provide frequent enough measurements to estimate the storage coefficient: WL1, WL2 and WL3, with nearly daily measurements from the USGS throughout the entire InSAR acquisition timespan, and WL4 with nearly monthly measurements from the Utah Geological Survey during 2009-2010.

The input detrended water level $h_{detrend}(t)$ is simply the non-linear component. However, the parameterization of input detrended deformation $d_{detrend}(t)$ depends on whether or not it includes a seasonal signal. If seasonality exists, the detrended deformation is considered to be the seasonal component simulated by the superposition of three sinusoidal functions; otherwise, the spline interpolation of the linearly detrended deformation was applied. Original time-series deformation and water level are shown as black crosses with error bars and orange line, respectively, in Figure 3.11. The water level data at WL2 and WL3 exhibit periodic seasonal variations (yellow lines in Figures 3.11b and c) and I identify targets deformed with seasonality in the vicinity of WL2 and WL3 (Figure 3.6c). Water level at WL1 does not show evident seasonal variation, and coincidentally, no target around this gauge has been identified with seasonal deformation (Figure 3.11a). Nevertheless, WL4 only has one-year water level data and the existence of seasonality in deformation during this year has not been determined, so I use the spline interpolation of the linearly detrended deformation (Figure 3.11d).

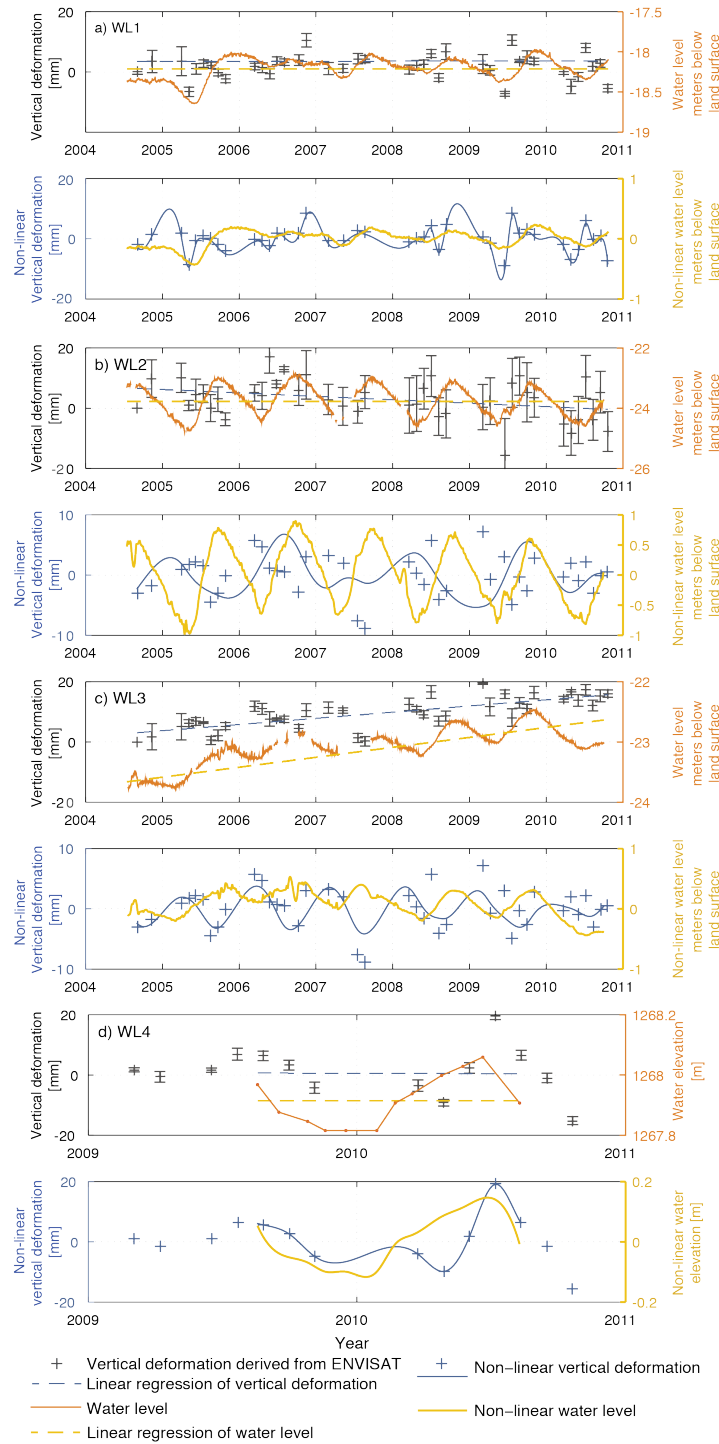


Figure 3.11 Comparison between time-series ground deformation and water level monitoring gauges WL1 (a), WL2 (b), and WL3 (c) and WL4 (d) (locations shown in Figure 3.6). Black crosses show the original deformation measured by ENVISAT dataset, and the underlying blue dashed lines show the corresponding linear regression. Orange lines show the original water level measurements in meters, and the underlying yellow dashed line show the corresponding linear regression. Blue crosses and solid lines show the detrended ground deformation. Yellow solid lines show the detrended water level measurements.

Considering that the period of seasonal deformation and water level is around one year, I set the delay time τ from 0 to 365 days to avoid aliasing. The estimated storage coefficients from well data [Thiros, 2003] range between 0.0005 and 0.1, and are taken as the search window for the storage coefficient (S). The best-fit results are shown in Table 3.1. WL2, in the central south of the valley, occupies the smallest storage coefficient (0.002), while WL4, in the wetlands near Great Salt Lake, has a greater storage coefficient (0.0668), suggesting a larger amount of groundwater communication at WL4 in response to given head change. The interpolated map of storage coefficient is shown in Figure 3.12a.

WL4 occupies the smallest time lag of 43 days, while the time lags for WL1-3 range between 120 and 306 days. A lengthy time lag may suggest slow infiltration and slow drainage of the clay lenses around the wells. Aquifer thickness, were approximated by the thickness of the unconsolidated and semi-consolidated deposits (digitized from the isopach map, Figure 3.12b) [Mattick, 1970; Arnou and Mattick, 1968], which includes the Quaternary and partial Tertiary deposits. The thickest (~1220 m) unconsolidated and semi-consolidated sediments are located in the northwest and northeast parts of the valley. It thins toward the central valley (~600 m) and thickens again gradually toward the south (~800 m). The thinnest (<300 m) part is located along the margins of the valley. I apply basin-wide porosity estimates (Figure 3.12d) ranging between 0.06 and 0.25 from Starn et al. [2015]. In agreement with the compositions of unconsolidated to semi-consolidated clay, silt, sand, gravel, tuff, and lava of the Tertiary- and Quaternary-age basin-fill deposits in Salt Lake Valley [Wallace and Lowe, 2009; Thiros et al., 2010], the derived specific storage coefficient S_s (Figure 3.12c) and the bulk aquifer compressibility α (Figure 3.12e) are in a reasonable range for these general sediment types [Domenico and Mifflin, 1965; Chaussard et al., 2014; Hanson, 1989; Nelson, 1982; Neuman and Witherspoon, 1972; Sneed, 2001; Sneed et

al., 2007]. The S_s and α of the UAOI southwest of Salt Lake City are $3.8 \times 10^{-5} \text{ m}^{-1}$ and $1.0 \times 10^{-9} \text{ m}^2/\text{N}$, respectively. Given the biases due to the water compressibility, the resulting values for bulk aquifer compressibility α are of the same order, which are mainly influenced by the values for the specific storage S_s because the product of porosity and water compressibility is negligible. The map of aquifer hydrogeological properties can be enhanced if more monthly/seasonally-acquired water level data in this region become available.

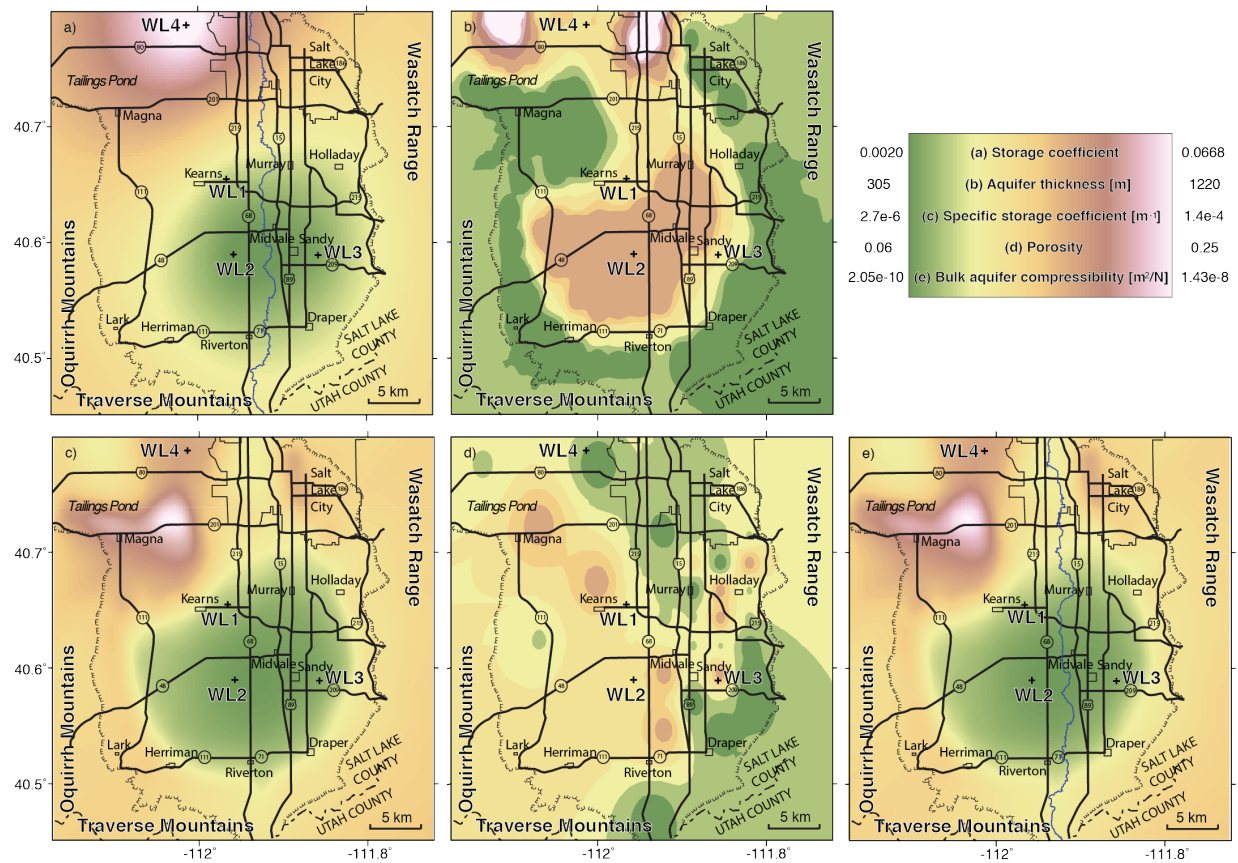


Figure 3.12 The derived hydrogeological properties. (a) Storage coefficient interpolated by four estimates at WL1-4. (b) Basin-wide estimates of aquifer thickness (digitized from the isopach map of unconsolidated and semi-consolidated sediments [Mattick, 1970; Arnow and Mattick, 1968]). (c) specific storage coefficient. (d) Porosity (from the interpolation of the estimates at pilot points [Starn et al., 2015]). (e) Bulk aquifer compressibility considering non-zero water compressibility.

Table 3.1 Hydrogeological properties at water level gauges (WL1-4).

Site	Lon W[°]	Lat N[°]	S	τ [day s]	Res. [mm]	b [m]	S_s [m ⁻¹]	n	α [m ² /N] (negligible β)	α [m ² /N] (non-zero β)
WL1	111.97	40.65	0.0116	306	4.0	631	2e-5	0.1187	2e-9	1.95e-9
WL2	111.96	40.59	0.0022	239	3.0	879	3e-6	0.1392	2e-10	2.36e-10
WL3	111.86	40.59	0.0047	120	1.9	614	8e-6	0.1493	7e-10	7.31e-10
WL4	112.02	40.79	0.0668	43	5.8	706	9e-5	0.0799	9e-9	8.96e-9
<p>* S is the storage coefficient, τ is the delay time between the detrended ground deformation and head changes, Res. is the residual of the optimal solution for $\ d_{detrend}(t + \tau) - S \times h(t)\$, b is the aquifer thickness that approximated by the thickness of unconsolidated and semi-consolidated sediments, S_s is the specific storage, n is the porosity, α is bulk aquifer compressibility. The locations of the sites, b, and n are priori-knowns, and the other parameters are derived.</p>										

3.4.5 Analytic modeling of the groundwater reservoir

In the long time span, the reservoir in the area of interest produces tensile vertical shear stress due to upward hydraulic head, and exerts extensional strain and ground surface uplift. I simulate the long-term displacement field associated with deforming vertical shear zones using the analytic modeling of cuboid groundwater reservoir [Barbot et al., 2017]. To match the outstanding imprint at the surface, I assume the reservoir is by size of 9×6 km and striking at -20° to the north. The target reservoir is located in the water discharge area, where water sometimes reaches the surface at artesian wells. The shallow unconfined aquifer, if it exists in the top layer, has a maximum thickness of 15 m [Snyder and Lowe, 1998; Wallace and Lowe, 2009], and is negligible when considering the underlying several-hundred-meter confined part of the aquifer. The median depth to top of the well screen in the deeper part of aquifer of discharge area is 120 m and the median well depth is 285 m [Thiros, 2010], implying that the reservoir goes through the shallow alluvial aquifer, upper confining units, and deeper into the permeable aquifer by 285 m or more. The Poisson's ratio in the half space is set to be 0.33. The thickness of the reservoir is approximated

by the thickness of unconsolidated and semi-consolidated sediments, which is around 500-600 m at this location.

The cross-section profile (dashed line in Figure 3.13) in SAR observation of the deformation velocity field shows that the peak-to-trough amplitude is ~ 15 mm/yr along LOS direction, that is, ~ 16 mm/yr in vertical direction. The model shows the surface deformation on radar LOS under the expansion of the regular cubic reservoir beneath the surface. The bulge is asymmetric - the eastern side of Jordan River has larger LOS displacement and a sharper boundary than the western side. This is because the eastern side is closer to the incoming radar pulse from the descending-orbit and right-looking sensor, and thus has a smaller angle of incidence. However, the results of InSAR observation seem to show no significant difference between LOS displacements on the western and eastern sides of Jordan River. The difference suggests that the western side might contain a thicker reservoir and/or larger source strain.

I first assume a uniform thickness for the cuboid reservoir. Minimizing the residual between the observation and the model, produces a solution with 2×10^{-5} isotropic source strain rate when the thickness of the reservoir is 500 m, i.e., a volume of 27-km^3 reservoir skeleton, and the annual expansion rate is $5.4 \times 10^5 \text{ m}^3/\text{yr}$; a 1.7×10^{-5} isotropic source strain rate when the thickness is 600 m, i.e., 32.4-km^3 reservoir skeleton, and the annual expansion rate is $5.5 \times 10^5 \text{ m}^3/\text{yr}$. I further considered the effect of varied thickness by applying the quad-cuboid, and the distribution of the cuboid depends on the pattern of the displacement field. Given a homogeneous hydrologic unit with a uniform strain rate of 2×10^{-5} , the best fit results reveal a much thicker shearing zone at the west side (600 m) than the east side (350-375 m), and the volume (30.7 km^3) is in between the previous two situations, but the annual expansion rate is the largest ($6.1 \times 10^5 \text{ m}^3/\text{yr}$). The residual of the quad-cuboid model is the least (Table 3.2).

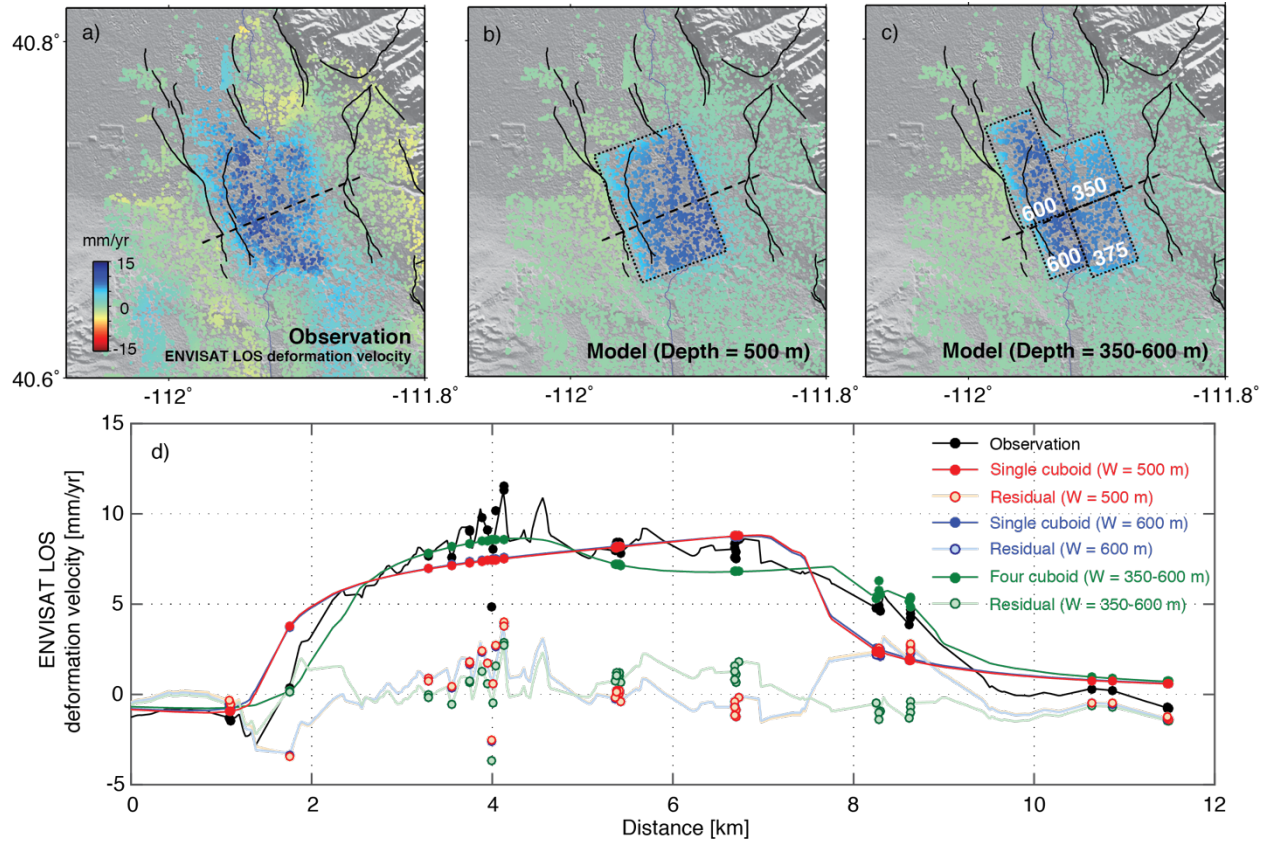


Figure 3.13 Groundwater reservoir modeling of the annual uplifting area. (a) ENVISAT observation. (b) analytical solution when one single cuboid with the thickness (W) of 500 m. (c) quad-cuboid with varied thickness, and the numbers in the cuboids indicate the best-fit thickness. And (d) the comparison between the observation and model results along the dashed-line profile for a single cuboid (W = 500 or 600 m), and for a quad-cuboid with varied thickness.

Table 3.2 Best fit results for the analytic modeling.

	Thickness [m]	Volume [km ³]	Strain rate	Annual expansion rate [m ³ /yr]	Residual [mm]
Single cuboid	500	27	2×10^{-5}	5.4×10^5	1.69
	600	32.4	1.7×10^{-5}	5.5×10^5	1.68
Quad-cuboids	350-600	30.7	2×10^{-5}	6.1×10^5	1.54

Based on the assumption of point-source dilatation in elastic half space, another simple approximation on the estimate of subsurface volume due to fluid injection is given by [Mogi, 1958;

Shirzaei et al., 2016], $dv = \frac{\iint_{-\infty}^{+\infty} LOS \, dx dy}{2(1-\nu)l_z}$, where l_z is radar's look vector in the vertical direction,

and ν is the Poisson's ratio. The long-term uplift of Salt Lake Valley shares a similar mechanism due to increased pore pressure and decreased effective stress. The displacement field is manifested by the distributed CT points; however, I expect spatially continuous estimates in order to calculate the total subsurface volume change over the area of interest. Since long-term averaged deformation is expected to be a low frequency 2D signal, I downsample the data points to further eliminate the potential outliers. The uniform downsampling algorithm uses a regular grid and has the trade-off between data reduction efficiency and deformation details preservation. Alternatively, spatially variant downsample methods, such as quadtree partitioning (quadtree algorithm) [Jónsson, 2002], can better resolve this problem. I can roughly estimate the overall strain rate by assuming multiple point-source dilatation in the reservoir, where the point sources can be projected at the center of each quadtree partitioning (Figure 3.14). I also assume that the reservoir layer is spatially homogeneous with the same Poisson's ratio ν (0.33). The annual volume change is estimated to be $5.4 \times 10^5 \text{ m}^3$, which is in agreement with the analytical modeling.

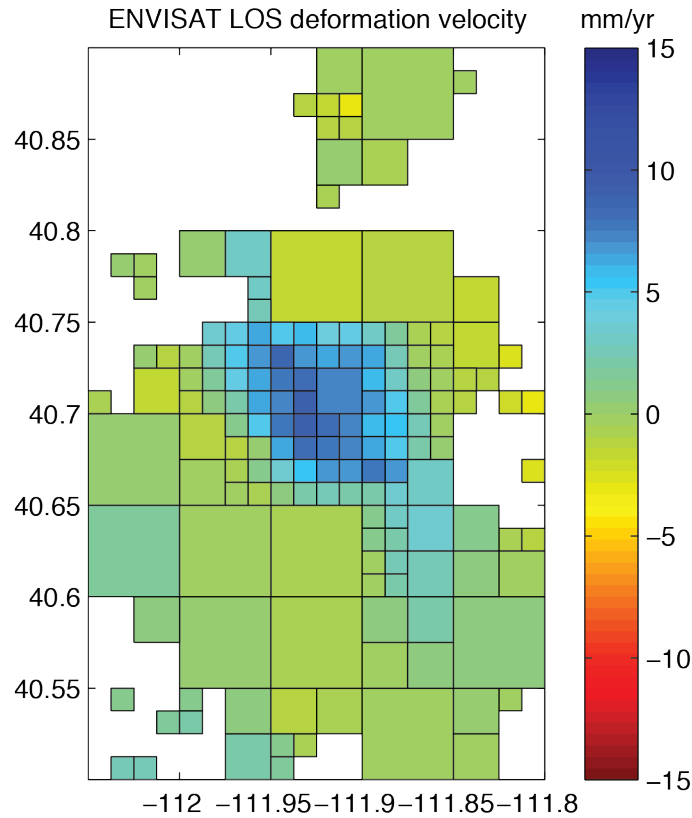


Figure 3.14 Quadtree representation of ENVISAT LOS deformation velocity.

3.5 Discussion and conclusions

3.5.1 Localized anthropogenic deformation and basin-wide hydrogeologic effects

I observed two localized subsiding sites over the industrial fields in North Salt Lake and the foot of the Traverse Mountains in Lehi. Both sites are located in areas with no seasonal deformation and with large RMSE from the exponentially decaying model. The North Salt Lake site shows continuous quasi-linear subsidence at a rate of ~ 20 mm/yr, which accelerated during 2015-2016 (Figure 3.15d) compared with the period of 2004-2010 (Figure 3.15a). One meteorological monitoring gauge (M3 in Figure 3.6) is located 2 km southeast of this site. However, I do not see a correlation between the non-linear ground deformation and precipitation (Figure 3.15b), suggesting the deformation here is less likely to be influenced by natural hydrological process. The aerial image shows a group of round-top infrastructures over the

subsiding site at North Salt Lake (Figure 3.15c), probably related to industrial production, suggesting that human activities are potentially responsible for the observed subsidence. I also observed an actively (throughout 2015-2016) subsiding site (Figure 3.15e) near an electronics manufacturing company in Lehi; however, such drastic subsidence has not been identified in the 2004-2010 results. Surface fissures started to develop dramatically between 2010 and 2013 (Figure 3.15f), and continued growing through July 2016 or afterwards. An aging of asphalt may be another reason for the fissures.

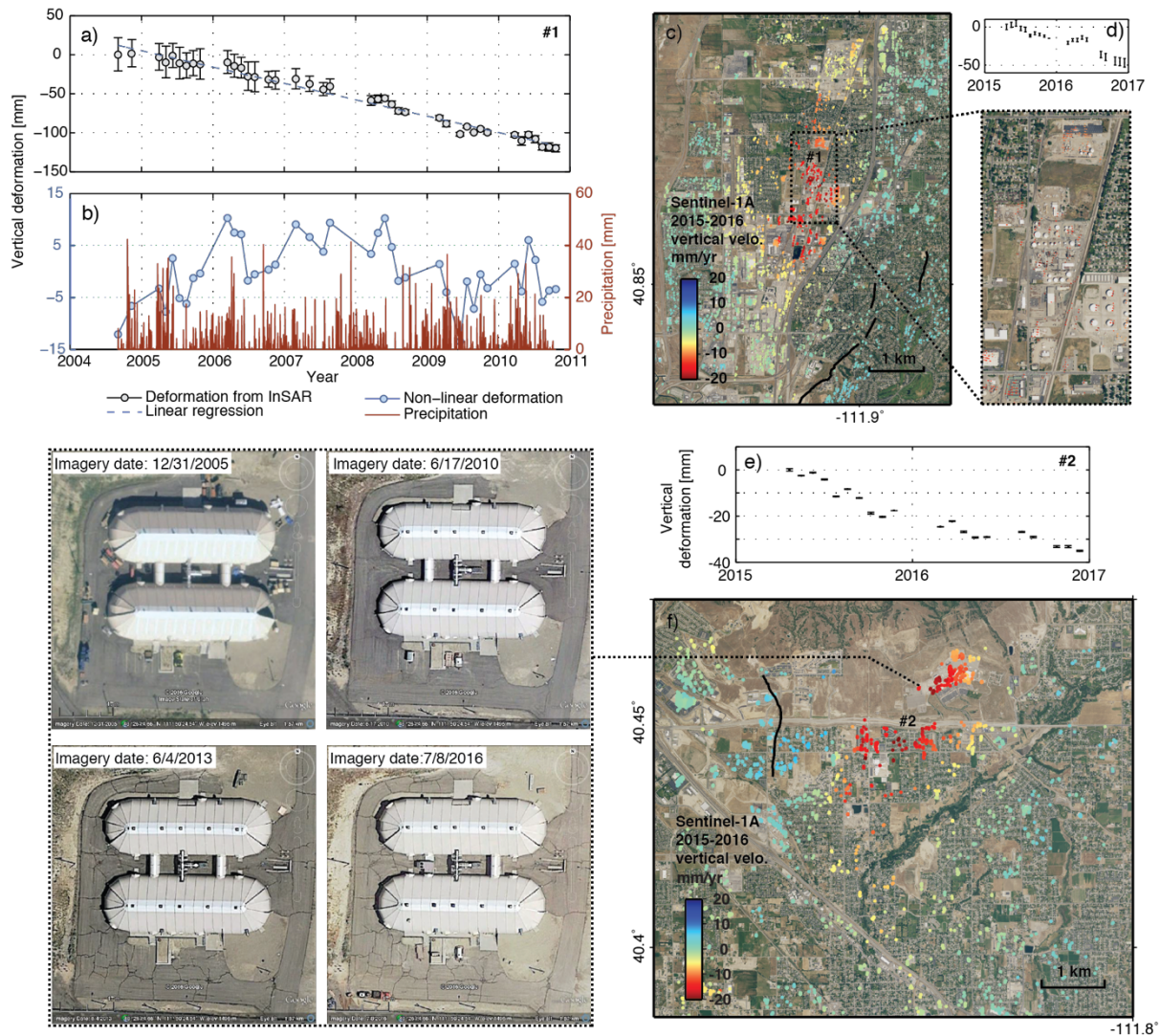


Figure 3.15 Localized subsidence in North Salt Lake (a)-(d) and Lehi (e)-(f). (a) and (d) Cumulative vertical deformation in North Salt Lake during 2004-2010 and 2015-2016, respectively. (b) Cumulative non-linear vertical deformation against precipitation. (c) Vertical deformation velocity in North Salt Lake during 2015-2016, with the area of subsidence enlarged. (e) Cumulative vertical deformation in Lehi during 2015-2016. (f) Vertical deformation velocity in Lehi during 2015-2016, with a subsiding site enlarged, to show the development of fissures. Error bars in panels a, d and e are the standard deviations of the deformation estimates within 200 m of the selected target.

The observed localized subsidence shows different deformation patterns compared with the time series over the confined aquifer. The temporal features of seasonality and the residuals of exponentially decaying model may be used to characterize the deformation related to both hydrological processes and industrial production. For example, the net uplift of the hydrological

unit highlighted by the high-resolution deformation map (Figure 3.6a) is marked by seasonality and large RMSE due to significantly fluctuating deformation, while the other hydrological units with no detectable motions are marked by no seasonality and small residuals. On the other hand, the industrial production is characterized by no seasonality and large RMSE due to accelerated or quasi-linear trend of deformation.

3.5.2 Long-term deformation due to a delayed response to the prolonged head changes

The aquifer skeletal response to changes in subsurface water levels is not instantaneous, and may take years to appear as surface deformation. According to a USGS report [Burden et al., 2005] on the groundwater conditions during 1975-2005 in Salt Lake Valley, water levels in the principal aquifer mostly declined, probably due to increased withdrawal and decreased precipitation. The greatest water level decline occurred south of Holladay and east of Midvale (grey shaded areas, Figure 3.16). The ground subsidence observed along the mountain front of the Wasatch Range and Jordan River banks, can be explained by this prolonged water level decline. Remarkably, ground water level has increased in the downtown area and the northwestern part of the valley (dotted area in Figure 3.16), which is consistent with the ground uplift derived from the ENVISAT data.

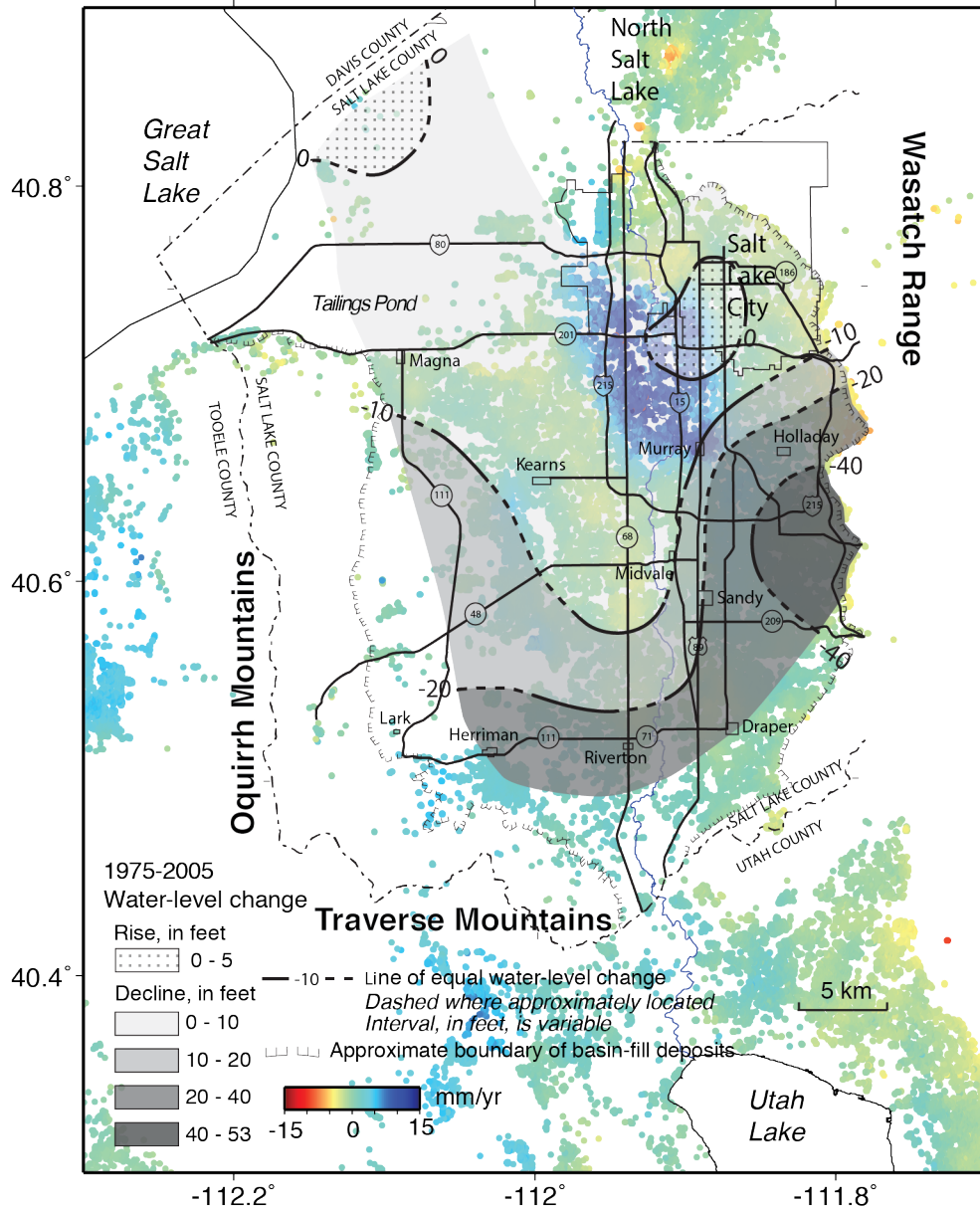


Figure 3.16 Map of ground water level changes from 1975 to 2005, digitalized from Burden et al., 2005, superimposed on the long-term vertical deformation velocity derived from 2004-2010 ENVISAT data.

I infer that the uplift signature over the UAOI may result from the on-site water level increase. When the seasonal recharge of groundwater exceeds the amount of discharge over a long time span, the accompanying water level increase leads to net uplift of the surface when the vertical hydraulic conductivity is low enough to avoid rapid fluid diffusion [Miller et al., 2017]. This is

consistent with a large decay coefficient (-0.1 to -0.01) and thus slow equilibrium to the head changes at the heart of the UAOI. Interestingly, the water level change map of 1975-2005 shows that there is a small outstanding area with slight water level rise (0-5 feet or 1.5 meters) in Salt Lake City. However, the map for 1970-2000 [Burden et al., 2000] shows a border area with increased water level at the foot of the Wasatch Range. This area extends southwest to form an elliptical shape with its long axis oriented at an azimuth of approximately 45 degrees east of north in the water level change map of 1980-2010 [Burden et al., 2010], which is characterized with small water level decline (0-10 feet or 3 meters) in the most recent map of 1985-2015 [Burden et al., 2015]. A similar resemblance between the spatial patterns of groundwater level and displacement in a particular time interval, rather than the earlier or more recent time, has also been observed in Gulf Coast aquifers [Qu et al., 2015].

I have shown that the net uplift at UAOI coincides with the area of net water level increase from 1975 to 2005, suggesting that the net uplift has a lagged response to the head increase, probably decades ago. However, the water level did not consistently increase during 1975-2005. According to the monthly-to-yearly recorded water level data since 1931 (Figure 3.17) at gauge #404506111523301 (40°45'06.68", 111°52'37.24") near the eastern boundary of the UAOI, the water level only increased during 1963-1982 (by ~2 m) and 1990-1995 (by ~1 m), while the water level mainly fluctuated for the time intervals of 1931-1963 and 1995 onwards. The timing and magnitude of the vertical strain for an aquifer also may depend on other parameters, including aquifer thickness, permeability, and storage states, which can change with lithology, or with seismic shaking [e.g., Chaussard et al., 2014].

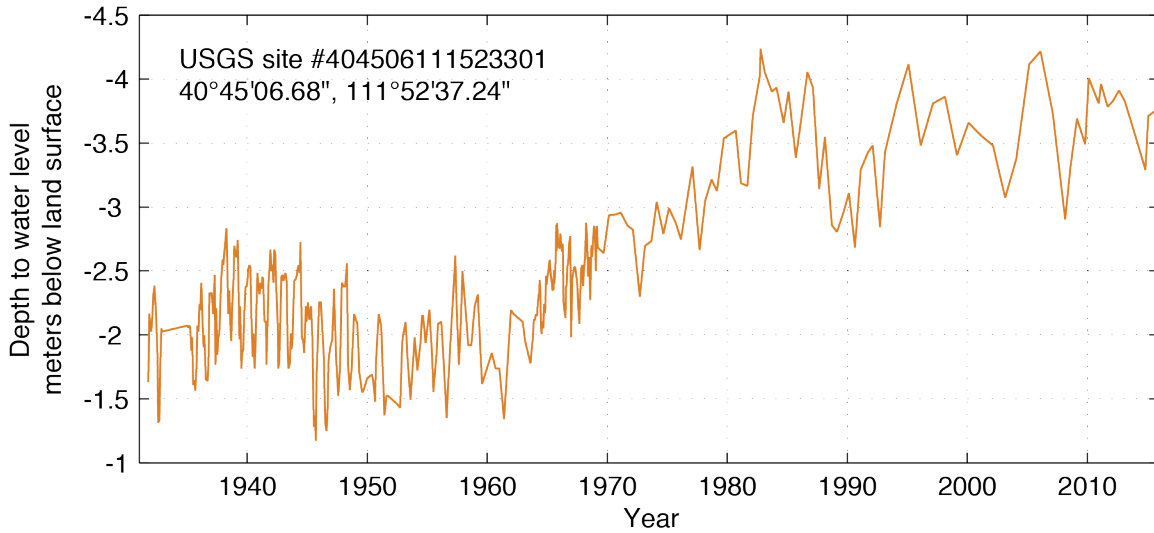


Figure 3.17 Water level of USGS gauge #404506111523301 in the ground uplifting area.

The water-level-change map used in this study was based on an interpolation of measurements at about a dozen of gauges distributed in the aquifer basin, with a temporal sampling rate of only once per year [Burden et al., 2000; 2005; 2010; 2015]. Therefore, the contours of water level change may not be perfectly constrained due to the sparsely distributed gauges. On the other hand, because the ground deformation is approximately proportional to hydraulic head changes, the surface deformation map with estimates covering most of the aquifer, can improve the resolution of water level changes [e.g., Chen et al., 2016].

3.5.3 Salt Lake Valley, UT and Santa Clara Valley, CA: similarities and distinctions

There are similarities in the aquifers below Santa Clara Valley, CA and Salt Lake Valley, UT. They are both located under densely populated areas and both systems possess faults that function as hydrologic barriers, disrupting the subsurface flow of groundwater and modulating the long-term ground deformation [Schmidt and Bürgmann, 2003].

Santa Clara Valley had a subsidence history from 1916 to 1982 [Poland and Ireland, 1988], in contrast to later uplift from 1992 to 2011 due to water recharge [Schmidt and Burgmann, 2003;

Chaussard et al., 2014]. I have also observed an uplift signal in Salt Lake Valley from 2004 to 2010, yet the reason behind the uplift could be different for the two aquifer systems. For Santa Clara Valley, the observed elastic strain is in response to anthropogenic withdrawal and later remedial actions of fluid injection. However, there is no evidence of consistent fluid injection before or during 2004-2010 in Salt Lake Valley, suggesting that the aquifer in Salt Lake Valley responds elastically to the natural hydrological process. Alarmed at the social and environmental problems caused by the uncontrolled groundwater withdrawal in Santa Clara Valley, particular attention needs to be paid on the prolonged water level decline in most areas of Salt Lake Valley (Figure 3.17) [Burden et al., 2000; 2005; 2010; 2015]. Once irreversible inelastic subsidence occurs it may cause critical damage to the roads and other infrastructures. Additionally, the valley may face the threat of saltwater intrusion and permanently contaminating the water source if subsidence were to be so pronounced as to allow the groundwater level near the Great Salt Lake to drop below the water level of the lake itself.

3.5.4 Correlation between seismic hazards, seasonal deformation and hydrological process on a monthly scale

Water discharge and recharge may disturb the stress field due to pore pressure changes and may trigger faulting and micro-earthquakes [e.g., Segall et al., 1994]. To investigate the relationship between seismicity and hydrology via the media of ground deformation, I compare the earthquakes, water discharge, precipitation records, and non-linear ground deformation using monthly binned averages, and fit the data with a single frequency sinusoid function (Figure 3.18).

To reduce instrumental bias, I use natural earthquakes since 1962 (archive of University of Utah Seismograph Stations) above latitude 40.6° over the Salt Lake Valley with a minimum local magnitude of 1.25, over which the magnitude and total number of earthquakes obey the Gutenberg-

Richter law [Lay and Wallace, 1995]. I picked main shocks and culled foreshock and aftershock sequences (occurring in consecutive days) to summarize the number of earthquakes for each month. A number of 186 earthquakes with magnitude up to 5.2 and depth ranging between 0.03 and 14.04 km were selected.

I use the water discharge data at gauge D1 and precipitation data at gauge M1 between 2004 and 2015, where they both show regular seasonal oscillation. I use the averaged non-linear deformation over the net uplifting area of interests southwest of the Salt Lake City between 2004 and 2010. Note that the deformation data used in Figure 3.14 include the monthly binned averaged deformation over the entire area of interest, rather than time-series deformation at gauge D1, so that the phase is slightly different from that in Figure 3.9.

The seismic hazard is approximated by the monthly cumulative number, monthly averaged magnitude and monthly averaged earthquakes depth (Figure 3.18a-c). March, July, and October-November seem to have higher seismic hazard than other months, in which March shows the most consistent and profound expressions in the high seismic hazard in terms of large number of earthquakes, large magnitude and shallow depth. March has the most uplift (Figure 3.18d) when the rainfall and snowmelt infiltrate into the subsurface and hydraulic heads elevate; on the other hand, the ground surface compacts the most during August and September, which may be the reason for the least seismic hazard. July is the transit period from relaxation to compaction, and October-November corresponds to the opposite transit, and both periods witness large displacement gradient. However, the explanation of the displacement gradient does not work for March since the displacement gradient is small.

The seasonal deformation is obviously influenced by the water recharge and discharge processes: all three have similar apparent frequency with a period of around one year, yet with

certain time lags (Figure 3.18e-f). Stream discharge (to Jordan river) has been increased from November through June with a significant peak from May to June due to snowmelt. Infiltration of precipitation shows two peaks in April and December, respectively. The apparent net water storage by removing the trend of the water discharge from that of the precipitation, modulates the seasonal deformation but with a few months' delay due to low hydraulic conductivity.

Nevertheless, the apparent wavelength of the monthly binned earthquake records is much shorter than that of the deformation and hydrologic records (Figure 3.18). This might be due to the fact that, under the normal faulting regime, pore pressure changes (either increase or decrease) can bring the effective stress closer to the failure envelope considering the coupling between the minimum horizontal stresses and pore pressures. Overall, there is insufficient evidence to support the correlation between seismic hazard and groundwater processes over the Salt Lake Valley. Worth noting is that the earthquake analysis is highly simplified.

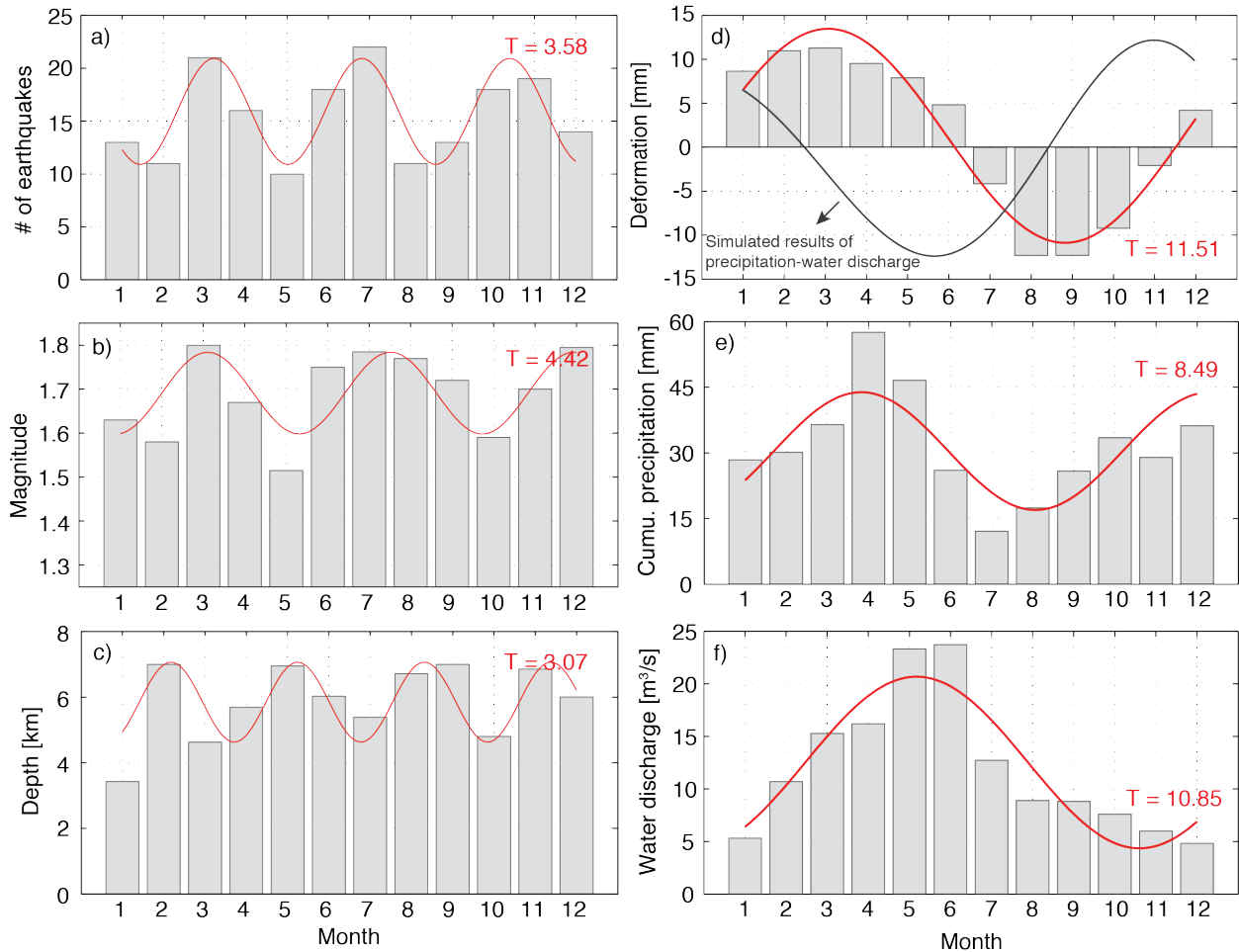


Figure 3.18 Monthly binned histograms showing the number (a), magnitude (b) and depth (c) of tectonic earthquakes, non-linear deformation component of the area of interest (d), cumulative precipitation (e), and water discharge (f). The red lines show the apparent periodic waveform with the corresponding period indicated. The gray line in panel d show the simulated apparent net water storage by removing the trend of the water discharge from that of the precipitation.

I have measured the ground deformation over two time intervals (2004-2010 and 2015-2016) over Salt Lake Valley using multi-temporal InSAR analysis. The InSAR-derived deformation maps highlight seasonal oscillating cycles of uplift and decline as well as a long-term net uplifting area southwest of downtown Salt Lake City. Spatially, the net uplifting area falls within the aquifer systems' discharge area and is bounded by existing faults. The maps of deformation velocity, the seasonality and the decay coefficient help us better evaluate the existing boundaries of principal aquifers and identify some previously unknown fault segments, suggesting the embedded faults

disrupt the groundwater flow and partition the hydrological units. Temporally, the time-series deformation measurements provide insights into the time scale of groundwater exchanged. The cross-correlation with hydrological observations, such as precipitation and water discharge rate, reveals that the ground deformation is modulated by both water recharge and discharge processes. The large seasonal oscillations reflect the rapid redistribution of groundwater. In one location, the long-term uplift corresponds to the prolonged increase in hydraulic head and thus the pore pressure. In addition, two localized subsiding sites were identified through the analysis in North Salt Lake and Lehi, which are more likely due to anthropogenic activities rather than natural hydrological processes. WFZ is probably overdue for damaging earthquakes, and may threaten nearly 80% of Utah's population [USGS, 2016], and deserve our attention and contingency response. InSAR is a powerful monitoring tool that provides timely ground deformation measurements, which can help us better understand the complex kinetic chain associated with anthropogenic and natural activities, earthquake and groundwater processes.

ACKNOWLEDGMENTS

I thank Dr. Teng Wang from Nanyang Technological University (previously at our Radar Lab) for his assistance in InSAR data processing; Dr. Sylvain Barbot from Nanyang Technological University for his assistance in analytic modeling of the groundwater reservoir; Dr. Brian Stump, Dr. Matt Hornbach, and Dr. Jinwoo Kim from Southern Methodist University for useful comments and discussions; *Journal of Geophysical Research: Earth Surface* Associate Editor Joel Johnson and anonymous reviewers for constructive comments; and Ms. Cathy Chickering for language editing. I thank the Utah Automated Geographic Reference Center (AGRC) for providing the locations of recharge and discharge areas of the principal aquifers along the Wasatch Front and adjacent areas, as well as the location of Quaternary faults (<https://gis.utah.gov/data/geoscience/>); Dr. Kris Pankow, University of Utah Seismograph Stations and U.S. Geological Survey (USGS) for providing historic earthquake archives in the study region; USGS for providing water discharge data at gauges 10170500 and 10168000, water level data at gauges (40°39'16"N, 111°57'59"W), (40°35'24"N, 111°57'22"W), (40°35'24"N, 111°51'29"W), and (40°45'07" N, 111°52'37" W) (<https://waterdata.usgs.gov/usa/nwis/>); Utah Geological Survey for providing water level data at the gauge (40°47'17" N, 112°0'55" W) (<https://apps.geology.utah.gov/gwdp/>); National Climatic Data Center (NCDC), National Oceanic and Atmospheric Administration (NOAA) for providing meteorological data at gauges USW00024127, USC00427606 and USC00420820 (<https://www.ncdc.noaa.gov/cdo-web/datasets/>). Copernicus Sentinel-1A data can be obtained from European Space Agency (ESA) or Alaska Satellite Facility (ASF). ENVISAT ASAR data

were downloaded from ESA (cat-1 2853). This research was financially supported by NASA Earth and Space Science Fellowship (NNX15AN10H), NASA Surface and Interior Program (NNX16AL10G), and the Shuler-Foscue Endowment at Southern Methodist University. The maps were generated using General Mapping Tools (GMT) and ArcGIS.

REFERENCES

- Agram, P. S., R. Jolivet, B. Riel, Y. N. Lin, M. Simons, E. Hetland, M. P. Doin, and C. Lasserre (2013), New Radar Interferometric Time Series Analysis Toolbox Released, *Eos, Transactions American Geophysical Union*, 94, 69–70, doi:10.1002/2013EO070001.
- Agram, P. S., and M. Simons (2015), A noise model for InSAR time-series, *J. Geophys. Res. Solid Earth*, 2014JB011271, doi:10.1002/2014JB011271.
- Amelung, F., D. L. Galloway, J. W. Bell, H. A. Zebker, and R. J. Laczniaik (1999), Sensing the ups and downs of Las Vegas: InSAR reveals structural control of land subsidence and aquifer-system deformation, *Geology*, 27(6), 483–486, doi:10.1130/0091-7613.
- Arnow, T., and R. E. Mattick (1968), Thickness of valley fill in the Jordan Valley east of Great Salt Lake, Utah, in Geological Survey Research 1968, *U.S. Geol. Surv. Professional Paper 600-B*, B79-B82.
- Arnow, T., R. Van Horn, and R. LaPray (1970), The pre-Quaternary surface in the Jordan Valley, Utah, in Geological Survey Research 1970, *U.S. Geol. Surv. Professional Paper 700-D*, D257–D261.
- Barbot, S., J. Moore, and V. Lambert (2017), Displacement and stress associated with distributed an elastic deformation in a half-space, *Bulletin of the Seismological Society of America*, 107(2), 821–855.
- Bell, J. W., F. Amelung, A. R. Ramelli, and G. Blewitt (2002), Land subsidence in Las Vegas, Nevada, 1935-2000: New geodetic data show evolution, revised spatial patterns and reduced rates. *Environmental and Engineering Geoscience*, 8(3), 155–174, doi:10.2113/8.3.155.
- Berardino, P., G. Fornaro, R. Lanari, and E. Sansosti (2002), A new algorithm for ground deformation monitoring based on small baseline differential SAR interferograms, *IEEE Trans. Geosci. Remote Sens.*, 40(11), 2375–2383.
- Black, B. D., W. R. Lund, D. P. Schwartz, H. E. Gill, and B. H. Mayes (1996), Paleoseismology of Utah, volume 7-Paleoseismic investigation on the Salt Lake City segment of the Wasatch fault zone at the South Fork Dry Creek and Dry Gulch sites, Salt Lake County, Utah, *Utah Geol. Surv. Special Study* 92, 22.

- Burden, C. B., et al. (2000), Ground-water conditions in Utah, spring of 2000, *Utah Department of Natural Resources Division of Water Resources Cooperative Investigations Report Number 41*.
- Burden, C. B., et al. (2005), Ground-water conditions in Utah, spring of 2005, *Utah Department of Natural Resources Division of Water Resources Cooperative Investigations Report Number 46*.
- Burden, C. B., et al. (2010), Ground-water conditions in Utah, spring of 2010, *Utah Department of Natural Resources Division of Water Resources Cooperative Investigations Report Number 51*.
- Burden, C. B., et al. (2015), Ground-water conditions in Utah, spring of 2015, *Utah Department of Natural Resources Division of Water Resources Cooperative Investigations Report Number 56*.
- Casagrande, A., (1932), *The structure of clay and its importance in foundation engineering*, in contributions to Soil Mechanics 1925-1940, Boston Soc. Civ. Eng., 72–113.
- Casagrande, A., (1936), Determination of preconsolidation load and its practical significance, *Proc. 1st Conf. Soil Mech. and Found. Eng. (Vol. 3). Am. Soc. Civ. Eng.*, 60–64.
- Chaussard, E., R. Bürgmann, M. Shirzaei, E. J. Fielding, and B. Baker (2014), Predictability of hydraulic head changes and characterization of aquifer system and fault properties from InSAR-derived ground deformation, *J. Geophys. Res. Solid Earth*, 119, 6572–6590, doi:10.1002/2014JB011266.
- Chen, J., R. Knight, H. A. Zebker, and W. A. Schreüder (2016), Confined aquifer head measurements and storage properties in the San Luis Valley, Colorado, from spaceborne InSAR observations, *Water Resour. Res.*, 52, doi:10.1002/2015WR018466.
- Domenico, P. A., and M. D. Mifflin (1965), Water from Low-Permeability Sediments and Land Subsidence, *Water Resour. Res.*, 1(4), 563–567.
- Fattahi, H., P. Agram, and M. Simons (2017), A network-based enhanced spectral diversity approach for TOPS time-series analysis, *IEEE Trans. Geosci. Rem. Sens.*, 55, 777–786.
- Ferretti, A., C. Prati, and F. Rocca (2000), Nonlinear subsidence rate estimation using permanent scatterers in differential SAR interferometry, *IEEE Trans. Geosci. Rem. Sens.*, 38, 2202–2212.
- Ferretti, A., C. Prati, and F. Rocca (2001), Permanent scatterers in SAR interferometry, *IEEE Trans. Geosci. Remote Sens.*, 39(1), 8–20.

- Galloway, D., D. R. Jones, and S. E. Ingebritsen (1999), Land subsidence in the United States, *U.S. Geol. Surv. Circular 1182*.
- Hanson, R. T. (1989), Aquifer-system compaction, Tucson Basin and Avra Valley, Arizona, *U.S. Geol. Surv. Water-Resources Investigations* 88–4172.
- Hooper, A. (2008), A multi-temporal InSAR method incorporating both persistent scatterer and small baseline approaches, *Geophys. Res. Lett.*, 35, L16302, doi:10.1029/2008GL034654.
- Hooper, A. (2010), A statistical-cost approach to unwrapping the phase of InSAR time series, *European Space Agency Special Publication, ESA SP–677*.
- Hu, X., T. Wang, T. C. Pierson, Z. Lu, J. W. Kim, and T. H. Cecere (2016), Detecting seasonal landslide movement within the Cascade landslide complex (Washington) using time-series SAR imagery, *Remote Sens. Environ.*, 187, 49–61.
- Jiang, H., G. Feng, T. Wang, and R. Bürgmann (2017), Toward full exploitation of coherent and incoherent information in Sentinel-1 TOPS data for retrieving surface deformation: Application to the 2016 Kumamoto (Japan) earthquake, *Geophys. Res. Lett.*, 44, 1758–1767, doi:10.1002/2016GL072253.
- Jónsson, S., H. Zebker, P. Segall, and F. Amelung (2002), Fault slip distribution of the 1999 Mw 7.1 Hector Mine, California, Earthquake, estimated from satellite radar and GPS measurements, *Bulletin of the Seismological Society of America*, 92(4): 1377–1389, doi:10.1785/0120000922.
- Kim, J.-W., Z. Lu, Y. Jia, and C. K. Shum (2015), Ground subsidence in Tucson, Arizona, monitored by time-series analysis using multi-sensor InSAR datasets from 1993 to 2011, *ISPRS J. Photogramm. Remote Sens.*, 107, 126–141.
- Lay, T., and T. C. Wallace (1995), *Modern Global Seismology*, Academic Press, London, 521.
- Lu, Z., and W. Danskin (2001), InSAR analysis of natural recharge to define structure of a ground-water basin, San Bernardino, California, *Geophys. Res. Lett.*, 28(13), 2661–2664, doi:10.1029/2000GL012753.
- Lu, Z., and D. Dzurisin (2014), *InSAR Imaging of Aleutian Volcanoes: Monitoring a Volcanic Arc from Space*, Springer, 390.
- Lambert, P. M. (1995), Numerical simulation of ground-water flow in basin-fill material in Salt Lake Valley, Utah, *Utah Department of Natural Resources Technical Publication No. 110–B*, 58.

- Massonnet, D., and K. L. Feigl (1998), Radar interferometry and its application to changes in the Earth's surface, *Rev. Geophys.*, 36(4), 441–500.
- Mattick, R. E. (1970), Thickness of unconsolidated to semiconsolidated sediments in Jordan Valley, Utah, *U.S. Geol. Surv. Prof. Paper 700-C*, C119–C124.
- Miller, M. M., and M. Shirzaei (2015), Spatio-temporal characterization of land subsidence and uplift in Phoenix using InSAR time series and wavelet transforms, *J. Geophys. Res. Solid Earth*, 120, doi:10.1002/2015JB012017.
- Miller, M. M., M. Shirzaei, and D. Argus (2017), Aquifer mechanical properties and decelerated compaction in Tucson, Arizona, *J. Geophys. Res. Solid Earth*, 122, 8402–8416, doi:10.1002/2017JB014531.
- Mogi, K. (1958), Relations between the eruptions of various volcanoes and the deformations of the ground surfaces around them, *Bull. Earthquake. Res. Inst.*, 36, 99–134.
- Nelson, G. L. (1982), Vertical Movement of Ground Water Under the Merrill Field Landfill, Anchorage, Alaska, *U.S. Geol. Surv. Open-File Report 82*(1016).
- Neuman, S. P., and P. A. Witherspoon (1972), Field Determination of the Hydraulic Properties of Leaky Multiple Aquifer Systems, *Water Resour. Res.*, 8(5).
- Poland, J. F., and R. L. Ireland (1988), Land subsidence due to withdrawal of fluids, *Rev. Eng. Geol.*, 2, 187–269, 1969.
- Qu, F., Z. Lu, Q. Zhang, G. W. Bawden, J. W. Kim, C. Zhao, W. Qu (2015) Mapping ground deformation over Houston–Galveston, Texas using multi-temporal InSAR, *Remote Sens. Environ.*, 169, 290–306.
- Reeves, J. A., R. Knight, H. A. Zebker, P. K. Kitanidis, and W. A. Schreüder (2014), Estimating temporal changes in hydraulic head using InSAR data in the San Luis Valley, Colorado, *Water Resour. Res.*, 50, 4459–4473, doi:10.1002/2013WR014938.
- Reinisch, E. C., M. Cardiff, and K. L. Feigl (2016), Graph theory for analyzing pair-wise data: application to geophysical model parameters estimated from interferometric synthetic aperture radar data at Okmok volcano, Alaska, *J Geod.*, 1–16, doi:10.1007/s00190-016-0934-5.
- Riel, B., M. Simons, P. Agram, and Z. Zhan (2014), Detecting transient signals in geodetic time series using sparse estimation techniques, *J. Geophys. Res. Solid Earth*, 119, 5140–5160, doi:10.1002/2014JB011077.

- Riley, F. S. (1969), Analysis of borehole extensometer data from central California, *Int. Assoc. Sci. Hydrol. Publ.*, 89, 423–431.
- Saar, M.O., and M. Manga (2003), Seismicity induced by seasonal groundwater recharge at Mt. Hood, Oregon, *Earth Planet. Sci. Lett.*, 214, 605–618.
- Schmidt, D. A., and R. Bürgmann (2003), Time-dependent land uplift and subsidence in the Santa Clara valley, California, from a large interferometric Synthetic Aperture Radar data set, *J. Geophys. Res.*, 108, 2416, doi:10.1029/2002JB002267, B9.
- Segall, P., J. Grasso, and A. Mossop (1994), Poroelastic stressing and induced seismicity near the Lacq gas field, Southwestern France, *J. Geophys. Res.*, 99.
- Shirzaei, Manoochehr, Ellsworth, W. L., Tiampo, Kristy F., González, P. J., and Manga, M. (2016), Surface uplift and time-dependent seismic hazard due to fluid injection in eastern Texas, *Science*, 353, 1416, doi: 10.1126/science.aag0262
- Shirzaei, M., R. Bürgmann, and E. J. Fielding (2017), Applicability of Sentinel-1 Terrain Observation by Progressive Scans multitemporal interferometry for monitoring slow ground motions in the San Francisco Bay Area, *Geophys. Res. Lett.*, 44(6), 2733–2742, doi:10.1002/2017GL072663.
- Sneed, M. (2001), Hydraulic and mechanical properties affecting ground-water flow and aquifer system compaction, San Joaquin Valley, California, *U.S. Geol. Surv. Open File Report 1*(35).
- Sneed, M., J. W. Borchers, R. E. Kayen, B. A. Carlin, K. M. Ellett, G. A. Wheeler, and T. M. Brocher (2007), Hydromechanical response characterization by integration of geophysical and hydrological data, San Lorenzo, California, *AGU Fall Meeting, Abstracts*, J23A-1007.
- Snyder, N. P., and M. Lowe (1998), Map of recharge areas for the principal valley-fill aquifer, Ogden Valley, Weber County, Utah, *Utah Geological Survey Map 176*, 16, scale 1:75,000.
- Starn, J. J., A. C. Bagtzoglou, and C. T. Green (2015), The effects of numerical-model complexity and observation type on estimated porosity values, *Hydrogeology Journal*, 23(6), 1121–1128, doi:10.1007/s10040-015-1289-3.
- Thiros, S. A. (2003), Hydrogeology of Shallow Basin-Fill Deposits in Areas of Salt Lake Valley, Salt Lake County, Utah, *U.S. Geol. Surv. Water-Resources Investigations Report 03-4029*.
- Thiros, S. A., L. M. Bexfield, D. W. Anning, J. M. Huntington (2010), Section 2.-Conceptual Understanding and Groundwater Quality of Selected Basin-fill Aquifers in the Southwestern United States, *U.S. Geol. Professional Paper 1781*.

USGS (2016), New Report Forecasts the High Likelihood of Damaging Earthquakes During the Lifetime of Many Utah Residents, released: 4/18/2016 4:35:43 PM, access April 21, 2016 at <http://www.usgs.gov/newsroom/article.asp?ID=4511#.VxlbL7Qfc22>

Wallace, J., and M. Lowe (2009), Ground-water quality classification for the principal basin-fill aquifer, Salt Lake Valley, Salt Lake County, Utah, *Utah Geol. Surv., Open File Report 560*.

CHAPTER 4

CONSOLIDATION SETTLEMENT OF SALT LAKE COUNTY TAILINGS

IMPOUNDMENT

Hu, X., T. Oommen, Z. Lu, T. Wang, J. W. Kim, 2017, Consolidation settlement of Salt Lake County tailings impoundment revealed by time-series InSAR observations from multiple radar satellites, *Remote Sens. Environ.*, 202, 199-209.

4.1 Introduction

Tailings impoundments/dams are built to accommodate the byproducts of mining operations after the separation of the valuable metals/minerals and the fine-grained waste (tailings), and they can usually be found at or near mine sites [Hudson-Edwards, 2016]. Since the mining industry produces enormous quantities of fine rock particles, ranging from a few millimeters down to as small as a few microns, the tailings embankment can reach several hundred meters in height and the impoundments can cover several square kilometers spatially [U.S. EPA, 1994]. Failures of tailings dams occur worldwide [e.g., Caldwell and Charlebois, 2010], with substantial triggering factors including, but not limited to, earthquakes, foundation/slope failures, liquefaction, and overloading. A catastrophic tailings dam failure can have significant fatal, environmental, and financial consequences [Hudson-Edwards, 2016]. The recent large collapse of mines and tailings dams in Hpakant, Kachin state, Myanmar on November 21, 2015 killed at least 113 people [WISE, 2015]. These failures also contaminated the ground surface and groundwater with metals, and a large scale contamination can cost an average of \$500 million to cleanup [Bowker and Chambers,

2015]. The safety of tailings facilities, for protecting life, environment, and property, is crucial to today's mining operations [ICOLD, 2001]. Therefore, monitoring the stability of tailings impoundment is critical for sustainable mining development. However, the overwhelming spatial extent of the tailings impoundment often proves to be an engineering challenge to monitoring using traditional geotechnical measurement techniques.

InSAR provides an excellent monitoring tool to evaluate the stability of man-made structures, such as tailings dams [e.g., Riedmann et al., 2013; Colombo, 2013; Necsoiu and Walter, 2015], by providing mm-scale deformation measurements with bi-weekly or monthly updates. The rate of settlement and its spatial distribution derived by InSAR can help determine if the desired consolidation is reached, if additional drainage needs to be performed, and where the drainage wells should be installed. It also can provide indications of any differential settlement occurring within the impoundment. However, recent InSAR studies on tailings impoundment in South Africa [Riedmann et al., 2013], Chile [Colombo, 2013], and New Mexico (USA) [Necsoiu and Walter, 2015] have mainly focused on the dams' slope stability, but their geotechnical mechanism, potential impacts to the surrounding area, and correlation with the hydrological processes have been less investigated [Riedmann et al., 2013; Colombo, 2013]. These analyses were limited by the availability of archived SAR images (e.g., short temporal period) and lacked validation [Necsoiu and Walter, 2015].

The study presented here is the first that uses a combination of multi-temporal and multi-spaceborne SAR observations, DEMs from SRTM and high-resolution LiDAR, and auxiliary water level data, to assess the stability of the Kennecott tailings impoundment in Salt Lake County, Utah, and the surrounding area. A set of 40 descending C-band ENVISAT ASAR images from Track 41 (T41) during 2004-2010, 13 ascending L-band ALOS PALSAR-1 fine beam mode

images from Path 202 (P202) during 2007-2011, and 18 descending C-band Sentinel-1A interferometric wide-swath (IW) images from Path 158 (P158, half of the imaging swath) during 2015-2016 were used (Figure 4.1a). Utilizing a large dataset of SAR images can: a) improve the accuracy of deformation measurement through multi-interferogram processing by reducing various artifacts in individual interferograms; b) enhance the temporal resolution of the time-series products; c) allow for the retrieval of 2-dimensional (or even 3-dimensional) deformation vectors; and d) expand the time span of the investigation to better understand the long-term characteristics of the phenomenon (e.g., Lu and Dzurisin, 2014). The multi-temporal InSAR method assesses the stability of the embankments through mapping out drastic and gradually decelerated subsidence over the south pond, and various deformation behavior over the surrounding infrastructures and land disposal sites. InSAR-derived deformation is also compared with daily water level data. I show that InSAR observations can be well-explained by a consolidation settlement model, which allows us to differentiate the settlement process and foresee its development in the near future.

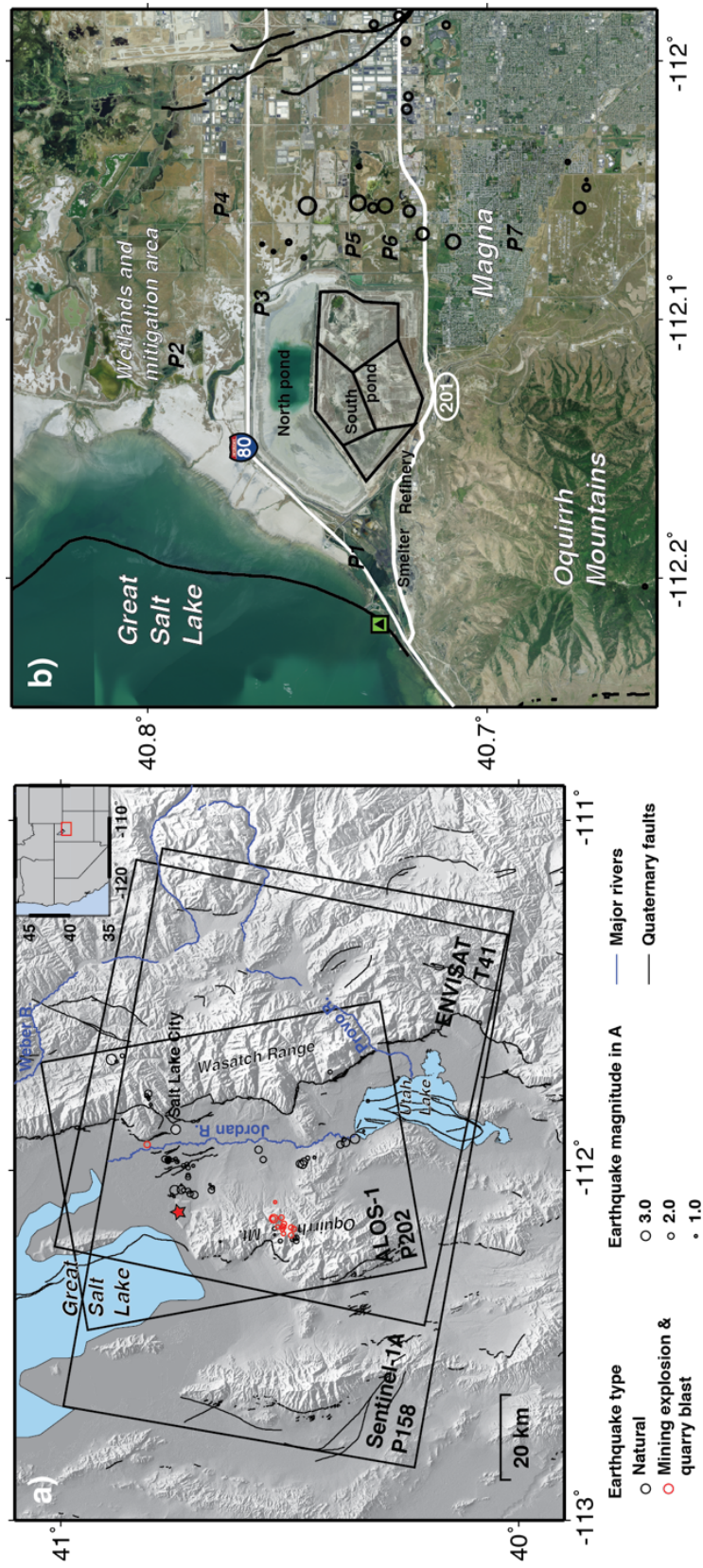


Figure 4.1 Geographic maps of the tailings impoundment. (a) Coverage of radar data tracks (black squares) superimposed on the shaded relief map over Salt Lake Valley, Utah. Black lines show the Quaternary faults and blue lines represent major rivers and streams. Circles indicate locations of earthquakes occurred in recent decade, in which black ones are tectonic earthquakes and red ones (concentrated at the Bingham Canyon mine) are caused by mining explosion and/or quarry blast. Earthquake magnitudes are proportional to the size of the circles. Tailings impoundment, denoted with the star, locates in the vicinity of the Great Salt Lake. (b) Aerial imagery of the tailings impoundment bounded by the Great Salt Lake to the northwest, wetlands and mitigation area to the northeast, Oquirrh Mountains to the southwest, and residential community Magna to the southeast. The whole impoundment can be classified into two major ponds – the north pond with active tailings deposition and the south pond which has been completely abandoned and reclaimed since 2001. The south pond can be further divided into four reclamation areas by the ditches (visible from the aerial images and LiDAR DEM shade relief map), and they are outlined by black polygons. Interstate Hwy I-80 and state Hwy 201 are delineated with white lines. The water gage at Saltair Boat Harbor is marked with the triangle inside the green square near the intersection of Hwys I-80 and 201. Same symbols are used in the other figures in this paper.

4.2 Study area and related hazards

The east flank of Oquirrh Mountains at Salt Lake Valley, Utah, accommodates the Bingham Canyon mine managed by Kennecott Utah Copper Company and contributes a quarter of total US copper production. Tertiary-age igneous rocks intruded the Oquirrh Formation, forming deposits of copper and other metals that have been extracted from a depth of more than 970 meters [Pankow et al., 2014]. About 20 km north of the Bingham Canyon mine, Kennecott built a 37-km² tailings impoundment to contain its uneconomic ore products, which has been in operation since 1906. Tailings in the impoundment are primarily composed of silica sand, with a slightly higher concentration of copper than the general soil in the western United States [Kennecott Utah Copper, 2008].

Kennecott tailings impoundment, together with a mining refinery and a smelter, are in close proximity to the Great Salt Lake (Figure 4.1b). The tailings show a downward hydraulic gradient, equal to an average of 40% hydrostatic pressure [Klohn Leonoff, 1992]. The aquifer systems around the impoundment have concentrations of arsenic, selenium, and cadmium in excess of Utah Ground Water Quality Standards [Kennecott Utah Copper, 2011]. Currently, there is increasing public awareness of the extensive groundwater contamination and air pollution from mining production, and their impact to the fish and wildlife habitats in the Great Salt Lake and the residential community of Magna [EARTHWORKS, 2011].

Another big concern is the stability of the facility and the associated risk to public safety due to a potential earthquake induced failure [URS, 1999a; URS, 1999b; Tetra Tech, Inc., 2009]. Kennecott tailings impoundment has experienced failures in 1941, 1964 and 1998 [Kennecott Utah Copper, 1997; AGRA Earth and Environmental, Inc., 1998]. The deposition of fine particle tailings became fluid due to water intrusion, resulting in embankment failure. The impoundment is located

between the East Great Salt Lake fault zone to the west and the extended fault segments of the Wasatch fault system to the east [EERI, 2015]. Figure 4.1b illustrates the tectonic earthquakes in this valley mainly occurred at the terrain adjacent to tailings dams. The fluid pressure change in and around the settling impoundment may vary the stress field and trigger the seismicity [Amos et al., 2014], which in turn, may induce liquefaction and the associated dam failure and runout event.

To upgrade the stabilization of the old south pond in the vicinity of Magna community, Kennecott began reducing the slope of the southeast corner and moved the tailings more than 800 m away from the slope crest in the early 1990s [Kennecott Utah Copper, 2008]. In 1995, Kennecott added an adjacent 14-km² north pond with seismic upgrade, and later in 1999, began transitioning from the south pond to the north pond [Kennecott Utah Copper, 2008] (Figure 4.1). Kennecott actively managed the suppression of dust at the north pond by keeping the center (where fine grain tailings are deposited) wet with tailings slurry and watering the outer embankments [UDEQ and EPA, 2014]. After terminating the tailings deposition on the south pond completely in 2001, Kennecott reclaimed the area by vegetating the slopes and top surface, which included a series of implementations of dewatering [UDEQ and EPA, 2014]. Around the perimeter of the impoundment, clarification canal and toe drains have been constructed to collect the water. A sedimentation pond (P5 in Figure 4.1b) to the east side of the south pond was used for further clarification of the drain-down water to reduce total suspended solids before directing the water to the process circuit [Kennecott Utah Copper, 2011]. Kennecott has spent over \$500 million dollars in the past 20 years to upgrade the stability of the south tailings facility, and recently launched another \$2 million pilot dewatering project to accelerate the stabilization process, which included the installation of more wells for water pumping [Kennecott Utah Copper, 2016].

Even though enormous efforts have been put forth to mitigate the risk of failure [Kennecott Utah Copper, 1997; EARTHWORKS, 2011], there were no geodetic measurements to systematically monitor the settlement of tailings and the stability of the surrounding area. Persistent consolidation settlement due to the dissipation of pore pressure and the associated increase in effective stress during water drainage and extraction may pose a threat to the surrounding infrastructures, including a major railway line, Interstate Hwy I-80 and State Hwy 201 (Figure 4.1). It is especially thus important to monitor the stability of the impoundment area in this tectonically active region. Utah Department of Environmental Quality (UDEQ) and Environmental Protection Agency (EPA) claimed that the south pond, the outer embankments of the north pond, and the surface soils along the south side of Hwy 201 appeared to be stable in their recent five-year review [2014]. However, the statement needs to be thoroughly investigated by long-term observations.

4.3 Multi-temporal InSAR analysis

I employ a multi-temporal InSAR data processing routine to derive the displacement field after removing the atmospheric phase screen and orbital artifacts inherent in each interferogram [e.g., Hu et al., 2016]. The topographic phase component in the interferograms is estimated using 2-m resolution bare-earth LiDAR DEM acquired in 2006. A total number of 105 ENVISAT ASAR interferograms (perpendicular baseline $< \sim 300$ m and temporal interval $< \sim 450$ days), 23 ALOS PALSAR-1 interferograms (perpendicular baseline $< \sim 2,000$ m and temporal interval $< \sim 600$ days), and 66 Sentinel-1A interferograms (perpendicular baseline $< \sim 250$ m and temporal interval $< \sim 180$ days) are used for time-series analysis. Figure 4.2 shows the baseline configurations for these three datasets.

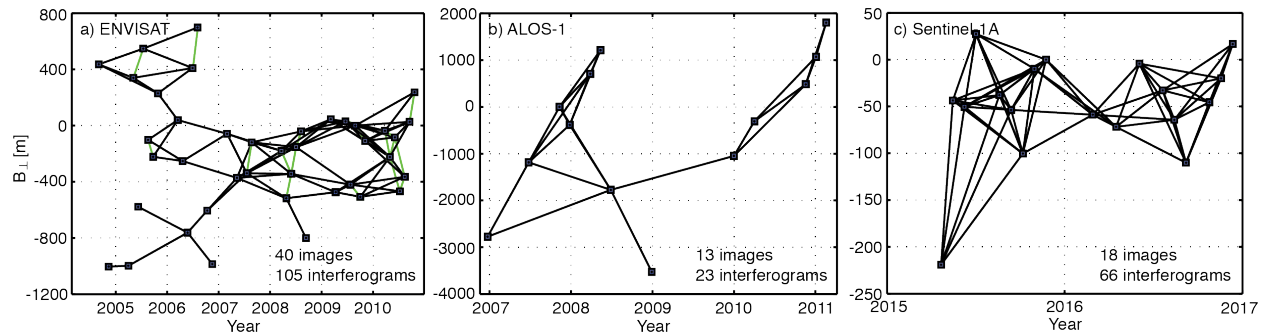


Figure 4.2 Image graph of the interferometric pairs: ENVISAT (a), ALOS-1 (b) and Sentinel-1A (c) datasets. All connecting lines indicate the interferograms used to retrieve the time-series deformation, in which the green lines in panel a represent the interferograms used to estimate the dominant deforming trend at the south pond.

I jointly use the DA and averaged coherence to identify PS [Ferretti et al., 2000] or CT points [Hu et al., 2016]. The north pond completely loses coherence due to the moist surface for the purpose of enhanced dust control, and thus no CT point can be detected. The south pond has been reclaimed and well-vegetated at the surface and thus allows the identification of CT points. Although the south pond is no longer active for tailings deposition, it is still valuable to evaluate Kennecott's commitment of reclamation and stabilization efforts, especially when the tailings may still have the potential to liquefy in this tectonically active region. The available ENVISAT and Sentinel-1A images are sufficiently large in number, and thus I exclude the data acquired during the winter season from December to February when the coherence is poor. Nevertheless, the available ALOS-1 images are limited, so I include all data running through different seasons. The south pond has been kept wet for the purpose of dust control, which means that the top layer is frozen in the winter so that SAR amplitudes are highly variable in time. Therefore, the DA of ALOS-1 over the south pond is significantly larger than that of the other two datasets, and its detected CT points at the south pond are more sparse than the surrounding area at given DA threshold. The disparity in density is less obvious for ENVISAT dataset and almost nonexistent for Sentinel-1A dataset. To achieve a general density equilibrium of CT points between the south

pond and the surrounding areas for ENVISAT and ALOS-1 datasets, I first applied ordinary thresholds ($DA < 0.5$ and averaged coherence > 0.35 for ENVISAT dataset, and $DA < 0.4$ and averaged coherence > 0.5 for ALOS-1 dataset) to obtain the initial CT points in the study area (Figures 4.3a and d), and then loosen the thresholds ($DA < 1$ and averaged coherence > 0.32 for ENVISAT dataset, and $DA < 1$ and averaged coherence > 0.4 for ALOS-1 dataset) to densify CT points within the south pond (Figures 4.3b and e). A merge of these two constitutes the ultimate CT points (Figures 4.3c and f) used for time-series analysis. Sentinel-1A images are regularly acquired over this study site with about a 24-day interval (the satellite repeat cycle is 12 days), leading to much larger coherence and smaller DA, and I use the same thresholds ($DA < 0.45$ and averaged coherence > 0.5) for the entire study area. The resultant averaged density is 1,200, 1,600 and 1,350 CT points per km^2 for ENVISAT, ALOS-1 and Sentinel-1A datasets, respectively.

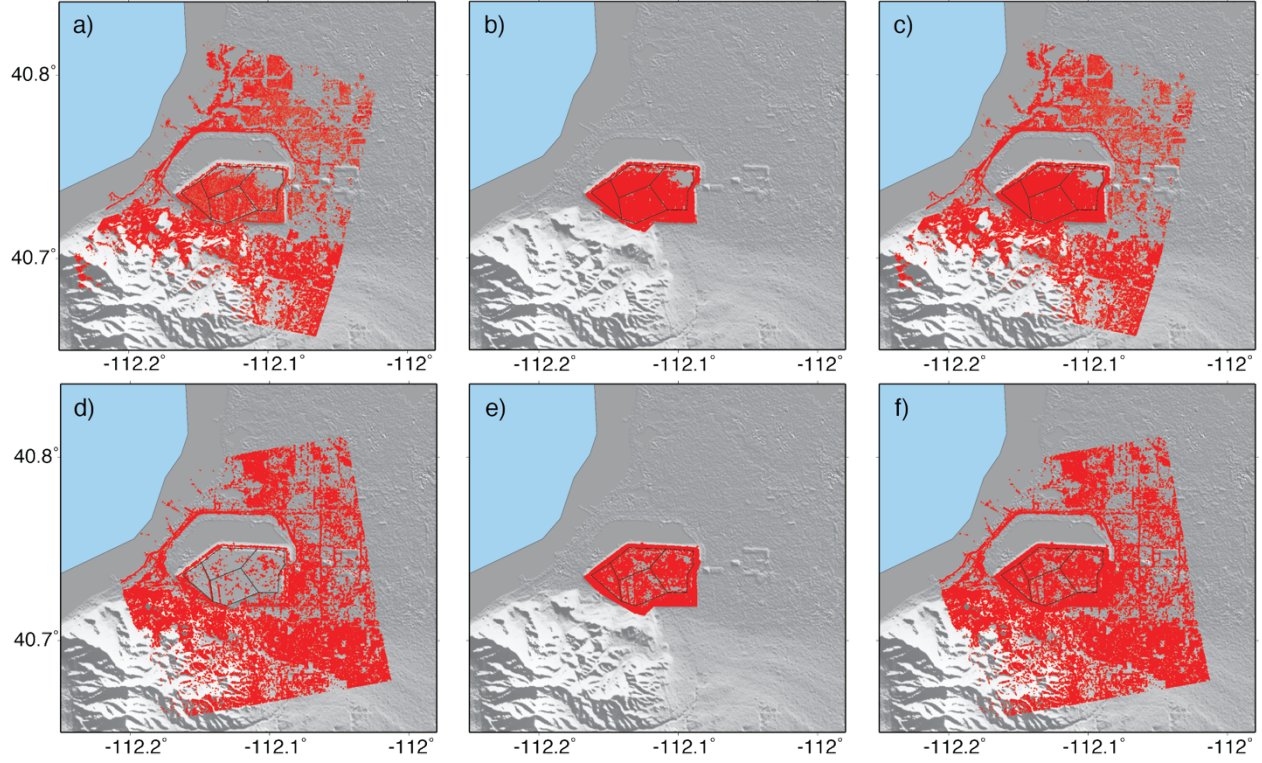


Figure 4.3 CT points selection for ENVISAT (a-c) and ALOS-1 (d-f) datasets. (a) and (d) show the initial CT points detected in the study area, (b) and (e) show the densified CT points in the south pond by loosening the thresholds, and (c) and (f) show the ultimate CT points used in time-series analysis by merging CT points in (a), (b) and (d), (e), respectively.

As the study area is adjacent to the Great Salt Lake at the foot of Oquirrh Mountains, water vapor - in the air above the site - can produce artifacts in interferograms. Considered as low frequency signals in space, atmospheric artifacts and satellite orbital errors are estimated by first-order polynomial fitting with respect to the range and azimuth position in radar coordinates as well as the elevation at the location of CT points. The actively moving south pond and poorly coherent mountainous areas are masked out when constraining the polynomial coefficients.

The deformation gradient in the tailings impoundment based on initial interferograms is too large for the C-band ENVISAT dataset to be correctly unwrapped. To resolve the heavily condensed fringes in terms of interferograms, I first estimated the linear deformation velocity using 19 interferograms with stringent baseline thresholds (perpendicular baseline $< \sim 300$ m and

temporal interval $< \sim 90$ days, green connecting lines in Figure 4.2a). The velocities for each CT point are further used to estimate the dominant deformation component, which is removed from the original wrapped phase for all the selected 105 interferogram. As a result, the fringes of the interferograms are greatly reduced which allows for correct phase unwrapping. Subsequently, the dominant deformation component is added back. This process is run iteratively, and the dominant deformation component is re-estimated from each iteration. In the study, two iterations are good enough to eliminate the phase jumps. The resultant 105 unwrapped interferograms are used to retrieve the time-series deformation at each CT point using LSE (e.g., Hu et al., 2016). Although Sentinel-1A dataset is also operated in the C-band, the temporal frequency (~ 9 acquisitions per year used in this study) is improved over ENVISAT (~ 6 acquisitions per year), so I have a sufficient number of interferograms with clearly distinguishable fringes and avoids the unwrapping problem.

4.4 Data analysis and interpretation

Assuming that there is no north-south movement on the south pond, I derive the 2D (vertical and east-west) displacement field (Figure 4.4) using the temporally overlapping measurements of ENVISAT and ALOS-1. The ground surface shows significant land subsidence, reaching a rate of 200+ mm/yr at the northeast corner; which is a representation of the vertical settlement of the tailings impoundment during dewatering. Interestingly, the horizontal displacement map shows that the west and east motion of the south pond moves toward the center, though at a much smaller magnitude (< 30 mm/yr). This might be due to the possible surface motion of the south pond towards the central north pond (greenish surface area in Figure 4.1b) that is currently in active tailings deposition. Considering the tailings fields are governed by the vertical motion, I retrieve

the vertical deformation by projecting the radar line-of-sight (LOS) deformation with the local incidence angle at each CT point in the following analysis.

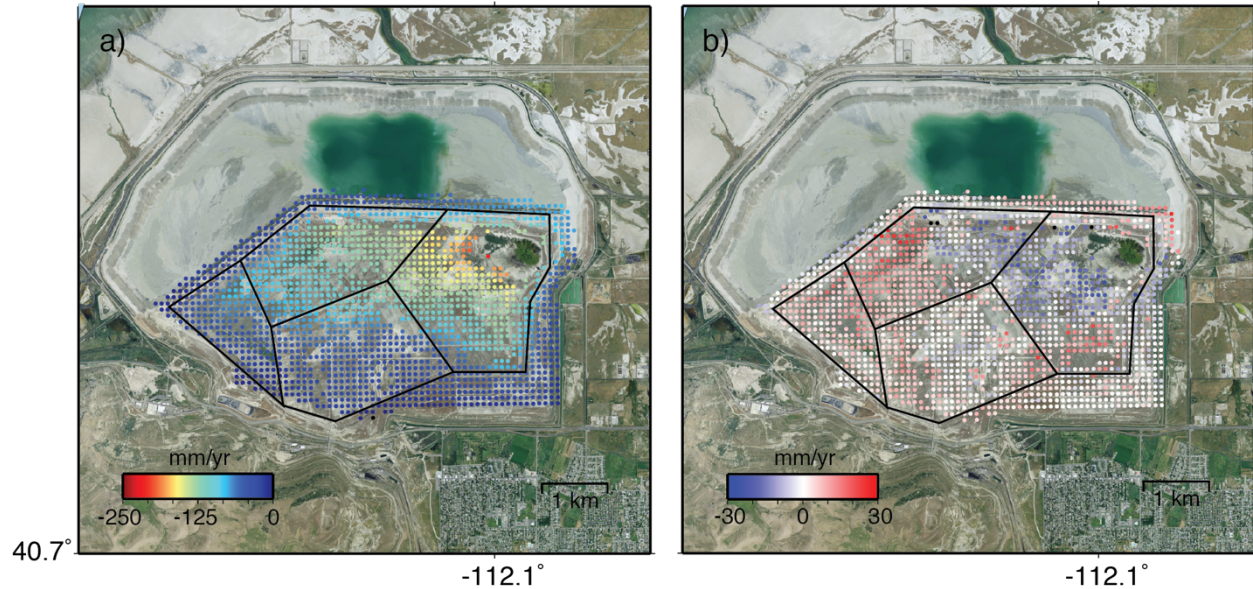


Figure 4.4 2D annual displacement (assuming no north-south movement) field of the south pond derived by ENVISAT and ALOS-1 measurements of overlapping period between 2007 and 2010. (a) Vertical displacement field. Negative values mean subsidence. (b) Horizontal east-west displacement field. Positive values mean eastward motion and negative values mean westward motion.

4.4.1 Drastic settlement of the south pond

The vertical deformation velocity of the study area (Figures 4.5a-c) and the deformation velocity measurements along two profiles AA' and BB' (Figures 4.5d-e, for CT points within a buffer of 100 m) suggest that the settlement has gradually decelerated throughout the entire south pond. Three independent InSAR datasets show good consistency with the compaction peak located at the northeast corner at a rate of 200+ mm/yr during 2004-2011 and 100+ mm/yr during 2015-2016; the adjacent toe of the north slope just west of the northeast corner is where the statically-induced flow liquefaction slide occurred in 1998 [AGRA Earth and Environmental, Inc., 1998]. The settlement seems to be well constrained by the peripheral embankments. Although the time span of Sentinel-1A imagery is only about two years, the temporal resolution is high enough to

maintain good coherence, so the averaged velocity map can pinpoint the location of the compaction peak, where ENVISAT and ALOS-1 datasets failed due to the scarcity of CT points. In addition to the drastic subsidence, the entrapped water over the fine-grained tailings is another explanation for the scarcity of CT points at this location. The water used in the slurry transport of tailings on the south pond has been collected in a decant pond in the near vicinity of the northeast corner since 1917 [Dunne et al., 1999].

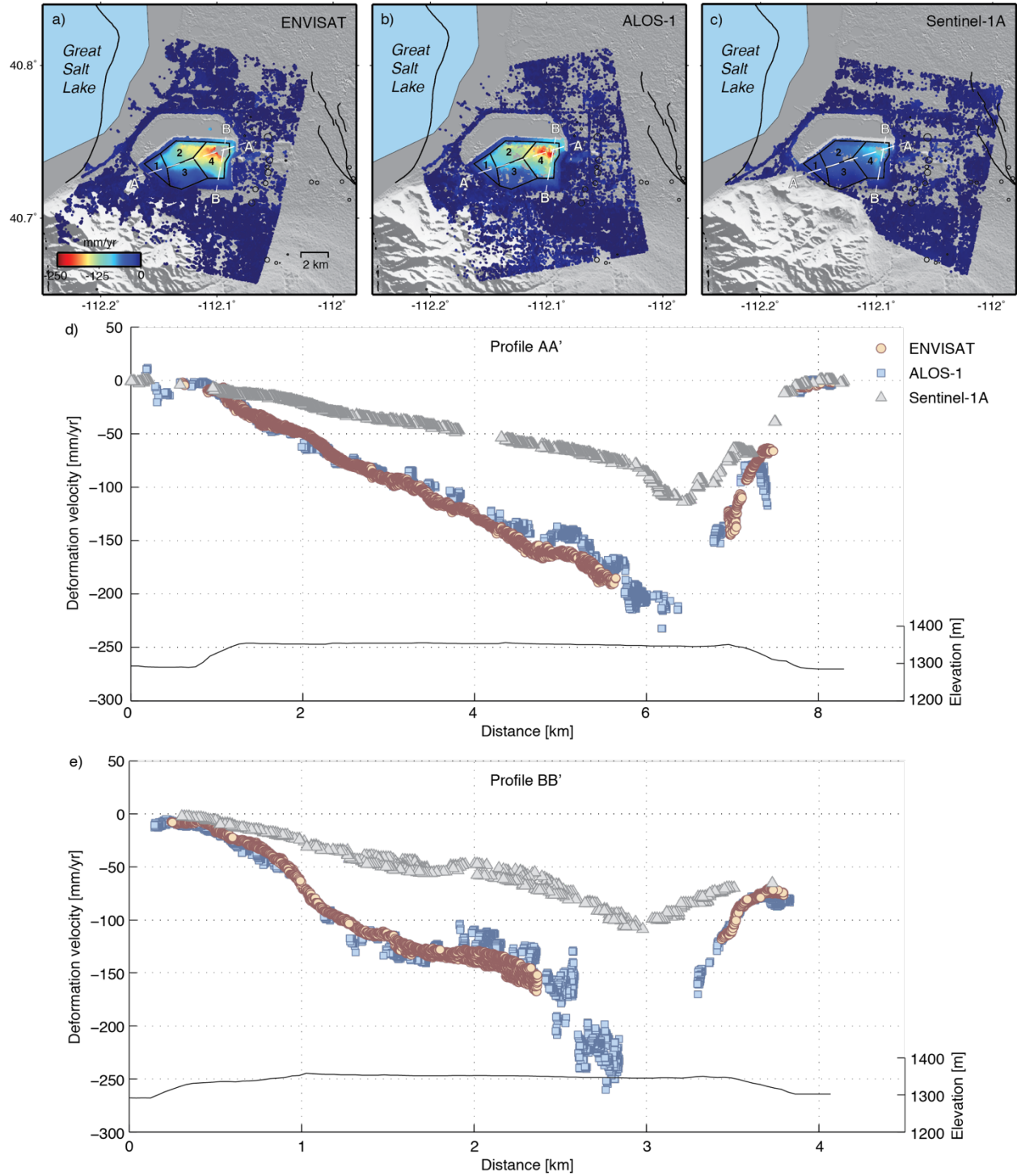


Figure 4.5 Vertical deformation velocity in the south pond derived from ENVISAT (a), ALOS-1 (b) and Sentinel-1A (c) datasets. (d) and (e) show the deformation velocities of ENVISAT (red circles), ALOS-1 (blue squares), and Sentinel-1A (gray triangles) along cross-section profiles AA' and BB' (white dashed lines). The left Y axis represents the vertical deformation velocity in millimeters per year and the right Y axis represents the elevation in meters.

The 2006 LiDAR DEM, 2000 SRTM DEM and their difference over the study area are shown in Figures 4.6a-c. According to the DEM map, the impoundment areas are significantly higher (approximately 65 m) than the surrounding ground, consistent with the investigation conducted by the UDEQ and EPA [2014]. Additionally, the embankments confining the pond along the interstate Hwy I-80, and the tapered earthen berms next to the Magna neighborhood are also visible from the DEM difference map, suggesting they were built between 2000 and 2006: a linear structure with around 20-m increase of height along I-80 highlights the upgrade and construction of the embankments during this time period, and the linear features with more than 10-m decrease of height at the southeast corner probably correspond to the ditches bounded the tapered earthen berms (approximately 4.5 m in height) [Kennecott Utah Copper, 2008]. More importantly, the DEM difference map provides additional evidence of the emplacement of the compaction peak (Figures 4.6d and e). InSAR and DEM estimates are in good agreement that the compaction peak locations at 6.5 km along profile AA' (from A) and 3.05 km along profile BB' (from B).

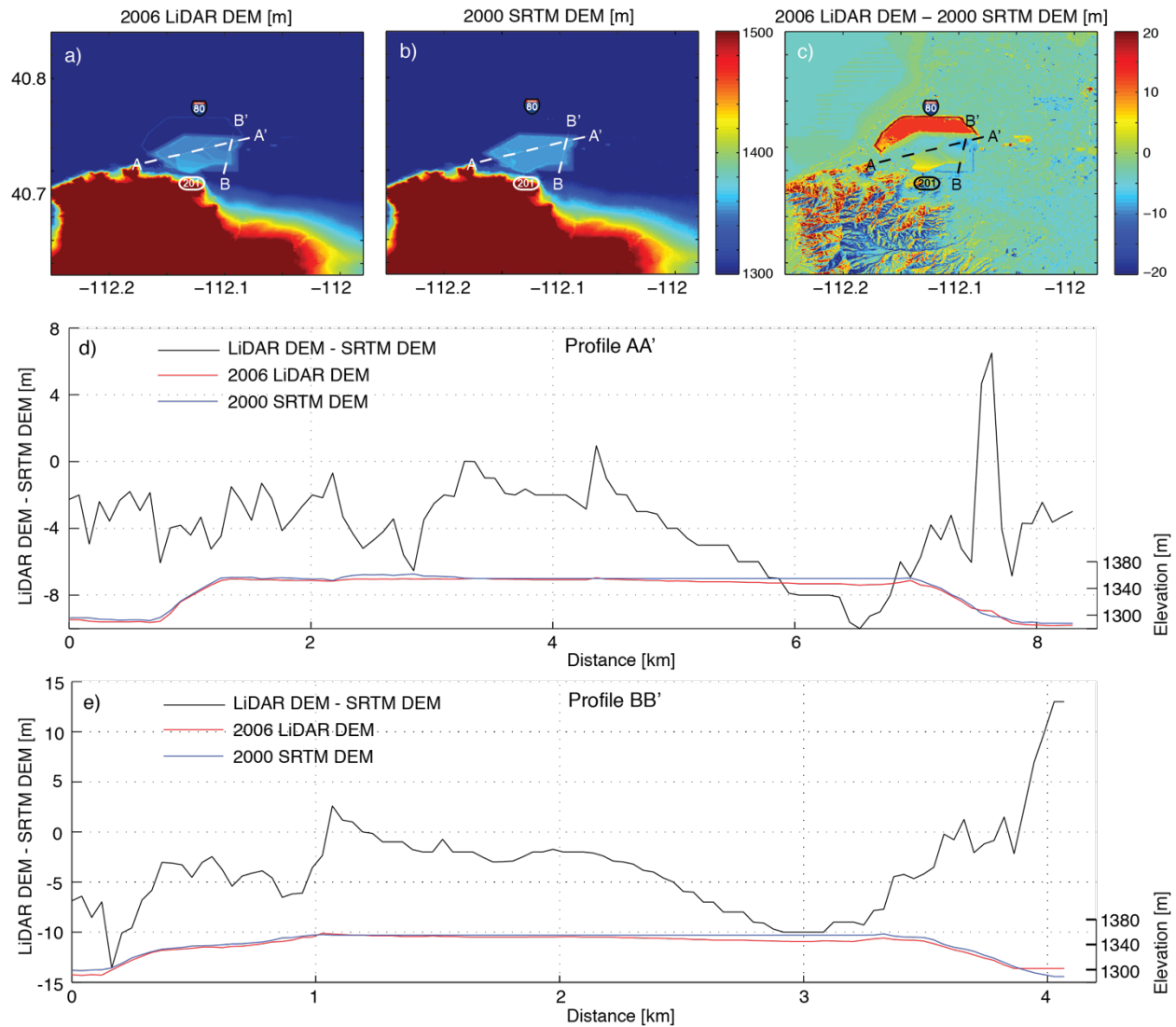


Figure 4.6 DEM of the pond area: 2006 bare-earth LiDAR DEM (a), 2000 SRTM DEM (b), and the difference between those two (c). (d) and (e) show the elevation and their difference along profiles AA' and BB' respectively.

The south pond was subdivided into some reclamation areas, and these areas were reclaimed in a systematic and sequential manner, while tailings continue to be deposited into the unreclaimed areas [URS, 1999a]. A series of reclamation dikes constructed across the surface of the impoundment isolate each of the reclamation areas and allow us to delineate the major reclamation areas (polygons outlined by black lines in Figures 4.1b, 4.3, 4.4, and 4.5a-c) according to the shaded relief map of LiDAR DEM and aerial imagery.

To better analyze the deformation patterns, I calculated the averaged cumulative deformation of each reclamation area. Figure 4.7 shows that the least subsidence is observed at reclamation areas 1 and 3 to the west and south, with more than twice the magnitude of deformation found at reclamation areas 2 and 4 to the north and east. The cumulative deformation from ALOS-1 is slightly larger than that from ENVISAT, which is more outstanding in reclamation area 4. This is because the density of CT points over the subsiding northeast corner is larger in ALOS-1 than in ENVISAT, so more significant values are included when taking the average. Another reason for the difference between ENVISAT and ALOS-1 estimates might be due to possible horizontal displacements because of the descending track from ENVISAT and the ascending track from ALOS-1 have different sensitivities to horizontal motions. Nevertheless, the difference in the cumulative deformation is small and can be ignored with respect to the total. Time-series deformation (Figure 4.7) also suggests that the settlement has been decaying. Take the reclamation area 4 for example, Sentinel-1A results depict a cumulative averaged subsidence of almost 100 mm in less than two years from April 2015, indicative of a settling rate of ~ 50 mm/yr, around one quarter of that in previous years from 2004 through 2011 (an average of ~ 130 mm/yr as derived from ENVISAT and ALOS-1 results). I believe a couple of outliers in the time series are due to the localized atmospheric turbulence associated with the corresponding acquisitions.

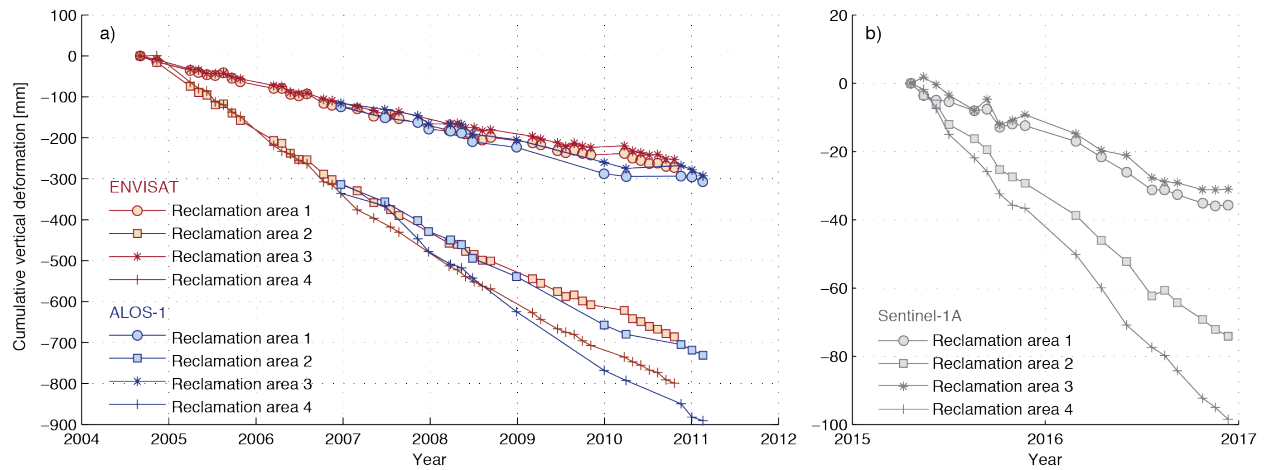


Figure 4.7 Quasi-linear cumulative deformation of four reclamation areas within the south pond. Circles, squares, asterisks and crosses represent the results of reclamation areas 1 to 4, respectively. Red and blue annotations in panel a and gray annotations in panel b represent the measurements of ENVISAT, ALOS-1 and Sentinel-1A, respectively.

4.4.2 Stability of the embankments and surrounding area

The settlement in the tailings impoundment and the accompanying drastic surface subsidence may have an impact on the stability of the embankments and surrounding area, underlain by the low permeability Upper Bonneville Clay. Based on multi-temporal InSAR results, I have found the northeast embankments of the south pond are in active motion (Figure 4.8). Some long-term net subsiding sites can also be located: two segments along the Hwy I-80 (P1 and P3) and two wetlands and mitigation sites (P2 and P4), and the sedimentation pond (P5) and the land disposal site (P6). In contrast to the decaying settlement of the south pond, most of the highlighted sites seem to maintain the same level of deformation velocity through time. One segment of Hwy 201 adjacent to the embankments at the southeast corner experiences relatively subtle subsidence (~ 20 mm/yr), far less than that of the south pond, and the deformation boundary has retreated from the residential community of Magna according to the recent Sentinel-1A results.

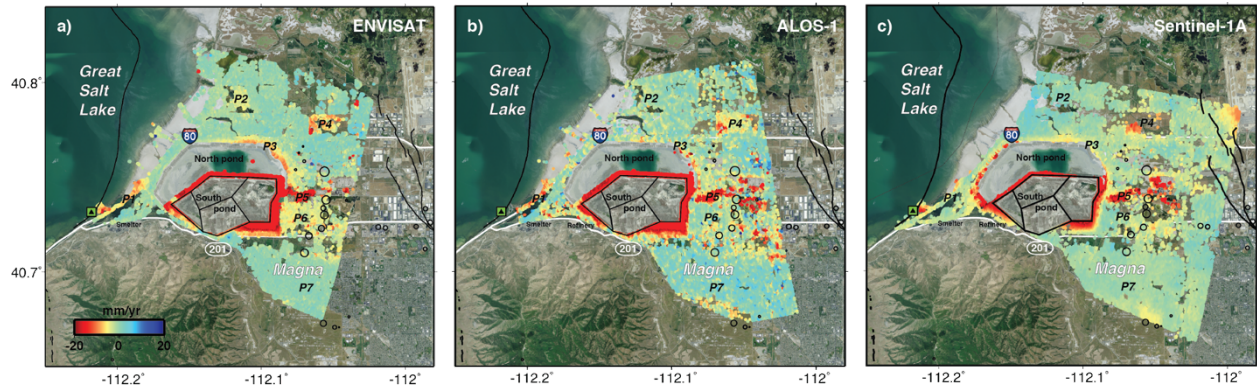


Figure 4.8 Vertical deformation velocity surrounding the tailings impoundment derived from ENVISAT (a), ALOS-1 (b) and Sentinel-1A (c) datasets, respectively. The drastic settlement of south pond and the poorly coherent mountainous areas in the southwest of the study area are masked out so that I can highlight on the area of interest with a narrow range of color scale.

To better interpret the behavior of the occurring deformation, I plot the time-series deformation at selected sites, and also compare them with the daily water level measurements at Saltair Boat Harbor in the vicinity of the Great Salt Lake (green square in Figures 4.1b and 4.8). The sedimentation pond P5 (Figure 4.9e) shows quasi-linear subsidence, which is similar to the south pond (Figure 4.7). Interestingly, the subsidence of P5 is at the same rate of decaying with respect to the settlement over the south pond. To be specific, the rate of subsidence of P5 has decreased from ~ 25 mm/yr during 2004-2011 to ~ 10 mm/yr during 2015-2016, similar to the decaying settling process (by around 60 percent) of the adjacent reclamation area 4 from ~ 130 mm/yr to ~ 50 mm/yr. Therefore, I suggest that the subsidence of P5 is highly likely due to the settlement effect extending from the south pond. About 3 km northeast to the impoundment, site P4 (Figure 4.9d) seems to maintain a quasi-linear subsidence at a rate of 7 to 10 mm/yr. Site P7 (Figure 4.9g) at Magna shows fluctuations in displacement, but the net elastic deformation is almost zero. The other selected sites, including the Hwy I-80 segments P1 (Figure 4.9a) and P3 (Figure 4.9c), wetlands and mitigation site P2 (Figure 4.9b), and the land disposal site P6 (Figure 4.9f), exhibit net cumulative subsidence up to 60 mm with larger fluctuations from 2004 to 2011. The water

level follows the seasonal trend, reaching a peak in the late spring and then dropping to the bottom in the early winter, with an annual peak-to-trough magnitude of less than 1 m. The time-series deformation at P6, particularly for Sentinel-1A results, seems to be in phase with water levels, possibly suggesting an elastic response of the ground surface to the pore pressure change; however, no similar comparisons at other sites (e.g., P1-P5) can be found closer to the water level gage. Therefore, there is no clear evidence for correlation between deformation fluctuation and seasonal water level in this study site.

I believe that the embankments do constrain the compaction of the impoundment to a large extent, but there are still some “leakages” that have occurred. Based on the observations, I make the following recommendations: (a) stabilization of embankments along the east half side of the impoundment; (b) monitoring of the tailings-related process near the water gage at Saltair Boat Harbor and the sedimentation pond around P5; (c) reinforcement of the foundation of Hwy I-80 segments at the harbor around P1 and along the northern embankment around P3, as well as the Hwy 201 segment next to the southern part of the embankment, or a complete relocation of those highway segments; and (d) establishment of buffer zones around the south and east slope near Magna.

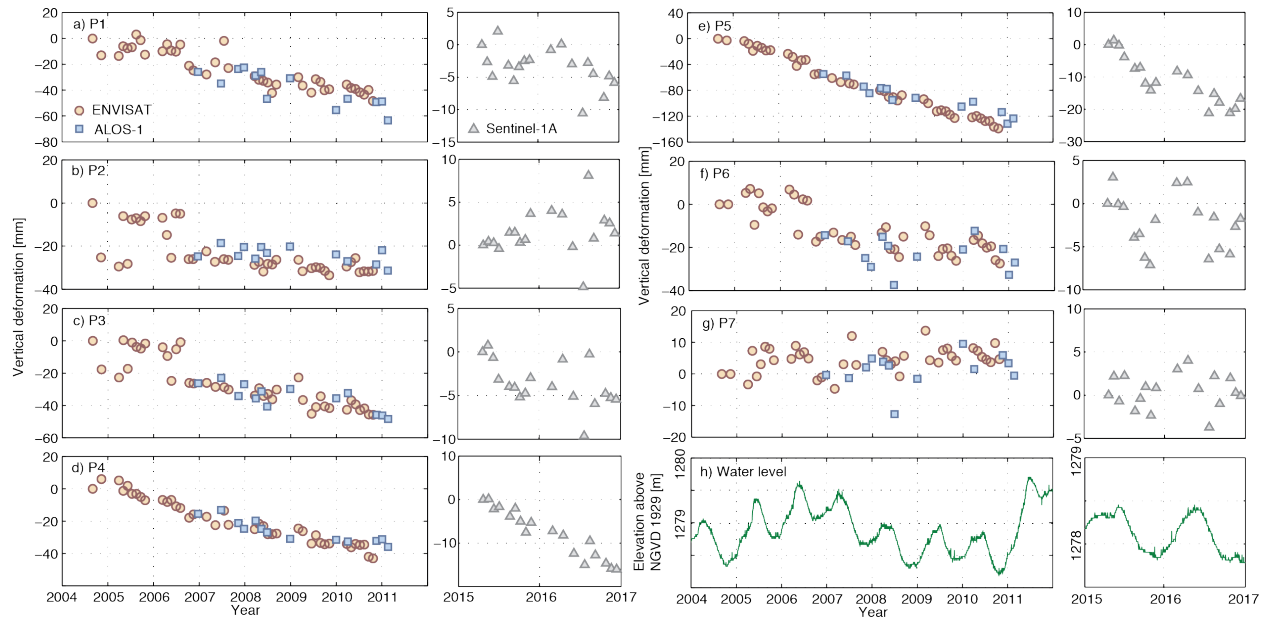


Figure 4.9 Cumulative vertical deformation surrounding the impoundment and water level measurements. (a)-(g) Time-series vertical deformation of the selected sites P1-P7 whose locations are marked in Figures 4.1b and 4.8. The measurements of ENVISAT, ALOS-1 and Sentinel-1A are denoted by the red circles, blue squares and gray triangles, respectively. (h) Daily water level measurements at Saltair Boat Harbor.

4.5 Consolidation settlement modeling

The tailings field can be vertically stratified into five layers from top to bottom – spigotted tailings, soft tailings clay, deep whole tailings, Upper Bonneville clay and interbedded sediments [URS, 1999a]. The surface is covered by the ~6-m thick spigotted tailings, similar to sandy beach deposits that belongs to the tailings, and I consider it as the final load on the tailings structure. Immediately beneath the spigotted tailings layer is the ~10-m soft tailings clay, which is fine-grained and typically classifies as a low-to-medium plasticity silty clays, and the soft tailings clay around the northeast corner area is characterized as decant pond clay, which is in highly saturated and occupies the lowest elevation. The ~45-m layer of older deposits of deep whole tailings are highly interbedded and relatively coarse-grained in nature, and typically classified as a silty sand interbedded with silts and silty clays. The foundation of the tailings structure is composed of lake clays interbedded with lenses of sands. The Upper Bonneville clay is about 4 m in depth and

marked by Gilbert red beds, so called because of oxidation stains resulting in a reddish appearance. The tight clay strata are occasionally interrupted by sand beds, typically with less than 0.6-m thickness; generally, this layer effectively limits the seepage of process water into underlying foundation [Dunne et al., 1999]. Interbedded sediments with various interbedded clays and sands sitting at the bottom have a thickness of ~15 m. The deposits of soft tailings clay and deep whole tailings have an over-consolidation ratio (OCR) of 1.5, attributed to aging and chemical alteration of tailings over time. Underneath the embankment, the maximum OCR of the foundation layers of the Upper Bonneville clay and interbedded sediments can reach 4.0 in the free field.

The settlement of overconsolidated tailings was analyzed using the software Rocscience Settle^{3D} [2009] based on the InSAR-derived surface displacement field. Soil material properties (Table 4.1) are selected adequately based on Kennecott's internal geotechnical reports [Dunne et al., 1999; URS, 1999a; URS, 1999b; Tetra Tech, Inc., 2009] and various documentations on soil properties [Carter and Bentley, 1991; Das, 2002; Das, 2008; Geotechdata info., 2013; Hough, 1969; McCarthy, 1998; Spangler and Handy, 1982; Swiss Standard, 1999].

Table 4.1 Soil material properties of tailings structure

Soil layers	Thickness* [m]	Unit weight* [kN/m ³]	Immediate settlement	Primary consolidation					Secondary consolidation
			Es** [kPa]	Cc**	Cr**	e0**	OCR*	K*** [mm/yr]	C α **
Spigotted tailings (load)	6	18.54	14000	0.36	0.050	0.8	1.2	3150	0.036
Soft tailings clay	10	16.81	2700	0.56	0.074	1.2	1.5	1	0.056
Deep whole tailings	45	18.22	14000	0.41	0.056	0.8	1.2	100	0.041
Upper Bonneville clay	4	18.54	10000	0.36	0.055	0.8	2.5	20	0.036
Interbedded sediments	15	20.26	32500	0.26	0.039	0.8	2.5	100	0.026

Es: Young's modulus

Cc: compression index

Cr: recompression index

e0: initial void ratio

OCR: over-consolidation ratio

K: permeability

C α : secondary compression ratio

Note: Soil material parameters are selected adequately based on Kennecott's internal geotechnical reports (superscript *) and other documentations on soil mechanism (superscript **).

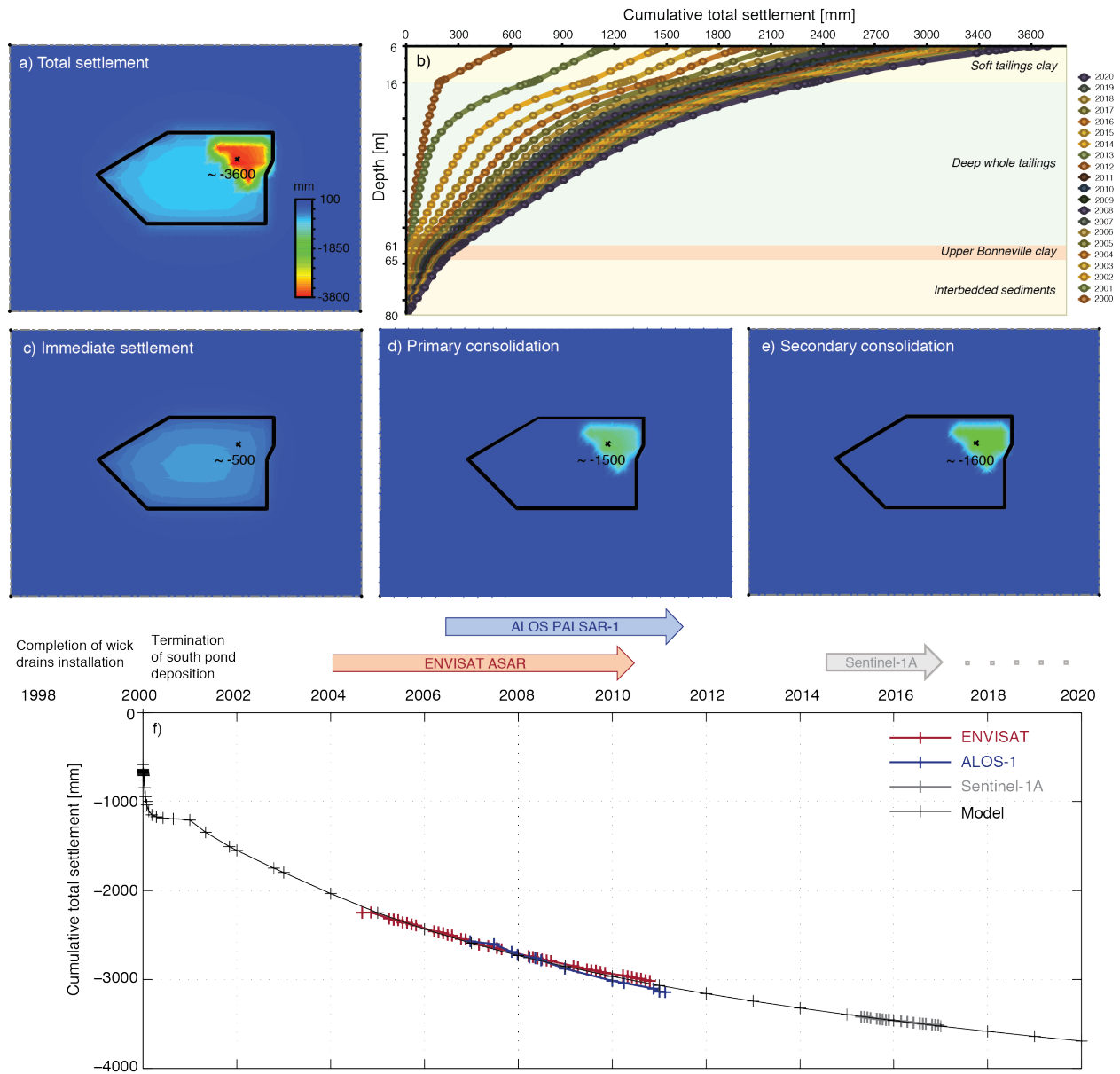
Wick drains/prefabricated vertical drains could support a number of critical engineering requirements during the stability upgrade of the south pond and the construction of the expanded north tailings storage facility [Dunne et al., 1999]. Wick drains were installed around the existing dewatering wells to enhance the drain flows by providing vertical drainage between various tailings layers. Two principal wick drain programs were implemented around the southeast and the northeast corners of the south pond. At the southeast corner, wick drains mainly focused on the eastern reach of the south slope, where hydraulic conductivity was relatively low, and consequently, the flow rates of tailings in this area were relatively slow. The installation followed a triangle pattern with a spacing of 4 m and an averaged depth of 33 m, and most of them were installed between December 1997 and July 1998 [URS, 1999b]. At the northeast corner, the wick

drain program was initiated after realizing significantly lower shear strength than anticipated over the slope at the northeast side of the south pond in 1992 [Dunne et al., 1999]. The prompt field investigation suggested that the clay-sized soil materials in this area had not consolidated to a degree that can sustain the increasing overlying loads. The fine-grained nature of the tailings in this area had entrapped water and resulted in an increase of in situ pore pressures as new material deposition occurred. A series of wick drains were installed mainly at the embankment slope and beach area with a spacing of 2 m and an averaged depth of 60 m, which were believed among the deepest vertical drains installed in the world [Dunne et al., 1999], and the installation were completed between 1995 and 1998 [URS, 1999a].

Wick drain programs have proven effective in controlling excess pore pressure and enhancing the drainage characteristics within the upstream tailings embankment [Dunne et al., 1999]. Since horizontal permeability is usually higher than vertical permeability so that horizontal flow is faster, I assume the ratio of horizontal to vertical permeability K_h/K_v is 2 for all layers. Settlement analyses are carried out using an average pressure (111 kN/m^2) of the top spigotted tailings layer acting on the remaining tailings structure starting from 2000 (the middle time between the installation of wick drains and the abandon of tailings deposition to the south pond). The surface settlement is assumed to be the imprint of the deformation at the interface of spigotted tailings and the underlying soft tailings clay at a depth of 6 m. In addition, to represent the groundwater condition, I added 0-m piezometric line at the layer of soft tailings clay, and 1-m piezometric line at the underlying layers. Wick drains at the southeast corner is along the periphery slopes; however, the coverage at the northeast corner is not accessible from literatures [Dunne et al., 1999; URS, 1999b], so I made assumptions based on InSAR-derived displacement field.

The total settlement is the sum of three components - immediate (elastic) settlement, primary consolidation, and secondary consolidation (creep) (Figures 4.10a and c-e). Immediate settlement occurs instantly after loads are applied and is measured as more than 500 mm at the center of the loads in the model (Figure 4.10c). Immediate settlement is assumed to be linear elastic, and only depends on the total stress, not effective stress. Therefore, pore pressure changes due to settlement have no effect on the immediate settlement. When a load is applied to a low permeability material, a period of primary consolidation is normally expected after load is applied due to dissipating excess pore pressure. Afterwards, continuing settlement, which is known as secondary consolidation, may occur even after a great deal of excess pore pressure has dissipated. The considerable amount of settlement suggests that the tailings structure around the northeast corner is undergoing secondary consolidation on the basis of the selected soil parameters. In the model, I assume that the secondary consolidation starts when the excess pore pressure of the soil drops to 5% of the initial excess pore pressure. The secondary consolidation starts from different stages at different layers, which is determined by soil permeability – low permeability soils dissipate excess pore pressure slowly so that take long time to complete the primary consolidation; on the other hand, high permeability soils dissipate excess pore pressure fast so that the secondary consolidation is initiated at early stages. The model suggests that the impact of primary and secondary consolidation is mainly on the northeast corner with wick drains (Figures 4.10d and e), and their differences are mainly manifested in the temporal behavior. Taken a selected target at the northeast corner, (“x” in Figures 4.10a and c-e) for example, the primary consolidation at this location surges in the first year with more than 600 mm of deformation, followed by a gradual increase by almost 900 mm till 2020. The overall secondary consolidation at the near surface is increasing after placing the load at a steadily decelerated pace, accounting for ~1600 mm of the

~3600 mm total settlement. Figure 4.10b shows the total settlement of the selected target at different depths and stages, exhibiting as a long-term exponential decay as excess pore pressure gradually dissipates. I have also compared the total settlements estimated with the InSAR observations and the modeling results, which shows excellent agreement for all three overlapping time elapses of ENVISAT, ALOS-1 and Sentinel-1A datasets (Figure 4.10f), suggesting a cumulative settlement amount of ~1500 mm between 2004 and 2016. Furthermore, the model provide estimates of future settlement process, e.g., the annual settlement rate at the near surface in 2020 is expected to be around one quarter of the amount in 2004.



4.6 Discussion and conclusions

I have deployed a multi-temporal InSAR method to investigate the nearly decadal deformation behavior of Salt Lake County tailings impoundment, Utah using multi-spaceborne SAR datasets. Despite varied land covers and deformation patterns, I have obtained an adequate density of CT points in the study area by applying adjustable thresholds considering the scattering characteristics of ground targets. I have also overcome the difficulty of phase unwrapping over areas with large deformation rates by “removing” the dominate deformation trend to “detrend” the fringes and later “adding” it back after the performance of phase unwrapping.

The south pond is undergoing drastic consolidation settlement. Four reclamation areas dissected by the ditches are subsiding in a quasi-linear manner (through several years) at different rates. The displacement fields derived from InSAR and differential DEM enable us to pinpoint the compaction peak at the northeast corner. The maximum subsiding rate has decreased from 200+ mm/yr during 2004-2011 to 100+ mm/yr during 2015-2016. I also identify some subsiding sites surrounding the impoundment, and most of them are moving non-linearly, yet there is no clear evidence to show the movements are modulated by water level variations. Particularly, the segments of Hwys I-80 and 201 have a net annual subsidence of ~10 mm. While the subsidence of the sedimentation pond east to the impoundment is decelerated, which is likely due to the settlement effect extended from the south pond. Furthermore, InSAR observations facilitate consolidation settlement modeling, which illustrates the settlement process in different soil layers. Overall, the settlement is undergoing long-term exponential decay, and the annual settlement rate in 2020 is expected to be less than half of the amount one decade ago.

ACKNOWLEDGMENTS

I thank Dr. Thomas Oommen from Michigan Technological University for his assistance during consolidation settlement modeling. I thank Utah Automated Geographic Reference Center (AGRC) for providing the locations of Quaternary faults and U.S. Geological Survey (USGS) for providing water level measurements (site no. 10010000) and earthquake archives in the study region. This research was financially supported by NASA Earth and Space Science Fellowship (NNX15AN10H), U.S. Geological Survey (G14AC00153), and the Shuler-Foscue Endowment at Southern Methodist University. The figures were generated using General Mapping Tools (GMT), MATLAB and Rocscience. Constructive comments from anonymous reviewers and the *Remote Sensing of Environment* Editor, Dr. Michele Manunta improved the manuscript.

REFERENCES

- AGRA Earth and Environmental, Inc. (1998), Independent Analysis of Deformations, Southeast Corner Seismic Upgrade Design, Tailings Impoundment Modernization Project, Kennecott Utah Copper Corporation, Magna, Utah, prepared for Kennecott Utah Copper, Available at http://www.kennecott.com/library/media/Independent_analysis_of_deformations.PDF
- Amos, C. B., P. Audet, W. C. Hammond, R. Bürgmann, I. A. Johanson, and G. Blewitt (2014), Uplift and seismicity driven by groundwater depletion in central California, *Nature*, 509, 483–486.
- Bowker, L. N., and D. M. Chambers (2015), The risk, public liability and economics of tailings storage facility failures, Available at https://www.earthworksaction.org/files/pubs-others/BowkerChambers-RiskPublicLiability_EconomicsOfTailingsStorageFacility%20Failures-23Jul15.pdf
- Caldwell, J., and L. Charlebois (2010), Chapter 3-Tailings impoundment failures, black swans, incident avoidance and checklists. Tailings and Mine Waste 2010, the Organizing Committee of the 14th International Conference on Tailings and Mine Waste, 33–39, Available at <http://www.infomine.com/publications/docs/Caldwell2010d.pdf>
- Carter, M., and S. P. Bentley (1991), *Correlations of soil properties*, Pentech Press, London.
- Colombo, D. (2013), Measuring deformation from space. InSAR as an operational tool for mining sector, *South African Surveying and Geomatics Indaba (SASGI) Proceedings 2013 – Stream I*.
- Das, B. M. (2002), *Principles of Geotechnical Engineering*, 5th ed., Thomas Learning, United State.
- Das, B. M. (2008), *Advanced Soil Mechanics*, Taylor and Francis, London and New York.
- Dunne, B., J. Jackson, Z. Zavodni, H. Ilhan (1999), Application of wick drains to upgrade the Kennecott Utah Copper Magna tailings impoundment – two case studies, Available at <http://www.infomine.com/library/publications/docs/dunne.pdf>

- EARTHWORKS (2011), Problems of Bingham Canyon Mine. EARTHWORKS FACTSHEET, Available at http://www.earthworksaction.org/files/publications/FS_Problems_BinghamCanyon_2011_low.pdf
- EERI (Earthquake Engineering Research Institute), Utah Chapter (2015), Scenario for a Magnitude 7.0 Earthquake on the Wasatch Fault–Salt Lake City Segment, Hazards and Loss Estimates, prepared for the Utah Seismic Safety Commission, Available at http://dem.utah.gov/wp-content/uploads/sites/18/2015/03/RS1058_EERI_SLC_EQ_Scenario.pdf
- Ferretti, A., C. Prati, and F. Rocca (2000), Nonlinear subsidence rate estimation using permanent scatterers in differential SAR interferometry, *IEEE Transactions on Geoscience and Remote Sensing*, 38(5), 2202–2212.
- Geotechdata info. (2013), Soil void ratio, Available at <http://geotechdata.info/parameter/soil-void-ratio.html>
- Hough, B. (1969), *Basic soil engineering*, Ronald Press Company, New York.
- Hu, X., T. Wang, T. C. Pierson, Z. Lu, J. Kim, and T. H. Cecere (2016), Detecting seasonal landslide movement within the Cascade landslide complex (Washington) using time-series SAR imagery, *Remote Sensing of Environment*, 187, 49–61.
- Hudson-Edwards, K. (2016), Global collaboration is needed to mitigate the environmental impacts of mine wastes, *Science*, 352(6283), 288–290.
- ICOLD (International Commission On Large Dams) (2001), Tailings dams risks of dangerous occurrences - lessons learned from practical experiences, Bulletin 121.
- Kennecott Utah Copper (1997), Memorandum to B.D. Farmer from Ray D. Gardner, Legal Counsel, Re: Tailings Impoundment, SE Corner Seismic Instability Review, Available at http://extras.mnginteractive.com/live/media/site297/2008/0321/20080321_044843_kenecott_memo.pdf
- Kennecott Utah Copper (2008), Tailings Impoundment Q and A, Available at [http://www.kennecott.com/library/media/Tailings%20Q and A.pdf](http://www.kennecott.com/library/media/Tailings%20Q%20and%20A.pdf)
- Kennecott Utah Copper (2011), Ground water quality discharge permit UGW350011 Statement of Basis, Available at <http://www.deq.utah.gov/ProgramsServices/programs/water/groundwater/gwpermits/docs/kennecott-tailings/kennecott-tailingsSOB.pdf>

- Kennecott Utah Copper (2016), Rio Tinto Kennecott launches \$2 million pilot project for south slope tailings facility, Available at <http://www.kennecott.com/newsroom/news-releases/rio-tinto-kennecott-launches-2-million-pilot-project-south-slope-tailings>
- Klohn Leonoff (1992), Southeast corner modernization, geotechnical characterization.
- Lu, Z., and D. Dzurisin (2014), *InSAR Imaging of Aleutian Volcanoes: Monitoring a Volcanic Arc from Space*, Springer Praxis Books, Geophysical Sciences, ISBN 978-3-642-00347-9, 390 pp.
- McCarthy, D. F. (1998), *Essentials of soil mechanics and foundations: basic geotechnics*, 5th ed., Prentice Hall.
- Necsoiu, M., and G. R. Walter (2015), Detection of uranium mill tailings settlement using satellite-based radar interferometry, *Engineering Geology*, 197, 267–277.
- Pankow, K. L., J. R. Moore, J. M. Hale, K. D. Koper, T. Kubacki, K. M. Whidden, and M. K. McCarter (2014), Massive landslide at Utah copper mine generates wealth of geophysical data, *GSA Today*, 24(1), doi:10.1130/GSATG191A.1.
- Riedmann, M., J. Anderssohn, and O. Lang (2013), Monitoring of slope stability of tailings dams in South Africa using satellite interferometry, *2013 GRSG AGM - Status and Developments in Geological Remote Sensing*.
- Rocscience Inc. (2009), Settle^{3D} Version 2.0 – Settlement/Consolidation Analysis. www.roscience.com, Toronto, Ontario, Canada.
- Spangler, M. G., and R. L. Handy (1982), *Soil engineering*, 4th ed., Harper Row Publishers, New York, 1982.
- Swiss Standard SN 670 010b (1999), Characteristic Coefficients of soils, Association of Swiss Road and Traffic Engineers.
- Tetra Tech, Inc. (2009), Salt Lake County Tailings Impoundment Study (Draft), prepared for Salt Lake County, Available at http://www.kennecott.com/library/media/Kennecott%20Tailings_Seismic%20Review_DRAFT%20Report.pdf
- U.S. EPA (United States Environmental Protection Agency) (1994), Technical report: Design and evaluation of tailing dams, *EPA report, EPA 530-R-94-038*, 1–59.

URS (URS Greiner Woodward Clyde) (1999a), Geotechnical evaluation summary report for December 17, 1999 State Engineer's Meeting, prepared for Kennecott Utah Copper, Available at <http://www.kennecott.com/library/media/Geotechnical%20Eval%20Summary%20Report.PDF>

URS (URS Greiner Woodward Clyde) (1999b), South slope seismic stability evaluation report, prepared for Kennecott Utah Copper, Available at <http://www.kennecott.com/library/media/SOUTH%20SLOPE%20SEISMIC%20STABILITY%20EVALUATION%20REPORT.pdf>

UDEQ (Utah Department of Environmental Quality) and EPA (Environmental Protection Agency) (2014), Five-year review report - Kennecott north zone superfund site, Available at <http://www.epa.gov/sites/production/files/2014-06/documents/kennecott-north-1fyr-6-17-2014.pdf>; <http://www.epa.gov/sites/production/files/2014-06/documents/kennecott-north-1fyr-appendix-a.pdf>; <http://www.epa.gov/sites/production/files/2014-06/documents/kennecott-north-1fyr-appendix-b.pdf>

WISE (World Information Service on Energy) (2015), Chronology of major tailings dam failures (from 1960 to 2015), WISE Uranium Project, Tailings Dam Safety, Available at <http://www.wise-uranium.org/mdaf.html>

CHAPTER 5

CONCLUDING REMARKS

The work presented in this dissertation is motivated by the desire to advance our understanding of the evolution of geohazards and landform alterations associated with hydrologically driven ground deformation in geodetic time scale, with a focus on the landslides, aquifer systems, and the mine tailings impoundment.

This dissertation illustrates how the spaceborne remotely sensed InSAR images can be used to retrieve the spatio-temporal complexity of the ground deformation, and how the deformation products can further contribute to the understanding of the mechanisms, developments, and hydrological architectures of the targeted geodynamic settings, in the context of either anthropogenic or natural triggering. The highlights of the major chapters of this dissertation are summarized below.

5.1 Highlights

Chapter 2:

- Map spatio-temporal landslide motions using the proposed time-series InSAR method, correcting the artifacts associated with the atmosphere and DEM errors.
- Re-evaluate the incipient motion related to 2008 Greenleaf Basin rock avalanche, which is one month earlier than the reported date.
- Recognize active motion at the mouth of Greenleaf Basin, which could be a precursor to

an extremely hazardous failure to the residences and facilities downslope.

- Characterize the hydrology-driven seasonal landslide movement: the hydrological loading effects determine the movement magnitude in Cascade Range.
- Reveal rainfall triggered precursory (slope-normal) subsidence before downslope sliding using high-temporal-sampling Sentinel-1A InSAR and on-slide GPS results.
- Extract quasi-3D displacement field on slope plane using two independent spaceborne InSAR observations.
- Invert for the thickness and basal geometry of the slow-moving landslide by applying the mass conservation on the spaceborne InSAR-derived displacement fields.

Chapter 3:

- Image of basin-wide spatio-temporal ground deformation over Salt Lake Valley, Utah from spaceborne InSAR data.
- Characterization of hydrogeological properties using long-term and seasonal deformation observations and hydrological records.
- Mapped tectonic faults from InSAR and discussed their role in disturbing groundwater flow and partitioning hydrological units.
- Characterized and differentiated the ground deformation due to anthropogenic activities and natural hydrological processes.
- Constrained the strain rate and the apparent geometry of subsurface groundwater reservoirs.

Chapter 4:

- Mapped tailings settlement process using InSAR and differential DEM.
- Derived 2D displacement field and differentiated consolidation behavior in space.

- Modeled and predicted the exponentially decaying consolidation settlement.
- Evaluated the stability of surrounding infrastructures such as highways.
- Investigated the potential correlation between non-linear motions and water level changes.

5.2 Future work

The dynamics of landslides is important to the studies of geomorphologic evolution, climate change, and historic earthquakes. The case study of the Crescent Lake landslide, WA, has provided insights into spatio-temporal landslide mobility and basal complexity of a typical shallow translational landslide. Beyond that, I have been working on, and would like to further investigate the slowly moving landslides in the coastal bluffs in the northwestern Pacific region, United State. Figure 5.1 shows some preliminary results of mapping the slowly moving landslides over the national forests in northern California. With respect to InSAR technical improvements, I will focus on correcting the phase aliasing during unwrapping in areas with complicated spatio-temporal deformation. With respect to landslide mechanism investigations, I will derive the diffusivity based on diffusion equation using the cross-correlation between the precipitation-modulated transient pore-pressures at depth with time-series landslide motions. The systematical investigation of landslide dynamics can provide statistic data source for the landslide hazard planners during their probabilistic risk assessment.

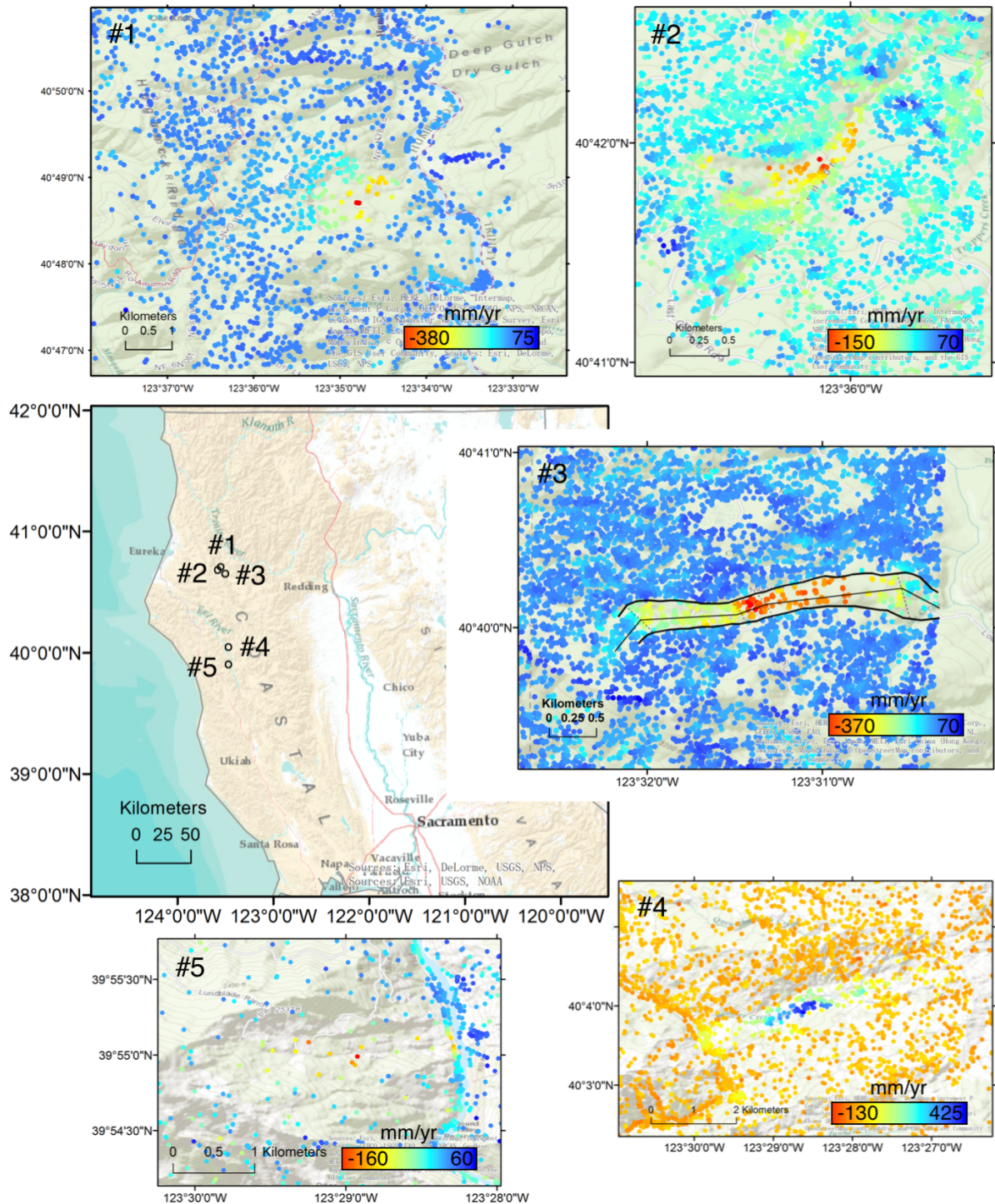


Figure 5.1 Preliminary results of InSAR-mapped slowly moving landslides over the national forests in northern California. Orange shadows mark the areas prone to landsliding. The applied InSAR data are ALOS-1 PALSAR-1 spanning 2007-2011.

Along with the historic and popular spaceborne SAR images such as ERS-1/2, ENVISAR ASAR, ALOS-1 PALSAR-1, COSMO-SkyMed, TerraSAR-X, and RADARSAT-1/2, the newly acquired Sentinel-1A/B and ALOS-2 PALSAR-2 images, as well as the planned missions such as NASA-ISRO SAR, are enriching and enhancing the SAR data archive not only in the aspects of the length and coverage of observations, but also radar frequency, temporal sampling, spatial resolution, image mode and polarization. An increasing number of data, in no doubt, provide new opportunities to image the shallow solid earth system through the space.